

Aalborg Universitet



**AALBORG  
UNIVERSITY**

## **HYBRID ANTENNA ARRAY DESIGN AND TECHNIQUES FOR SELF-BACKHAULED WIRELESS ACCESS POINTS**

Tariq, Muhammad Haroon

*DOI (link to publication from Publisher):*  
[10.54337/aau718334904](https://doi.org/10.54337/aau718334904)

*Publication date:*  
2024

*Document Version*  
Publisher's PDF, also known as Version of record

[Link to publication from Aalborg University](#)

*Citation for published version (APA):*  
Tariq, M. H. (2024). *HYBRID ANTENNA ARRAY DESIGN AND TECHNIQUES FOR SELF-BACKHAULED WIRELESS ACCESS POINTS*. Aalborg University Open Publishing. <https://doi.org/10.54337/aau718334904>

### **General rights**

Copyright and moral rights for the publications made accessible in the public portal are retained by the authors and/or other copyright owners and it is a condition of accessing publications that users recognise and abide by the legal requirements associated with these rights.

- Users may download and print one copy of any publication from the public portal for the purpose of private study or research.
- You may not further distribute the material or use it for any profit-making activity or commercial gain
- You may freely distribute the URL identifying the publication in the public portal -

### **Take down policy**

If you believe that this document breaches copyright please contact us at [vbn@aub.aau.dk](mailto:vbn@aub.aau.dk) providing details, and we will remove access to the work immediately and investigate your claim.



**HYBRID ANTENNA ARRAY DESIGN AND  
TECHNIQUES FOR SELF-BACKHAULED  
WIRELESS ACCESS PO**

**BY  
MUHAMMAD HAROON TARIQ**

PhD Thesis 2024



**AALBORG UNIVERSITY**  
DENMARK



# **HYBRID ANTENNA ARRAY DESIGN AND TECHNIQUES FOR SELF-BACKHAULED WIRELESS ACCESS POINTS**

by

Muhammad Haroon Tariq



**AALBORG UNIVERSITY**  
DENMARK

*Dissertation submitted to the Department of Electronic Systems and the committee  
on graduate studies of Aalborg University in partial fulfilment of the requirements  
for the degree of Doctor of Philosophy.*

January 2024

Submitted: January 2024

Main Supervisor: Professor Dr. Shuai Zhang,  
Aalborg University

Co-supervisor(s): Professor Dr. Constantinos B. Papadias,  
Alba – The American College of Greece

Assessment: Associate Professor Gilberto Berardinelli (chairman)  
Aalborg University Denmark  
Professor Ana García Armada  
Universidad Carlos III de Madrid, Spain  
Professor Ville Valteri Viikari  
Aalto University, Finland

PhD Series: Technical Faculty of IT and Design, Aalborg University

Department: Department of Electronic Systems

ISSN: 2446-1628  
ISBN: 978-87-94563-11-6

Published by:  
Aalborg University Open Publishing  
Kroghstræde 1-3  
DK – 9220 Aalborg Øst  
aauopen@aau.dk

© Copyright: Muhammad Haroon Tariq

Printed in Denmark by Stibo Complete, 2024

## ENGLISH SUMMARY

The use of self-backhauled access points (SBAPs) serving as data relays / base stations holds unique significance for delivering on-demand wireless broadband connectivity for public safety services such as recovery after communication infrastructure failures caused by natural disasters. The self-backhauled nodes can be mobile, for instance, placed on unmanned aerial vehicles (UAV) or fixed. The SBAPs can be beneficial for a number of mobile or fixed wireless access use cases, such as Smart City (SC) services, providing connectivity for citizens and SC infrastructure, fixed wireless access using street-level distribution and access via so-called “street furniture” equipment, for which fronthauling is also an important problem to be studied due to the typical obstacles at street level. UAV-borne SBAPs could also be stationed and docked on roof tops. Deployment of such base stations can face some restrictions that need to be considered such as the availability of reliable wireless backhaul links to transfer all the traffic to the core network from the targeted area. Since the SBAPs will have to operate in different environments (e.g., urban / suburban / rural, high/low height, high/low interference, special venues such as sports or emergency sites, etc.), it is important that their wireless backhaul links adapt to such conditions. Moreover, the backhaul link must be reliable, high rate and ideally low-latency (especially for critical situations such as emergency events but also for all real-time end-user applications). The problem of backhauling of the prescribed SBAPs of the network will be studied in this thesis. In order to satisfy the needs of the proposed network, the base station will benefit from highly directional antennas with narrow beamwidth and adaptive precoding schemes. To cope with the challenges of wireless backhaul, microwave and centimeter wave (cmWave) massive Multiple Input Multiple Output (mMIMO) communication will be considered for hybrid transceivers. The study will focus on microwave and centimeter wave (60GHz) frequencies, which allow wide bandwidth, as well as on adaptive hardware-efficient antenna arrays at such frequencies in order to tackle the propagation and interference environment. To reduce the complexity of RF chains being used in beamforming, we will consider hybrid arrays that may include a combination of active antenna elements, passive elements as well as phase shifters for sub 6GHz and cmWave (60GHz) frequencies. Considering situations like special events, disaster or aid missions, challenges and requirements for mobile UAVs will be investigated. The work will target both the design and configuration of hybrid energy-efficient antenna array architectures for the considered frequencies, as well as the development of channel models based on measurements at cmWave (60GHz) frequencies for such applications.

## DANISH SUMMARY

Brugen af SBAP'er (self-backhauled access points), der fungerer som data relæer / basestationer, har enorm betydning for levering af on-demand-forbindelse via fast trådløst bredbånd samt levering af offentlige sikkerhedstjenester eller hjælp til genopretning efter svigt i kommunikation infrastrukturen forårsaget af naturkatastrofer. De selv bærende knudepunkter kan være mobile, hvor et ubemandet luftfartøj (UAV) ikke kun kan betjene mobile brugere, men også faste bredbåndsbrugere. SBAP'erne kan være fordelagtige til en række anvendelser af fast trådløs adgang, såsom Smart City (SC) Services, der leverer forbindelse til SC-infrastruktur og fast trådløs adgang ved hjælp af distribution på gadeniveau og adgang via såkaldt "gademøbler"-udstyr, for hvilket fronthauling også er et vigtigt problem, der skal undersøges på grund af de typiske forhindringer på gadeniveau. De kan også stationeres og dockes på tagstationer. Udrulning af sådanne basestationer kan have nogle begrænsninger, der skal overvejes, såsom tilgængeligheden af pålidelige trådløse backhaul-links til at overføre al trafik til kernenettet fra målområdet. Da SBAP'erne skal fungere i forskellige miljøer (f.eks. by/forstad/land, høj/lav højde, høj/lav interferens, særlige steder som sports- eller nødsteder osv.), er det vigtigt, at deres trådløse backhaul-links kan tilpasses sådanne forhold. Desuden skal backhaul-linket være pålideligt, have høj hastighed og helst lav latenstid (især i kritiske situationer som nødsituationer, men også til alle slutbrugerapplikationer i realtid). Problemet med backhauling af netværkets påtænkte selv-backhaul access points (SBAP) vil blive undersøgt i den foreslåede forskning. For at tilfredsstille behovene i det foreslåede netværk, vil basestationen drage fordel af meget retningsbestemte antenner med smal strålebredde og adaptive forkodningsordninger. For at klare udfordringerne ved trådløs backhaul, vil mikrobølge- og millimeterbølge (mmWave) massiv Multiple Input Multiple Output (mMIMO) kommunikation blive overvejet til hybride transceivere. Undersøgelsen vil fokusere på mikrobølge- og mmWave-frekvenser, som tillader bred båndbredde, samt på adaptive hardwareeffektive antennearrays ved sådanne frekvenser for at tackle udbredelses- og interferensmiljøet. For at reducere kompleksiteten af RF-kæder, der bruges i beamforming, vil vi overveje hybride arrays, der kan omfatte en kombination af aktive antenneelementer, passive elementer samt faseskiftere til sub 6GHz- og mmWave-frekvenser. I situationer som særlige begivenheder, katastrofer eller hjælpemissioner vil udfordringer og krav til mobile UAV'er blive undersøgt. Arbejdet vil være rettet mod både design og konfiguration af hybride energieffektive antennearkitekturer til de betragtede frekvenser samt udvikling af kanal modeller baseret på målinger ved mmWave-frekvenser til sådanne anvendelser.

**Muhammad Haroon Tariq**

 Mesogeion 61, Marousi, 15126, Athens, Greece

 +30-6996083423 | +92-344-5423823

[mtariq@acg.edu](mailto:mtariq@acg.edu) | [haroontariq.awan@seecs.edu.pk](mailto:haroontariq.awan@seecs.edu.pk)

**Research Experience**

---

March 2020 – Present

**Research Scientist (Marie Curie Fellow – project PAINLESS)**

- Smart Wireless Future Technologies (SWIFT) Lab
- Research Technology and Innovation Network (RTIN)
- Alba – The American College of Greece (ACG), Athens, Greece
- *Design and development of multi-active / multi-passive parasitic antenna arrays.*
- *Analysis of mutual coupling on parasitic antenna arrays.*
- *Energy efficient antenna array design for backhauling of UAVs.*
- *Algorithm development for beamforming of parasitic antenna arrays.*
- *Channel measurements and modeling for mmWaves using NOKIA Bell labs equipment.*

May 2019 – Feb 2020

**Research Scientist (Marie Curie Fellow – project PAINLESS)**

Broadband Wireless and Sensor Networks (B-WiSE) Lab

Athens Information Technology (AIT), Athens, Greece

- *Design guidelines for radiation of parasitic antenna arrays.*
- *Channel measurements for mmWaves using Facebook sounder nodes.*
- *Mobile backhauling for portable access points.*

Nov 2015 – Dec 2016

**Post Graduate Researcher (Erasmus Mundus – INTACT Research Grant)**

Frederick University, Nicosia, Cyprus

- *Dynamically reconfigurable RF devices: RF energy harvesting and rectification to formulate baseband voltage signal. Antenna design and actuation of FET and PIN diode switches to dynamically modify the behavior of RF devices.*
- *RF component modeling for simultaneous wireless information and power transfer (SWIPT) system: Development of RF power splitting network for the ratios from 1:1 to 1:16.*
- *Design and implementation of reconfigurable power splitter for maximum RF power harvesting at a given SNR level.*

**Educational Qualifications**

---

2019 – 2023

**PhD Wireless Communications**

Dept. of Electronics Engineering, Aalborg University, Denmark ([www.aau.dk](http://www.aau.dk))

- **PhD Title:** Hybrid Antenna Array Design and Techniques for Self-Backhauled Wireless Access Points

- **Major Subjects:** Radiating Systems and Antennas, Channel Propagation and Measurements/Modeling, Wireless Communications

2011 – 2014

### **MS Electrical (Telecommunication) Engineering**

National University of Sciences and Technology (NUST), Islamabad, Pakistan  
([www.mcs.nust.edu.pk](http://www.mcs.nust.edu.pk))

- **MS Thesis:** Microwave Beamforming Using Frequency Selective Surfaces
- **Major Subjects:** Advance Electromagnetics, Radiating Systems and Antennas, Wireless Communications

2007 – 2011

### **BS Electrical (Telecommunication) Engineering**

COMSATS Institute of Information Technology (CIIT), Islamabad, Pakistan  
([www.comsats.edu.pk](http://www.comsats.edu.pk))

- **Pakistan Engineering Council (PEC) REG. No:** ELECT-32414
- **Major Subjects:** Electromagnetics, Antennas Propagation and Radiating Systems, Wireless Communications

## **Internships/Trainings**

---

March 2022 – April 2022

### **Secondment / Internship – Aalborg University, Denmark**

Antennas, propagation and Millimeter waves Systems (APMS) Section  
Department of Electronics Engineering,

- **Research Objectives:** Performance analysis of the wideband antenna array designed for portable access points and antenna measurements in an anechoic chamber.

Nov 2021 – Jan 2021

### **Secondment / Internship – University College London, UK**

Department of Electronics and Electrical Engineering,

- **Research Objectives:** Derivation of radiation conditions for the parasitic antenna arrays for UAVs and performance analysis of PAAs using CST simulations

19 – 23 July 2010

### **Workshop on Antenna Designing using CST**

- COMSATS Institute of Information Technology, Islamabad, Pakistan

## **Publications**

---

- **Muhammad Haroon Tariq**, Constantinos B. Papadidas, Shuai Zhang, Christos Masouros, “Energy Efficient Hybrid Beamforming Using Multi-Active/Multi-Passive Parasitic Antenna Arrays for Portable Access Points”, *IEEE Transactions on Aerospace and Electronic Systems*, January 2024 (**Submitted**)
- **Muhammad Haroon Tariq**, Iason Grivas, Constantinos B. Papadidas, Jinfeng Du, Dmitry Chizhik and Reinaldo Valenzuela, Mauricio Rodríguez, Rodolfo Feick, “mmWave Channel Measurements and Modeling for Outdoor to Indoor

- Fixed Wireless Communications”, *IEEE Transactions of Antennas and Propagation (TAP)*, January 2024 (**Not submitted yet**)
- Nikolaos Ntetsikas, Nithin Babu, **Muhammad Haroon Tariq**, Constantinos B. Papadias, Jinfeng Du, Dmitry Chizhik and Reinaldo Valenzuela, Mauricio Rodriguez, Rodolfo Feick, “60 GHz Outdoor to Indoor (O2I) Propagation Measurements in a University Campus”, *SPAWC*, July 2022
  - White Paper: Telecom Infra Project (TIP) Channel Sounder measurements for fixed wireless mmWave Networks Project Group, September 2020
  - **Muhammad Haroon Tariq**, Ioannis Chondroulis, Panagiotis Skartsilas, Nithin Babu, Constantinos B. Papadias, “mm Wave Massive MIMO Channel Measurements for Fixed Wireless and Smart City Applications”, *IEEE International Symposium on Personal, Indoor and Mobile Radio Communications (PIMRC)*, August 2020
  - **Muhammad Haroon Tariq**, Dimitrios D. Ntaikos, Constantinos B. Papadias, “Design Guidelines for Multi-Active / Multi-Passive Parasitic Antenna Arrays”, *IEEE Antennas and Wireless Propagation Letters (AWPL)*, September 2020
  - **Muhammad Haroon Tariq**, Abdul Quddious, M. Ali Babar Abbasi, Symeon Nikolaou, “On the Use of Tunable Power Splitter (PS) for Simultaneous Wireless Information and Power Transmission (SWIPT) Receivers”, *International Journal of Antennas and Propagation (IJAP)*, 2018
  - **Muhammad Haroon Tariq**, Saba Rashid, Farooq A. Bhatti, “Dual Band Microstrip Patch Antenna for WiMAX and WLAN Applications”, *International journal of Multidisciplinary and Current Research (IJMCR)*, ISSUE Feb 2014, ISSN: 2321-3124.
  - Aqeela Saghir, S. Muzahir Abbas, M. Usman Afzal, **Muhammad Haroon Tariq**, Tauseef Tauqeer, “Compact Dual Band Microstrip Antenna Design Using Slits”, *3rd IEEE International Conference on Computer, Control & Communication (IC4)*, 2013
  - Saleem Shahid, M. Ali Babar Abbasi, M. Rizwan and Sabaina Rafique, **Muhammad Haroon Tariq** “A Compact Multiband Antenna for GSM and WiMAX Applications”, *2nd International Multi Topic Conference (IMTIC 2012)*, *Springer Communications in Computer and Information Science*, Vol-281, 2012, pp. 20-30

## Achievements

---

- Marie Curie Fellowship Award under Horizon 2020 project PAINLESS, May 2019 – Dec 2022.
- Erasmus Mundus Scholarship under INTACT project, Oct 2015 – Jan 2017.
- Merit-based Punjab Educational Benevolent Fund Scholarship for 8 years, 2006 – 2013.
- Merit-based Financial Assistance and Tuition Waiver Scholarship at COMSATS IIT, 2007 – 2011.
- Best Student of the Year Award: 1996, 1999 – 2005 and 2010 – 2011.
- 1st position in Explore A Vision in all Pakistan Electronix Olympiad held at GIKI, 4 – 6 Feb 2011.

- 2nd position in Entrepreneurship Forum in all Pakistan CEPEX held at CIIT Islamabad, 13 – 14 April 2011.
- Won Antenna Design Competition in all Pakistan Electronix Olympiad held at GIKI, 4 – 6 Feb 2011.
- Participated in Antenna Design Competition in Open House organized at CIIT Islamabad, 2010.

## Technological Skills

---

### **Programming:**

MATLAB, Simulink, C++, VMLab

**RF/Microwave Circuits Designing** – Familiar with the RF/microwave circuit modeling which includes antennas, parasitic antenna arrays, filters, rectennas, microstrip, frequency selective surfaces.

### **RF/Microwave Circuits fabrication:**

Hands-on experience on traditional etching process using iron chloride, also familiar with the milling machine LPKF

Protomate H100.

**RF /Microwave Circuits Performance Characterization** – Hands-on experience of S-parameters measurements on Agilent vector network analyzer and radiation pattern measurements on NSI Anechoic Chamber system and conformity testing.

SNR measurements using spectrum analyzer and signal generators.

**Electromagnetic field analysis** – very familiar with the EM simulation tools such as CST Microwave and Design studio, Ansoft HFSS and Keysight ADS/Momentum.

## References

---

### **Dr. Shuai Zhang**

Associate Professor

Antennas, Propagation and Millimeter wave Systems (APMS)

Department of Electronic Systems

Aalborg University, Denmark

sz@es.aau.dk

+45-99407532

### **Dr. Constantinos B. Papadias**

Executive Director

Research, Technology & Innovation Network (RTIN)

Scientific Director, The American College of Greece Research Center (ACG-RC)

Professor, Information Technology, Deree & Alba

Fellow, IEEE and European Alliance of Innovation

cpapadias@acg.edu

+30-694-7428689

# ACKNOWLEDGEMENTS

الْحَمْدُ لِلَّهِ

This journey was nothing short of an exhilarating ride, and like all rides, it had its fair share of ups and downs. Pursuing a Ph.D. degree was a lifelong dream. Undoubtedly, many people have helped me realize this dream, and I owe my deepest gratitude to them. I am grateful to Marie Skłodowska-Curie Actions for providing me with an opportunity to carry forward my research and doctoral degree, under the project **PAINLESS**. I am thankful to the project **FIREMAN** as well for the partial funding of my stay in Greece. Firstly, **Prof. Constantinos Papadias**, who not only took me on this challenging journey but also expertly mentored me with kindness, sincerity, and affection. Thank you, sir, for treating me like your son and making me a part of your family. From the first meeting with him, I knew I was going to the right place. With his kind, determined, motivating, and easy-going nature, I fit right in. I am grateful for all the lessons, which were not always restricted to science. **Prof. Shuai Zhang**, his passion for science, his insights, reviews and suggestions for the improvement of scientific work and inquisitive nature will forever be inspiring to me. **Mr. Marios Sardis and Prof. George** have truly been blessings for me. Their scientific insights, always-ready-to-help attitude, and drive have been helpful for the proof of concept. I am also grateful to all the past and present members of the **SWiFT Lab**, **Nithin, Nikos, Ivan, David, Iason, Panos, Spyros, Sebastian, and Aimilios**, who made lab life exciting and were always there. #Salutes 'BROTHERS'. My deepest gratitude to the team at **NOKIA Bell Labs**, **Prof. Dimitry, Prof. Jinfeng and Prof. Reinaldo**, who provided us with the equipment for the channel measurements. You have helped me a lot with the improvement of results and the data analysis of the project. Thanks to the **Antennas Propagation and Milimeter wave Section (APMS)** at Aalborg University, Denmark, for providing me the opportunity to become a member of the section and to do the research in your labs. The experience was amazing. Our collaborator, **Prof. Christos Masouros**, at the University College London helped me advance this study, and I am thankful to **Prof. Izzat and Dr. Temitope** for all their help and guidance for prototyping of the antenna array. All the efforts and support to measure antenna array by Intracom Defense is highly appreciated. **Mr. Tariq Mehmood Malik and Shahida Yasmin**, my parents, have shared this dream with me since I was a child. Their love, support, and prayers have been phenomenal, and I can't thank them enough for making me the man that I am today. They have been the epitome of strength to me and have always believed in me. I owe all my achievements to them.

## ACKNOWLEDGEMENTS

My **sisters** have always cheered me on. I am eternally thankful for all the support and encouragement from miles away. **Adeena Shafique**, my partner for life, made this journey even more exciting. Thank you for all the adventures and being my constant support system. This incredible feat would not have been achieved without the family that I chose, my friends. **Maria, Aqeela, Fehmida, Hemal, Uzair, Rafay, Babar, Nouman, Saleem**....I am forever thankful to each and every one of you.

# LIST OF ABBREVIATIONS

PAA	Parasitic Antenna Arrays
SAMP	Single-Active/Multi-Passive
MAMP	Multi-Active/Multi-Passive
SBAP	Self-Backhauled Access Points
UAV	Unmanned Aerial Vehicle
MIMO	Multiple Input Multiple Output
mMIMO	massive MIMO
UE	User Equipment
SC	Smart City
AE	Active Element
PE	Parasitic Element
ULA	Uniform Linear Array
SISO	Single Input Single Output
SDR	Software Defined Radio
USRP	Universal Software Radio Peripheral
GUI	Graphical User Interface
RSSI	Received Signal Strength Index
SNR	Signal to Noise Ratio
BPSK	Binary Phase-shift keying
Tx	Transmitter
Rx	Receiver
RF	Radio Frequency
mmWave	Millimeter Waves
3GPP	3 <sup>rd</sup> Generation Partnership Project
FSPL	Free Space Path Loss
LOS	Line of Sight
NLOS	Non-Line of Sight
CSI	Channel State Information
FD	Full Duplex
PCB	Printed Circuit Boards
SBA	Stochastic Beamforming Algorithm
AOSBA	Alternating Optimization Stochastic Beamforming Algorithm
ACG	The American College of Greece
AAU	Aalborg University
UCL	University College London

# TABLE OF CONTENTS

<b>Chapter 1. Introduction.....</b>	<b>1</b>
1.1. Background.....	1
1.2. State of the art.....	1
1.2.1. Self-Backhaul.....	1
1.2.2. Massive MIMO.....	3
1.2.3. Parasitic Antenna Arrays.....	4
1.3. Ph.D. Project objectives.....	6
1.4. Key Methods.....	7
1.5. Significance and Outcome.....	11
1.6. Thesis Outline and Contributions.....	12
1.7. References.....	15
<b>Chapter 2. Design Guidelines and Radiation conditions.....</b>	<b>21</b>
2.1. Introduction.....	21
2.2. PAA Loads and Coupling Matrix.....	22
2.3. PAAs Radiation and Design Conditions.....	25
2.4. MAMP design.....	26
2.5. Results and discussion.....	27
2.5.1. MAMP-I.....	28
2.5.2. MAMP-II.....	31
2.6. Conclusion.....	34
2.7. References.....	35
<b>Chapter 3. Hybrid Beamforming Using Multi-Active/Multi-Passive Parasitic Antenna Arrays.....</b>	<b>36</b>
3.1. Introduction.....	36
3.2. System Model.....	38
3.3. Radiation conditions.....	39
3.4. Alternating Optimization Stochastic Beamforming Algorithm.....	42
3.5. MAMP design and results.....	45
3.5.1. Computation of Loads.....	45

3.5.2. Simulations using cst microwave studio .....	47
3.5.3. MAMP antenna array prototype.....	55
3.6. References.....	62
<b>Chapter 4. Propagation Measurements and Channel Modeling.....</b>	<b>65</b>
4.1. Introduction.....	65
4.1.1. Limiting factors for millimeter wave communications .....	66
4.1.2. Channel Modeling.....	67
4.2. Outdoor to Outdoor.....	67
4.3. Outdoor to Indoor.....	74
4.3.1. NOKIA Phase-I.....	74
4.3.2. NOKIA Phase-II.....	74
4.4. References.....	87
<b>Chapter 5. Experiments and Proof of Concept Demos .....</b>	<b>94</b>
5.1. Fireman setup.....	94
5.2. Antenna performance using USRPs .....	98
5.2.1. Antenna Performance for 4G Setup .....	98
5.2.2. Antenna performance Based on Power Measurements .....	102
<b>Chapter 6. Conclusions and Future Work.....</b>	<b>108</b>

# LIST OF FIGURES

Figure 1-1	Self-backhaul architecture.....	2
Figure 1-2	Roadmap of the thesis.....	10
Figure 2-1	Geometry of the Single-Active / Multi-Passive antenna array. ....	22
Figure 2-2	Multi-Active / Multi-Passive parasitic antenna array geometry. ....	24
Figure 2-3	The geometry of a multi-active / multi-passive antenna array with four (red-colored) active elements and sixteen (blue-colored) parasitic elements. The distance between SAMPs (active elements) is $\lambda/2$ and the distance between the parasitic elements is $0.2 * \lambda$ . ....	26
Figure 2-4	MAMP antenna array designed in CST microwave studio. Red-colored dots are active ports for feeding the array, and blue dots are parasitic elements with respective capacitive or inductive values. ....	27
Figure 2-5	Representation of the radiation patterns: the red color represents the radiation pattern of a six-element uniform linear array, and the magenta represents a four-element ULA, whereas blue color is representing radiation pattern of a MAMP. ....	28
Figure 2-6	Comparison of the normalized gains with that of achieved by 6-element ULA, 4-element ULA and a MAMP with 4 active and 16 parasitic elements.....	29
Figure 2-7	Error is calculated during each iteration when both the radiation patterns, the proposed MAMP and ULA are compared. ....	29
Figure 2-8	3D radiation pattern of the MAMP-I, where port 2 is having a negative input impedance.....	30
Figure 2-9	Top view of the 3D radiation pattern of the MAMP-I. ....	30
Figure 2-10	Representation of the radiation patterns: the red color represents the radiation pattern of a 6-element uniform linear array, and the magenta represents a 4-element ULA, whereas blue color is representing radiation pattern of a MAMP. ....	31
Figure 2-11	Comparison of the normalized gains with that of achieved by 6-element ULA, 4-element ULA and a MAMP with 4 active and 16 parasitic elements.....	32
Figure 2-12	Error is calculated during each iteration when both the radiation patterns, the proposed MAMP and ULA are compared. ....	32
Figure 2-13	3D radiation pattern of the MAMP-II, where all the feeding ports have an input impedance which is greater than zero.....	33
Figure 2-14	Top view of the 3D radiation pattern of the MAMP-II. ....	33
Figure 3-1	Multi-Active / Multi-Passive parasitic antenna array geometry.....	38
Figure 3-2	MAMP geometry in MATLAB; blue-colored crosses represent the parasitic elements, and the red dots represent the active elements. ....	46

TABLE OF FIGURES

Figure 3-3	The geometry of the MAMP array in CST, the cylinders are half-wave dipoles connected to passive components and grounded through via holes. The blue dots are the loads (passive components, capacitors, or inductors calculated from SBA) whereas the red dots are the feeding ports to feed the active elements. .... 48
Figure 3-4	The geometry of the MAMP in CST: (a) Top view of the structure, (b) bottom view..... 49
Figure 3-5	Calculated and simulated radiation pattern of MAMP PAA, comparison of the radiation patterns where magenta is representing a ULA with 2 active elements, red is for the 5 ULA to be compared with the MAMP beam, blue is the calculated beam pattern of MAMP using SBA based on different combination of loads and black is the radiation pattern of MAMP array obtained from CST simulations: (a) beam directed towards $\varphi = 60^\circ$ (b) beam directed towards $\varphi = 90^\circ$ (c) beam directed towards $\varphi = 120^\circ$ ..... 51
Figure 3-6	The 3D Radiation pattern of the MAMP array obtained from CST simulations: (a) beam directed towards $\varphi = 60^\circ$ (b) beam directed towards $\varphi = 90^\circ$ (c) beam directed towards $\varphi = 120^\circ$ ..... 52
Figure 3-7	Comparison of different parameters of MAMP array while the beam was directed towards $\varphi = 60^\circ$ , $\varphi = 90^\circ$ and $\varphi = 120^\circ$ (a) max realized gain against the $\varphi$ angle (b) max realized gain at the given frequency for all the beam steering angles (c) total efficiency of the MAMP at the given frequency for all the beam steering angles. .... 55
Figure 3-8	MAMP antenna array prototype..... 56
Figure 3-9	Setup for measuring the S-parameters using a vector network analyzer. .... 56
Figure 3-10	Measured and simulated S-parameters of the MAMP antenna array. The red curve represents the simulated while the blue is representing the measured S-parameters of the structure. .... 57
Figure 3-11	Measuring radiation pattern in the anechoic chamber: (a) antenna under test (b) setup for the measurement of radiation pattern..... 58
Figure 3-12	Measured and simulated radiation patterns of the MAMP antenna array. .... 58
Figure 3-13	Measured and simulated gain of the MAMP antenna array..... 59
Figure 4-1	Indoor LoS measurements setup: (a) a conference room setup with a distance of 2–6m between Tx and Rx (b) Measurements in the corridor where the distance between Tx and Rx is 20m. .... 69
Figure 4-2	Outdoor-outdoor propagation measurements setup for the Facebook sounder nodes outside urban Monumental Plaza in Athens, Greece, sounder nodes are mounted on a street lamp post at a height of 2.7m... .... 70

TABLE OF FIGURES

Figure 4-3 Outdoor-outdoor propagation measurements setup for the Facebook sounder nodes in suburban environment, where one sounder is mounted on a commercial telecom provider COSMOTE’s tower and the second node is on the roof of a moving SUV..... 70

Figure 4-4 Outdoor-outdoor propagation measurements setup for the Facebook sounder nodes in urban environment outside monumental plaza, where both sounder nodes are mounted on lamp posts. The measurements are carried out across a water fountain to see the reflections and the scattering. .... 71

Figure 4-5 Measured Pathloss between Tx and Rx over different distances, compared with FSPL and 2-Ray Pathloss models for: (a) Indoor (b) Outdoor urban-Pole to lamp-poles (c) Suburban..... 73

Figure 4-6 The cumulative distribution function (CDF) of pathloss for indoor, outdoor urban and suburban scenarios. .... 73

Figure 4-7 The number of useful links in different scenarios when the SNR is greater than 5dB..... 73

Figure 4-8 Outdoor-Indoor Measurements setup: (a) from street terminal to balcony behind foliage (b) from street terminal to inside terminal behind foliage and the windows. .... 76

Figure 4-9 Top and the front view of the residence building (R4), total distance is 240 meters (-104 to 136m) moving from left to the right side of the building. .... 77

Figure 4-10 Left and right side of the street facing the building R4. .... 77

Figure 4-11 Path gain measured in the street from left to right side against the distances for R4 when the receiver is placed at 1<sup>st</sup> floor in the balcony (1m away from the railing). Tx is at 3.5 height, Rx is placed in the balcony at a height difference of 1.65m. Vegetation depth is 4m and the street distance is 3m. .... 78

Figure 4-12 Over the top measurements’ scenario where Tx is placed at a height of 3.5m and  $w = 10.5\text{m}$  away from the Rx. .... 79

Figure 4-13 Top and front views of the external apartments. The total length of the street is 130m to the left side and 196m to the right side. .... 80

Figure 4-14 Left and right side of the view of street while looking from the balcony at 3<sup>rd</sup> floor. .... 80

Figure 4-15 Path gain measured versus the distance for R4 and external apartments (EA): (a) Receiver is on the 4th floor of the R4 building, (b) receiver is on the 3rd floor of the EA (c) receiver is at 4<sup>th</sup> floor of EA building. 82

Figure 4-16 Outdoor-Indoor measurements setup scenario, Rx is placed inside the lounge and 1m away from the glass window. .... 83

Figure 4-17 Outdoor-Indoor path gain versus the distance: (a) Rx is placed inside the dorm R4 on the 1st floor (b) Rx is at 4<sup>th</sup> floor of EA and inside the apartment, Rx is placed 1m away from the glass window in both cases. .... 85

TABLE OF FIGURES

Figure 5-1 FIREMAN setup..... 95

Figure 5-2 Access point omni antennas replaced with MAMP antenna array..... 95

Figure 5-3 Positions of the Raspberry Pi's in the SWiFT Lab..... 96

Figure 5-4 GUI which shows the connected sensor nodes, displaying the respective temperatures and the transmission powers..... 96

Figure 5-5 Received signal strength at the access point using MAMP antenna array: (a) the MAMP was directed towards Pi-2 (b) MAMP array was directed towards Pi-5..... 97

Figure 5-6 MAMP antenna connected to eNodeB (transmitter unit). The srsRAN eNodeB server debug log is visible in the background..... 99

Figure 5-7 Transmitter-Receiver setup for the power measurements using SDRangel..... 102

Figure 5-8 Received power at the USRP b210 using SDRAngel software when both transmitter and the receiver are tuned at 2.4GHz frequency; (a) spectrum of the DVB-S transmitting channel at 2.4GHz when omni antenna is transmitting (b) received power and the constellation when an omni antenna is transmitting (c) spectrum of the DVB-S transmitting channel at 2.4GHz when MAMP antenna is transmitting (d) received power and constellation is shown when MAMP antenna is transmitting ..... 104

Figure 5-9 Received power at the USRP b210 using SDRAngel software when both transmitter and the receiver are tuned at 2.4GHz frequency; (a) spectrum of the DVB-S transmitting channel at 2.4GHz when omni antenna is transmitting (b) received power and the constellation when an omni antenna is transmitting (c) spectrum of the DVB-S transmitting channel at 2.4GHz when MAMP antenna is transmitting (d) received power and constellation is shown when MAMP antenna is transmitting ..... 107



# CHAPTER 1. INTRODUCTION

## 1.1. BACKGROUND

Wireless communication systems provide the most cost-effective solution for communications in the present world as opposed to the high-cost cable networks based on cables. The wireless system has eliminated the need for high expenditures associated to laying cables between the base stations and the core network. Due to a plethora of applications, for instance, smart streets, smart homes, Internet-of-Things-based sensors, mobile devices, which are heavily dependent on the power grid, the demand for wireless systems is on the rise. To meet the high demands of these applications, an energy-autonomous and portable wireless network is required. These portable networks, which are self-energy-dependent, offer extra agility and performance gains to wireless communication systems. Although highly efficient and revolutionary, these systems pose massive challenges to the field of wireless networks.

Our motivation behind this research is to enable maximum coverage in all types of scenarios, such as fixed wireless networks using street furniture, emergencies, disasters, special events' areas, and remote areas that are affected by problematic infrastructure.

This research aims to provide an energy-efficient and portable network solution which is self-subsistent and scalable to satisfy the high future demands with minimal infrastructure. To aid the land-based network that suffers from congestion and communication failure, a broadly investigated solution is using unmanned aerial vehicles (UAVs) or fixed wireless. A self-backhauled base station can either be mounted on a UAV, it could be docked on a rooftop, or it could be mounted on a lamp post in a street for fixed wireless communications. This base station must deal with two major challenges: access network and backhaul.

## 1.2. STATE OF THE ART

### 1.2.1. SELF-BACKHAUL

Self-backhaul is defined as a network consisting of an integrated access and backhaul where both access and the backhaul use the same channel. An access link is a connection between a base station (BS) and the user equipment (UE) whereas backhaul is a link between either multiple base stations or between a BS and core network which is based on optic fiber. A schematic of a self-backhaul architecture is shown in Figure 1-1, where base stations are connected through wireless backhaul and one of them is linked with the core network over optical fiber.

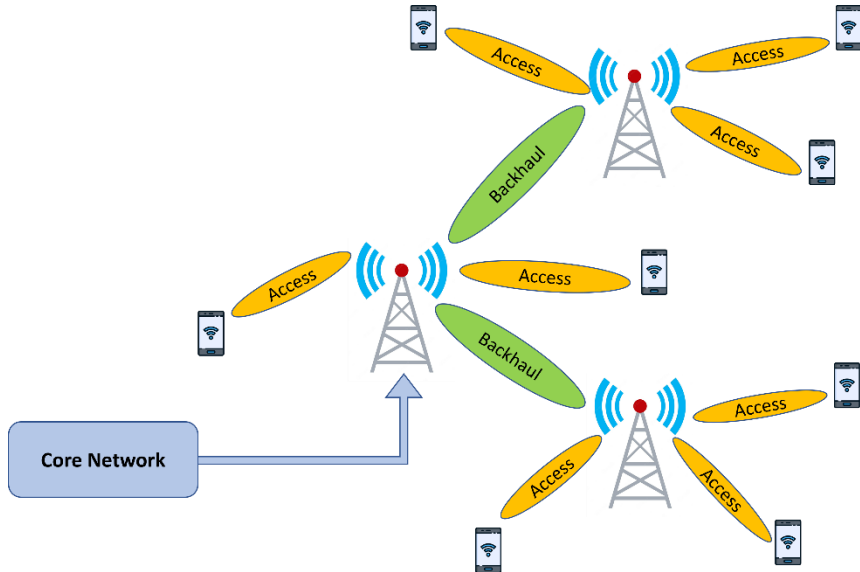


Figure 1-1 Self-backhaul architecture.

Self-backhauling is highly cost effective and due to its huge advantages, it was added by 3GPP in fifth generation (5G) New Radio release 15 as a topic for research and study. The cost can be reduced by avoiding the highly expensive fiber cables, the deployment cost and without bothering the street infrastructure. It is more beneficial for small cell architecture as recommended for 5G and adds more flexibility in the deployment. As the access and the backhaul share the same channel resources, the additional cost of purchasing a licensed spectrum can be avoided. Owing to the tremendous increase in data traffic growth and small base stations, the need for wireless backhauling has immensely increased. To meet the increasing demand for managing data traffic, many solutions have come to the forefront. One such technology is full duplex (FD), which simultaneously allows two-way traffic, transmission and reception, on the same frequency band thereby doubling the spectral efficiency; however, intercell interference has been disregarded and needs more attention [1]. One strategy to reduce self-backhaul delay, decrease interference and increase self-backhaul rate would be to apply Multiple Input Multiple Output (MIMO) antenna array at Macro Base Stations though it yields higher power consumption due to converters and the circuitry involved in radio frequency (RF) assembly. Generally, the cost and power consumption increase exponentially for the ideal hardware equipment with a large resolution. Moreover, for wideband mm-Wave MIMO systems, the power dissipated per conversion step (figure of merit – FoM) increases dramatically for sampling rates higher than about 1000MHz. For greener purposes, it will be highly important to look for ways of improving energy efficiency in MIMO-enabled macro base stations while maintaining system performance [2].

Another solution to cope with the exceeding data traffic demands is the use of small access points (SAPs). SAPs operate at the same frequency band with the same access technology. Similarly, they work at different frequency bands with different access technologies. These networks consisting of different kinds of base stations with various sizes are referred to as heterogeneous networks. These networks are great solutions for providing a better quality of service and cater to an enormous number of users. SAPs are connected to the core network via either a wired or a wireless link. SAP solves the issue of high costs linked to using wired backhaul links that use optical transmission technology and microwave backhaul links that require extra frequency bands. SAP is capable of communicating with a macro base station utilizing the same frequency band that it uses for the user equipments (UEs). A self-backhauled SAP uses the same channel for both access and backhaul thereby cutting the costs and capital expenditures. The efficiency of self-backhauling is enhanced when it is combined with FD [3–4]. There is scarcity in the spectrum bands below 6GHz, authors in [5–6] focused on mmWaves and integrated wideband channels for multiple backhaul and access links. Time, frequency, and power resources allocation was addressed in [7–8] for self-backhauling. UE rates and energy efficiency can be maximized by an optimized proportion of FD small cells; authors used stochastic geometry to find the coverage probability and the optimized ratio [9–10]. A comparison of two 5G massive MIMO (mMIMO) architectures is given in [11], where mMIMO direct access outperforms self-backhaul above the median of the UE rates due to line of sight (LoS) probability.

### 1.2.2. MASSIVE MIMO

One of the greatest technological innovations of all time is mobile computing. The explosive growth in the use of smartphones has been tremendous. As the use of connected devices, i.e. the Internet of Things is on the rise, the need for 5G networks has become imperative. There are three pivotal technologies that have been potentially considered for this goal such as mmWave mobile broadband, mMIMO, and small cells [1–2, 4]. Each of these technologies has its own challenges and no single technology can provide a 1000x increase in capacity. mmWave carrier frequencies need new spectrum allocations. Both mmWave and MIMO are in need of new hardware before they can be commercialized. Small cells are challenged by site acquisition and backhaul. One cost-efficient solution for implementing antenna arrays with large numbers of elements in mmWave frequencies can be patch antenna arrays. For frequencies in the range of 10–100 GHz, the dimension of the antenna elements is on the order of a few millimeters, which is easy to manufacture on printed circuit boards (PCBs). This significantly reduces the cost of antenna arrays. However, the loss of the antenna feed network on a PCB limits the dimension of the antenna arrays [4].

Phase arrays have the unique ability to produce a beam of radio waves by utilizing phase shifts. A major flaw of phased arrays is that usually a single beam is produced at a time.

In contrast to phased arrays, digital beamforming generates individually steerable multiple beams. Although advantageous for many applications, a digital beamformer can render high cost and power consumption. Hybrid beamforming, as the name suggests, is a fusion of both analog and digital beamforming domains. This approach does not take an individual antenna as an independent element; instead, it divides a large antenna array into smaller subarrays. In 5G literature, this is considered as an array of subarrays (AOSA). The working involves precoding a set of input data streams as in digital beamforming. These precoded streams are fed to individual analog beamformers or subarrays. The stream at each subarray undergoes phase shifting to produce a beam only from that subarray, which is ultimately directed at the end user. The total number of subarrays from the whole array determines the degrees of freedom (DoF) of the array. Employing analog subarrays in large antenna arrays significantly reduces costs due to a few numbers of complex RF chains required to form the beams. However, a drawback of hybrid beamforming is that the number of simultaneously supported data streams in a hybrid array is lower as compared to a full digital array. The design of the actual array is dictated by the beamforming capabilities as well as the complexity of the system and the budget [13]. A reduction in the number of RF chains also directly limits the number of data streams and user performance can be improved so that it matches the performance of a full digital beamformer.

Massive MIMO, a large-scale antenna system, is a wireless technology that is quite significant in 5G cellular networks. It employs several transmit and receive antennas by a few orders of magnitude compared to conventional MIMO to increase array gain and spectral efficiency. mMIMO originated from multi-user MIMO (MU-MIMO) and offers vast DoF. mMIMO and MU-MIMO can be employed by using beamforming techniques if channel state information (CSI) is available [14]. The biggest motivation behind using massive MIMO for self-backhaul is that it is very difficult to operate with optical fibers in some situations, where mMIMO can support high speed communication because of the high gain of the array.

### **1.2.3. PARASITIC ANTENNA ARRAYS**

Over the past two decades, there was a significant research activity on the side of multiple input / multiple output systems. The field has made great progress whether it's channel characterization or multi antenna configurations, but the MIMO systems have been scarcely made available to wireless user terminals [15]. This is due to the cost and higher power consumption of MIMO systems. The demand for high speed and reliable communications has shifted the focus towards mmWaves because of the wide bandwidth. mmWaves face issues due to obstacles and large distance path losses, so scientists prompt towards MIMO systems thus increasing the capacity, spectral efficiency and also the reliability of links. The multiple streams on MIMO channels require multiple or their own RF chain for the baseband processing thus increasing the size, cost, and

power dissipation of the units. This system may require three types of antenna systems, 1) all active 2) phased array and 3) parasitic antenna array. In all active antenna elements case, it is not a recommended solution due to cost, weight and the size of the array. As each antenna element requires a dedicated RF chain which increases hardware complexity. The more suitable way is to achieve the beamforming is using phased arrays. Hybrid beamforming is recommended using phased arrays. the phased array uses phase shifters and RF chains for the further baseband processing which again increases the cost and weight of the system. Phased arrays can be used to achieve coarse beams and are restricted to (5-6) bits because of the size and also that it is combination of subset of possible desired solutions. To cater to the problem, a new paradigm was made by using parasitic antenna arrays. The idea came from the fixed analog conventional Yagi-Uda antenna, where one active element is being fed and the beam is directed with the help of neighboring passive elements (directors). It was then equipped with mixed digital and analog processing techniques to do MIMO communications by using parasitic elements. PAAs use only reactive loads and can be tuned using varactors for different configurations. It eliminates the complex phase shifters and gives extra degree of freedom.

There are studies and research found on sparse antennas in past few years. The motivation behind sparse antennas is the reduction of size and cost of array structures. These are mostly used for RADAR and satellite communications, but the RF chains are still in a large number due to a large number of radiating elements, when considered in sparse representations. The other challenge of sparse arrays is antenna synthesis, where location, amplitude and phase of each radiating element is optimized and then the aim of synthesizing the desired radiation pattern with a minimum number of radiated antenna elements. The sparse structure enables the possibility to host many radiating elements and on the other hand, it has to manage the problem of initial user access. It must avoid too long searching procedures for identifying the region of user space.

It is entirely possible to get a comparable performance to a conventional MIMO by using parasitic antenna arrays and with a reduced number of RF chains. The phenomenon that allows this advantage is the mutual coupling among the neighboring elements of the array [16]. Where one element is excited and is called an active element and it induces currents on its neighboring elements called parasitic elements placed in close vicinity. Many precoding schemes and algorithms such as beam space models, MUSIC, ESPRIT and beamforming have been introduced to utilize this technique for MIMO communications [19–28]. The only drawback with those models and techniques was that they used single active and multi parasitic elements. To enhance the performance of the proposed system, multi active and multi passive parasitic antenna arrays (MAMP-PAA) were introduced, where the number of active elements is increased and thus the number of parasitic elements is also increased. The performance of the MAMP arrays is significant and comparable to the conventional MIMO systems but with reduced number of RF chains [32–33, 41].

An improved version of the previously developed stochastic beamforming algorithm is presented in this thesis for the computation of load values for parasitic elements. It can guide the algorithm to make sure that the array radiates based on the newly developed radiation conditions. The algorithm was based on the comparison of the ideal beam produced by a conventional uniform linear array (ULA) to that of a newly produced MAMP array, but due to the mutual coupling among the elements of the array, it is possible to have negative input impedance at some of the active elements. New constraints are introduced to make sure that the whole array radiates, and that the efficiency of the array is sufficient to carry out the transmission. Another drawback was that it could produce the negative real parts of the passive components (which means the negative resistance and corresponds to the stability of the system) which is not feasible to implement in real time. So, the proposed algorithm can generate positive load values, with high efficiency, making the whole array radiate and also in good comparison of radiation pattern to the ULA. Discrete angle resolution can be achieved using a combination of phased arrays and PAAs [42]. Where, phased array provides coarse beam scanning, and it can be fine tuned using PAAs. This may reduce the number of RF chains and the hardware complexity of the system.

### 1.3. PH.D. PROJECT OBJECTIVES

The study will focus on microwave and cmWave frequencies, which allow wide bandwidth, as well as on adaptive energy efficient, highly directional and narrow beam antenna arrays and possibly new channel models at such frequencies, in order to tackle the propagation and interference environment encountered by the portable access points. The latter will have to be modeled according to the scenarios of interest, whereas the derived techniques and solutions will have to be robust to the frequency selectivity of the wideband propagation channel.

The main objectives of the proposed research are:

#### **Obj. 1. Definition and modeling of hybrid antenna architectures.**

- To develop energy-efficient antenna arrays for fixed wireless communications (phased array based mMIMO, all active antenna elements, MAMP-PAAs, etc.).
- To incorporate a highly directional and narrow beam antenna array for the backhaul.
- Modeling of the mutual coupling for the proposed antenna array architecture.

#### **Obj. 2. Channel and signal modeling for microwave and mmWave backhaul links.**

- The development of statistical channel models based on the narrowest beam for portable access points in urban/suburban environments focusing on the

propagation characteristics of cmWaves, penetration loss, Doppler and multipath.

- To integrate the developed antenna architecture with the new channel model for the backhauling of the considered setup.

### **Obj. 3. Development of algorithms for adaptive beamforming.**

- To develop an algorithm for steerable beams for the considered setup.
- The developed techniques and algorithm that must incorporate the radiation conditions and radiation efficiency of the array.

### **Obj. 4. Performance analysis of the developed adaptive backhauling techniques over a physical layer.**

- Developed prototype will be integrated with an application to show the proof of concept.
- Universal Software Radio Peripheral (USRP) and RF front ends will be used for the performance evaluation of the developed Antenna array over 4G/5G physical layer.

## **1.4. KEY METHODS**

The motivation comes from the scenario of EU's project PAINLESS, where a flying wifi is manifested. The use of portable access points (PAP's) or unmanned aerial vehicles (UAV's) serving as data relays / base stations holds significant importance for delivering on-demand connectivity as well as providing public safety services or aiding in recovery after communication infrastructure failures caused by natural disasters. In-case of a disaster, the whole network could be out of service resulting in an outage of communication links. The demand for high speed and reliable communication has brought new solutions in terms of 5G and beyond where most of the focus is using small cell deployments due to shorter wavelengths (mmWaves) for self-backhauled base stations. PAPs could be utilized to solve the problem by mounting small cell base stations on it. The Deployment of such base stations can face some restrictions that need to be considered such as the availability of reliable wireless backhaul links to transfer all the traffic to the core network from the targeted area. Since these small cells will have to operate in different environments (e.g. urban / suburban / rural, high/low height, high/low interference, special venues such as sports or emergency sites, etc.), it is important that their wireless backhaul and access links are adaptive to such conditions. These small cells are self-backhauled, and they can be mounted on a drone, or they can be fixed on a streetlamp post. At mmWaves small cells can face two serious issues i.e., coverage for long distances and interference from other base stations. In order to satisfy the needs of the proposed network, a base station is considered that benefits from highly directional antennas with narrow beamwidth and adaptive precoding schemes. To cope up with the challenges of wireless backhaul, microwave and mmWave massive MIMO

communication is considered for hybrid transceivers. To reduce the complexity of RF chains being used in beamforming, parasitic antenna arrays are considered that may include a combination of active antenna elements, passive elements as well as phase shifters for sub 6GHz and mmWave frequencies.

After thoroughly surveying the literature and sketching the current state of affairs which include basic principles of backhauling, access links and antenna array systems, an antenna array architecture is defined based on the proposed objectives in section 1.3. The study focusses on the design and development of multi-active / multi-passive parasitic antenna array. The MAMP array is designed and analyzed by using different examples. Some key factors and limitations are discussed, for example, the negative impedance and the impact of negative impedance on the performance of a MAMP array, the negative load values, beam steering and the radiation efficiency of the array. The performance of the array is analyzed and the solutions to the formulated problems are produced in the upcoming chapters. Beamforming is used as a precoding scheme and a stochastic beamforming algorithm (SBA) is used to design and analyze the MAMP array. The SBA computes load values (which are reactive loads i.e., capacitors and inductors) along with the weights. The algorithm optimizes the load values by reducing the error between the ideal radiation pattern and a proposed radiation pattern produced by the MAMP array. It considers a uniform linear array (ULA) with ideal half-wave dipoles and point sources in MATLAB. Algorithm is developed using adequate robust optimization methods with necessary modifications. New radiation conditions are developed and integrated to the SBA to optimize the array performance.

The MAMP array is emulated in simulation software using antenna tool simulators such as high-frequency structure simulator (HFSS) and CST microwave studio. Different MAMPs are developed in CST to compare the results. The computed loads are integrated in the simulations and then the comparison is shown in the following chapters. At first, it is shown that the radiation conditions are key for improving the MAMP array performance, by considering the input impedance as a key factor. The array performance is shown by producing the examples with negative and positive input impedance. Later, recognizing that these conditions do not always suffice for the MAMP array to radiate as a whole, new radiation conditions are produced which are based on the overall radiation efficiency of the array. A new cost function is introduced in the SBA algorithm and new load values are computed. These values are integrated in the simulations and the results are compared. Beamforming is chosen as a precoding scheme and the examples are shown with different beam angles i.e.,  $60^\circ$ ,  $90^\circ$  and  $120^\circ$ . Calculated and simulated results are compared for the analysis of array performance.

To provide a proof-of-concept, a 2-active/12-parasitic MAMP array is developed and prototyped, steering the beam towards  $90^\circ$ . The 2-active (2-RF chains) array is developed so it can be integrated with the equipment in the lab. The lab's software-defined radio modules (USRPs), as well as the lab's IoT testbed, each have only 2 RF ports, so the prototype design is limited to 2-active elements. The designed MAMP array is measured using a network analyzer and in an anechoic chamber. Simulated and measures results

are in good match. The developed MAMP array is integrated with the available equipment in the SWiFT lab for the proof of concept.

Channel modeling is envisioned using the proposed MAMP antenna array and is a core objective of this research study. A MAMP array design is obstructed by the limitations of mutual coupling at mmWave frequencies. The wavelength is very short at such high frequencies, which causes difficulties for the development of a MAMP array. As in MAMP the parasitic elements are meant to be placed in close vicinity (at fractions of the wavelength) to increase the mutual coupling, at higher frequencies the distance between the neighboring elements is extremely small, it can even interrupt the near field of the elements. Channels are measured using a horn antenna operating at 60GHz. The outdoor to indoor scenarios are considered where a base station is mounted on a lamp post at certain height and is transmitting inside a building through a glass window and vegetation. Different scenarios are considered, and path gain is shown to analyze the performance at mmWaves for an envisioned fixed wireless communication setup.

The MAMP array is integrated with the USRPs to see the performance in real time scenarios. USRPs B210 are configured to a 4G/5G setup. Some experiments are performed for 4G communication using MAMP array for a backhaul link and the data rate is analyzed. Another experiment is performed using an IoT testbed, where an access point is used as a data collection hub and collects data from multiple sensor nodes. The MAMP array is integrated with the access point and the RSSI is measured to see the power as a key factor. The concept is to increase the battery lifetime at the sensors by increasing the Rx gain. As the MAMP array has a higher gain and is pointing towards the desired node, it thus reduces the transmitting power at the respective node and increases the battery life.

A performance analysis of the prototype has been performed for the comparison between the proposed techniques and the existing state-of-the-art architectures. To improve the required skills and knowledge regarding the stated objectives, seminars and summer / winter schools, conferences were attended. As part of the doctorate, the requirement of credit hours was fulfilled at Aalborg University, Denmark. The project outcomes were disseminated in peer-reviewed journals and conferences. The dissertation is being submitted to the Electronics Department of Aalborg University, Denmark.

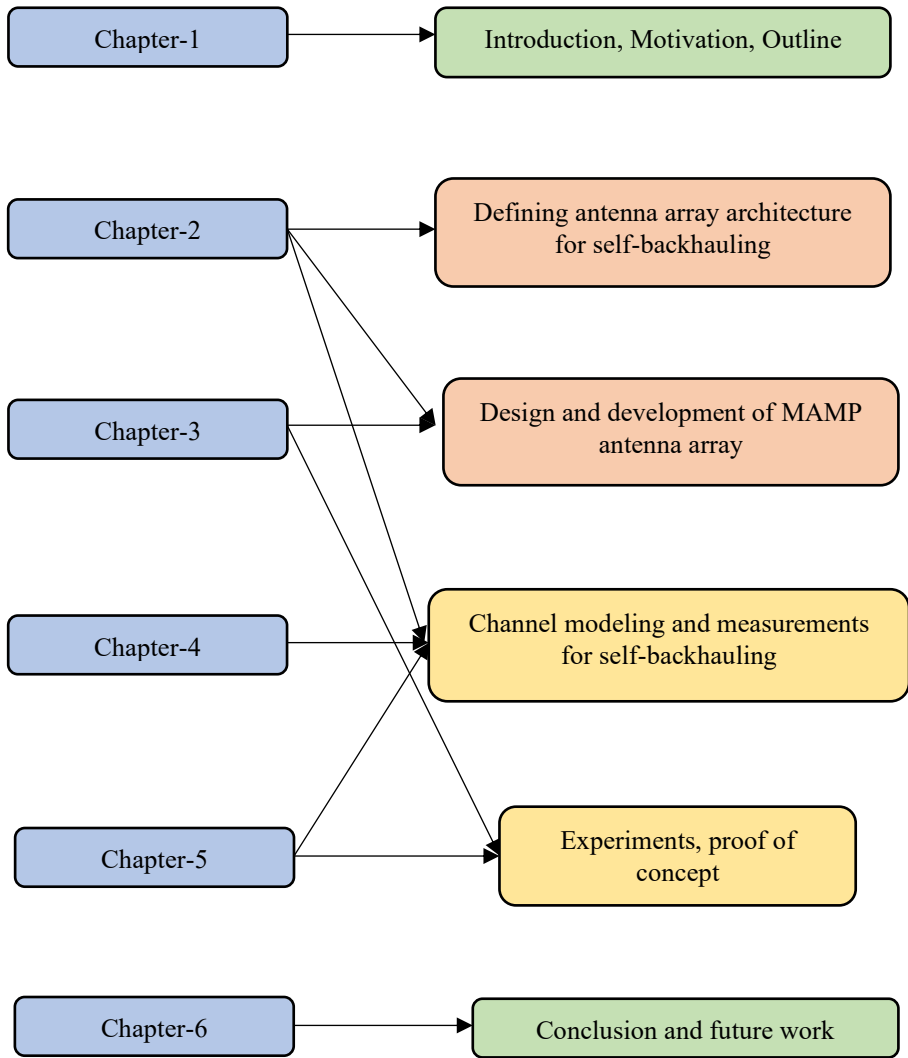


Figure 1-2 Roadmap of the thesis

## 1.5. SIGNIFICANCE AND OUTCOME

The future demands for energy-autonomous, infrastructure-less networks have increased with the demands of high-speed data communications. This has led the research community to focus on an interesting topic of energy-autonomous portable access points. The new research fascination is with no wires, no contacts, no batteries, and reliable energy supply, but the challenges also emerge to provide autonomous power networks and energy limited communication devices.

By the end, we expect to have the following outcomes:

- Design of energy-efficient antenna arrays for the self-backhaul wireless access points. The research community has widely acknowledged the multiple-input multiple-output systems as a promising technology for future wireless networks. Therefore, different precoding schemes and techniques have been studied widely for the energy and cost efficiency of the devices. One of the challenges as compared to 4G and LTE networks, especially in view of massive MIMO is to assign a dedicated RF chain for every antenna element. This one RF chain includes the digital-to-analog (D/A) / analog-to-digital (A/D) converter, signal mixer and power amplifier to each antenna element, in light of the state-of-the-art hardware implementation techniques and energy consumptions. Parasitic Antenna Arrays (PAAs) have been used to enable new trends and paradigms for multi-antenna transmission with a single RF chain. The reduction of RF chains results in significantly lower energy consumption, hardware complexity, size and cost of RF circuits.
- Development of an algorithm for beamforming using reduced number of RF chains. The constraints are to set the conditions for all or any of the active elements in arrays to radiate which before this work has not been addressed. The motivation behind this work is the reduction in the number of RF chains thus reducing the cost and size of the arrays by eliminating the assembly behind each RF chain consisting of filters, ADC, DAC amplifiers, etc. The high gain and high directivity beams can be achieved in desired directions using MAMPs by only tuning loads at parasitic elements, also with a reduced number of RF chains, low cost, and complexity. The array performance can be optimized based on radiation efficiency of the array.
- Performance evaluation of the derived techniques over 5G/4G physical layer. Using an over the air testbed the antenna performance can be analyzed to see the real time scenarios for future wireless communications.

- cmWave propagation measurements and channel modeling for fixed wireless communications. It would be extremely important for the development of channel models for 5G and beyond technologies, where street furniture, smart cities and drones will be connected wirelessly and providing gigabit per seconds. For the environments to provide such data rates and reliable communication at such higher frequencies it is desired to know the signal behavior in terms of signal losses at higher distances, and the fading effects due to vegetation, walls, obstacles, glass windows and traffic in real life scenarios.

## 1.6. THESIS OUTLINE AND CONTRIBUTIONS

### Chapter 2: System Architecture and Design Guidelines

The antenna array architecture is defined based on the newly developed guidelines. The parasitic antenna arrays are introduced with multi-active / multi-passive elements to replace the MIMO systems. Some radiation conditions are introduced in this chapter which ensure the radiation at the feeding ports of the array. The conditions are integrated into a previously developed alternating optimization stochastic beamforming algorithm (AO-SBA). This algorithm computes the load values for parasitic elements and then the integration of these constraints is verified by some examples using CST microwave studio simulations. The content in this chapter is based on material in:

- M. H. Tariq, D. K. Ntaikos and C. B. Papadias, "Design Guidelines for Multi-Active/Multi-Passive Parasitic Antenna Arrays," in *IEEE Antennas and Wireless Propagation Letters*, vol. 19, no. 12, pp. 2141-2144, Dec. 2020, doi: 10.1109/LAWP.2020.3024803.

### Chapter 3: MAMPs Techniques and Evaluation

The radiation conditions developed in chapter I are not enough and do not suffice the requirements of the MAMPs. So new radiation conditions are developed based on the radiation efficiency of the array. The antenna array is developed using the SBA and new constraints are integrated into the algorithm. Hybrid beamforming techniques are developed in this chapter and MAMP array is produced using CST simulations and later antenna array prototype was developed to showcase the proof of concept. A comparison is given between the simulated and the measured results of the array. The loads are computed using the SBA and the antenna was developed by a team at University College London (UCL), where the MAMP was fabricated, components were embedded and then the prototype was measured in an anechoic chamber at the Intracom Defense (IDE), Greece. The material in this chapter is obtained from the article below.

- Muhammad Haroon Tariq, Constantinos B. Papadias, Shuai Zhang, Christos Masouros, “Energy Efficient Hybrid Beamforming Using Multi-Active/Multi-Passive Parasitic Antenna Arrays for portable access points”, *IEEE Transactions on Aerospace and Electronic Systems*, January 2024 (Submitted)

#### Chapter 4: Propagation Measurements and Channel Modeling

Channel measurements were performed in different phases in Athens using different equipment. In the first phase, the analysis is shown for the channel measurements using Terragraph Sounder nodes provided by Facebook. Outdoor to indoor, outdoor to outdoor measurements were performed in a commercial plaza located in Athens, Greece. The sounders have a very narrow beam and operate at 60GHz.

After a series of campaigns in Athens, a channel model is developed for the propagation of cmWaves (60 GHz). The cmWave channel measurements are performed on campus and off campus using the equipment provided by NOKIA Bell Labs. The system consists of two sounder nodes and a GUI to collect the data. The transmitter is a prototyped Omni antenna, and the receiver is a horn, both operating at 60GHz. The measurements consist of outdoor to indoor multiple scenarios at multiple locations in Athens, Greece. Based on these channel measurements, a channel model is developed for future fixed wireless communications using the street furniture. The chapter includes the material in:

- Muhammad Haroon Tariq, Iason Grivas, Constantinos B. Papadias, Jinfeng Du, Dmitry Chizhik and Reinaldo Valenzuela, Mauricio Rodríguez, Rodolfo Feick, “mmWave Channel Measurements and Modeling for Outdoor to Indoor Fixed Wireless Communications”, *IEEE Transactions of Antennas and Propagation (TAP)*, January 2024 (Not submitted yet)
- Nikolaos Ntetsikas, Nithin Babu, Muhammad Haroon Tariq, Constantinos B. Papadias, Jinfeng Du, Dmitry Chizhik and Reinaldo Valenzuela, Mauricio Rodríguez, Rodolfo Feick, “60 GHz Outdoor to Indoor (O2I) Propagation Measurements in a University Campus”, *SPAWC*, Oulu, Finland, 2022, pp. 1-5, doi: 10.1109/SPAWC51304.2022.9833968.
- Muhammad Haroon Tariq, I. Chondroulis, P. Skartsilas, N. Babu and C. B. Papadias, "mmWave Massive MIMO Channel Measurements for Fixed Wireless and Smart City Applications," 2020 IEEE 31st Annual *International Symposium on Personal, Indoor and Mobile Radio Communications*, London, UK, 2020, pp. 1-6, doi: 10.1109/PIMRC48278.2020.9217375.
- White Paper: Telecom Infra Project (TIP) Channel Sounder measurements for fixed wireless mmWave Networks Project Group, September 2020

## Chapter 5: Experiments and Proof of Concept Demos

The developed MAMP antenna array is used to show the proof of concept by using it for different applications. The prototype is used in the applications available in the Smart Wireless Future Technologies (SWiFT) lab at the American College of Greece.

- FIREMAN Demo for IoT Setup
  - It is a project funded by the EU for the development of IoT systems for the industry.
  - The MAMP prototype is integrated with the system for the IoT network, which showed improved performance for the multiple sensor nodes in the lab.
  - The MAMP is installed at the access point which connects to the network of sensor nodes. RSSI at each sensor node is shown using a GUI.
  
- Software Defined Radio Demo
  - The prototype is integrated with the existing 4G/5G radio systems in the lab.
  - Comparable performances are shown by integrating the MAMP with the USRPs to enable the 5G and 4G cellular services.
  - The received powers are obtained and displayed for the proof of concept and to analyze the performance of the MAMP antenna array.

## 1.7. REFERENCES

- [1] D. Yu, Y. Liu and H. Zhang, "Energy-Efficient Beamforming Design for User-Centric Full-Duplex Wireless Backhaul Networks," 2021 IEEE Global Communications Conference (GLOBECOM), Madrid, Spain, 2021, pp. 1-6, doi: 10.1109/GLOBECOM46510.2021.9685903.
- [2] X. Jia, W. Xu, Y. Chen and L. Yang, "Hybrid Self-Backhaul and Cache Assisted Millimeter Wave Two-Tier Heterogeneous Networks With MIMO Equipped Backhaul Access Points," in IEEE Access, vol. 7, pp. 59963-59983, 2019, doi: 10.1109/ACCESS.2019.2914694.
- [3] A. Rahmati, A. Sadeghi and V. Shah-Mansouri, "Price-based resource allocation for full duplex self-backhauled small cell networks," 2015 IEEE International Conference on Communications (ICC), London, UK, 2015, pp. 5709-5714, doi: 10.1109/ICC.2015.7249232.
- [4] Z. Pi, J. Choi and R. Heath, "Millimeter-wave gigabit broadband evolution toward 5G: fixed access and backhaul," in IEEE Communications Magazine, vol. 54, no. 4, pp. 138-144, April 2016, doi: 10.1109/MCOM.2016.7452278.
- [5] M. N. Kulkarni, J. G. Andrews and A. Ghosh, "Performance of Dynamic and Static TDD in Self-Backhauled Millimeter Wave Cellular Networks," in IEEE Transactions on Wireless Communications, vol. 16, no. 10, pp. 6460-6478, Oct. 2017, doi: 10.1109/TWC.2017.2723887.
- [6] S. Singh, M. N. Kulkarni, A. Ghosh and J. G. Andrews, "Tractable Model for Rate in Self-Backhauled Millimeter Wave Cellular Networks," in IEEE Journal on Selected Areas in Communications, vol. 33, no. 10, pp. 2196-2211, Oct. 2015, doi: 10.1109/JSAC.2015.2435357.
- [7] R. Gupta and S. Kalyanasundaram, "Resource allocation for self-backhauled networks with half-duplex small cells," 2017 IEEE International Conference on Communications Workshops (ICC Workshops), Paris, France, 2017, pp. 198-204, doi: 10.1109/ICCW.2017.7962657.
- [8] T. M. Nguyen, A. Yadav, W. Ajib and C. Assi, "Resource Allocation in Two-Tier Wireless Backhaul Heterogeneous Networks," in IEEE Transactions on Wireless Communications, vol. 15, no. 10, pp. 6690-6704, Oct. 2016, doi: 10.1109/TWC.2016.2587758.
- [9] A. Sharma, R. K. Ganti and J. K. Milleth, "Joint Backhaul-Access Analysis of Full Duplex Self-Backhauling Heterogeneous Networks," in IEEE Transactions on

- Wireless Communications, vol. 16, no. 3, pp. 1727-1740, March 2017, doi: 10.1109/TWC.2017.2653108.
- [10] H. Tabassum, A. H. Sakr and E. Hossain, "Analysis of Massive MIMO-Enabled Downlink Wireless Backhauling for Full-Duplex Small Cells," in IEEE Transactions on Communications, vol. 64, no. 6, pp. 2354-2369, June 2016, doi: 10.1109/TCOMM.2016.2555908.
- [11] H. H. Yang, G. Geraci and T. Q. S. Quek, "Energy-Efficient Design of MIMO Heterogeneous Networks With Wireless Backhaul," in IEEE Transactions on Wireless Communications, vol. 15, no. 7, pp. 4914-4927, July 2016, doi: 10.1109/TWC.2016.2549529.
- [12] A. Bonfante et al., "5G Massive MIMO Architectures: Self-Backhauled Small Cells Versus Direct Access," in IEEE Transactions on Vehicular Technology, vol. 68, no. 10, pp. 10003-10017, Oct. 2019, doi: 10.1109/TVT.2019.2937652.
- [13] Xiaojing Huang, Jay Guo, "Hybrid antenna array – A low cost energy efficient phased array", white paper: Platform Technologies, UTS:GBDTC Global Big Data Technologies Center.
- [14] Priya, T.S., Manish, K. & Prakasam, P. Hybrid Beamforming for Massive MIMO Using Rectangular Antenna Array Model in 5G Wireless Networks. Wireless Pers Commun 120, 2061–2083, 2021, <https://doi.org/10.1007/s11277-021-08455-7>.
- [15] C. A. Balanis, Antenna Theory: Analysis and Design, Hoboken, NJ, USA: Wiley, 2012.
- [16] D. M. Pozar, Microwave Engineering, Hoboken, NJ, USA: Wiley, 2012.
- [17] A. Komatsuzaki, S. Saito, K. Gyoda and T. Ohira, "Hamiltonian approach to reactance optimization in ESPAR antennas," 2000 Asia-Pacific Microwave Conference. Proceedings (Cat. No.00TH8522), Sydney, NSW, Australia, 2000, pp. 1514-1517, doi: 10.1109/APMC.2000.926125.
- [18] Jun Cheng, Y. Kamiya and T. Ohira, "Adaptive beamforming of ESPAR antenna using sequential perturbation," 2001 IEEE MTT-S International Microwave Symposium Digest (Cat. No.01CH37157), Phoenix, AZ, 2001, pp. 133-136 vol.1, doi: 10.1109/MWSYM.2001.966856.
- [19] Chen Sun, A. Hirata, T. Ohira and N. C. Karmakar, "Fast beamforming of electronically steerable parasitic array radiator antennas: theory and experiment," in IEEE Transactions on Antennas and Propagation, vol. 52, no. 7, pp. 1819-1832, July 2004, doi: 10.1109/TAP.2004.831314.

- [20] J. C. Bucheli Garcia, M. Kamoun and A. Sibille, "On the performance of ESPAR for spatial multiplexing in reception," 2019 IEEE Wireless Communications and Networking Conference (WCNC), Marrakesh, Morocco, 2019, pp. 1-5, doi: 10.1109/WCNC.2019.8885547.
- [21] A. Kalis, A. G. Kanatas and C. B. Papadias, "A Novel Approach to MIMO Transmission Using a Single RF Front End," in *IEEE Journal on Selected Areas in Communications*, vol. 26, no. 6, pp. 972-980, August 2008, doi: 10.1109/JSAC.2008.080813.
- [22] O. N. Alrabadi, C. B. Papadias, A. Kalis and R. Prasad, "A universal encoding scheme for MIMO transmission using a single active element for PSK modulation schemes," in *IEEE Transactions on Wireless Communications*, vol. 8, no. 10, pp. 5133-5142, October 2009, doi: 10.1109/TWC.2009.080824.
- [23] V. I. Barousis, A. G. Kanatas and A. Kalis, "Beamspace-Domain Analysis of Single-RF Front-End MIMO Systems," in *IEEE Transactions on Vehicular Technology*, vol. 60, no. 3, pp. 1195-1199, March 2011, doi: 10.1109/TVT.2011.2112383.
- [24] O. N. Alrabadi, J. Perruisseau-Carrier and A. Kalis, "MIMO Transmission Using a Single RF Source: Theory and Antenna Design," in *IEEE Transactions on Antennas and Propagation*, vol. 60, no. 2, pp. 654-664, Feb. 2012, doi: 10.1109/TAP.2011.2173429.
- [25] Chen Sun, Nemai Chandra Karmakar, "Direction of Arrival Estimation Based on a Single Port Smart Antenna Using MUSIC Algorithm with Periodic Signals", *EURASIP Journal on Applied Signal Processing* 2004:9, 1364-1375, HindawiPublishingCorporation, 2004.
- [26] E. Taillefer, A. Hirata and T. Ohira, "Reactance-domain ESPRIT algorithm for a hexagonally shaped seven-element ESPAR antenna," in *IEEE Transactions on Antennas and Propagation*, vol. 53, no. 11, pp. 3486-3495, Nov. 2005, doi: 10.1109/TAP.2005.858854.
- [27] V. I. Barousis and C. B. Papadias, "Arbitrary Precoding with Single-Fed Parasitic Arrays: Closed-Form Expressions and Design Guidelines," in *IEEE Wireless Communications Letters*, vol. 3, no. 2, pp. 229-232, April 2014, doi: 10.1109/WCL.2014.020614.130863.
- [28] L. Zhou, F. A. Khan, T. Ratnarajah and C. B. Papadias, "Achieving Arbitrary Signals Transmission Using a Single Radio Frequency Chain," in *IEEE Transactions on Communications*, vol. 63, no. 12, pp. 4865-4878, Dec. 2015, doi: 10.1109/TCOMM.2015.2493140.

- [29] A. Li, C. Masouros and C. B. Papadias, "MIMO Transmission for Single-Fed ESPAR With Quantized Loads," in *IEEE Transactions on Communications*, vol. 65, no. 7, pp. 2863-2876, July 2017, doi: 10.1109/TCOMM.2017.2692224.
- [30] L. Zhou, F. A. Khan, T. Ratnarajah and C. B. Papadias, "Single-RF Multi-Antenna Transmission With Peak Power Constraint," in *IEEE Transactions on Communications*, vol. 65, no. 12, pp. 5197-5208, Dec. 2017, doi: 10.1109/TCOMM.2017.2737981.
- [31] G. K. Papageorgiou, D. Ntaikos and C. B. Papadias, "Efficient Beamforming with Multi-Active Multi-Passive Antenna Arrays," 2018 IEEE 19th International Workshop on Signal Processing Advances in Wireless Communications (SPAWC), Kalamata, Greece, 2018, pp. 1-5, doi: 10.1109/SPAWC.2018.8445890.
- [32] M. H. Tariq, D. K. Ntaikos and C. B. Papadias, "Design Guidelines for Multi-Active/Multi-Passive Parasitic Antenna Arrays," in *IEEE Antennas and Wireless Propagation Letters*, vol. 19, no. 12, pp. 2141-2144, Dec. 2020, doi: 10.1109/LAWP.2020.3024803.
- [33] V. Barousis, A. G. Kanatas, A. Kalis and C. Papadias, "A Stochastic Beamforming Algorithm for ESPAR Antennas," in *IEEE Antennas and Wireless Propagation Letters*, vol. 7, pp. 745-748, 2008, doi: 10.1109/LAWP.2008.2004783.
- [34] M. Capek, L. Jelinek and M. Masek, "Finding Optimal Total Active Reflection Coefficient and Realized Gain for Multiport Lossy Antennas," in *IEEE Transactions on Antennas and Propagation*, vol. 69, no. 5, pp. 2481-2493, May 2021, doi: 10.1109/TAP.2020.3030941.
- [35] M. Wang, T. -H. Loh, Y. Zhao and Q. Xu, "A Closed-Form Formula of Radiation and Total Efficiency for Lossy Multiport Antennas," in *IEEE Antennas and Wireless Propagation Letters*, vol. 18, no. 12, pp. 2468-2472, Dec. 2019, doi: 10.1109/LAWP.2019.2940382.
- [36] V. I. Barousis, C. B. Papadias and R. R. Müller, "A new signal model for MIMO communication with compact parasitic arrays," 2014 6th International Symposium on Communications, Control and Signal Processing (ISCCSP), Athens, Greece, 2014, pp. 109-113, doi: 10.1109/ISCCSP.2014.6877828.
- [37] L. Zhou, F. A. Khan, T. Ratnarajah and C. B. Papadias, "Achieving Arbitrary Signals Transmission Using a Single Radio Frequency Chain," in *IEEE Transactions on Communications*, vol. 63, no. 12, pp. 4865-4878, Dec. 2015, doi: 10.1109/TCOMM.2015.2493140.

- [38] A. Li, C. Masouros and C. B. Papadias, "MIMO Transmission for Single-Fed ESPAR With Quantized Loads," in *IEEE Transactions on Communications*, vol. 65, no. 7, pp. 2863-2876, July 2017, doi: 10.1109/TCOMM.2017.2692224.
- [39] Y. Zhou, R. S. Adve and S. V. Hum, "Design and Evaluation of Pattern Reconfigurable Antennas for MIMO Applications," in *IEEE Transactions on Antennas and Propagation*, vol. 62, no. 3, pp. 1084-1092, March 2014, doi: 10.1109/TAP.2013.2284874.
- [40] G. K. Papageorgiou, M. Sellathurai, D. K. Ntaikos and C. B. Papadias, "3D Beamforming with Multi-Active Multi-Passive Antenna Arrays Using Stochastic Optimization," 2020 IEEE 21st International Workshop on Signal Processing Advances in Wireless Communications (SPAWC), Atlanta, GA, USA, 2020, pp. 1-5, doi: 10.1109/SPAWC48557.2020.9154231.
- [41] L. Wang, K. -K. Wong, S. Lambotharan, A. Nallanathan and M. ElKashlan, "Edge Caching in Dense Heterogeneous Cellular Networks With Massive MIMO-Aided Self-Backhaul," in *IEEE Transactions on Wireless Communications*, vol. 17, no. 9, pp. 6360-6372, Sept. 2018, doi: 10.1109/TWC.2018.2859936.
- [42] I. E. Uchendu, J. R. Kelly, R. Mitra and Y. Gao, "Hybrid Parasitic Linear Array Antenna for Fine Beamsteering Applications," in *IEEE Access*, vol. 9, pp. 84899-84909, 2021, doi: 10.1109/ACCESS.2021.3088405.



# CHAPTER 2. DESIGN GUIDELINES AND RADIATION CONDITIONS

Parasitic antenna arrays (PAAs) with a single radio frequency (RF) chain have been employed to bring forth novel paradigms for multi-antenna transmission. The advantage of using single RF PAAs is that they can lead to significant decrease in hardware complexity, cost, size, and weight. This is because only the active element (AE) has a direct voltage feeding connection using an SMA connector. Moreover, the performance of a PAA can be significantly enhanced by just increasing the active elements in PAAs. This setup will establish a multi-active / multi-passive (MAMP) antenna array, where parasitic elements depend upon the load values and are grounded through via holes. The major challenge for a MAMP array is to find the right tunable loads for parasitic elements (PE) which ensure that the array will radiate.

## 2.1. INTRODUCTION

The research in the field of wireless communications is becoming increasingly prosperous due to the huge demand of wirelessly connected devices. These devices need high speed data rates and a reliable connection with significantly low latencies. To overcome user demands, scientists have proposed a huge number of antenna elements for diversity and high gain over the transmission channels. The increased number of antenna elements results in more complex systems and increased cost and size. To improve the performance tradeoffs in modern wireless communication systems, researchers have shown interest in PAAs. PAAs have reduced cost, size, and weight as compared to conventional antenna arrays. They work on the principle of mutual coupling, where an active element is connected through RF connection, and it induces currents on neighboring elements that are placed close to the active element [1–3]. This induced current is due to the mutual coupling among the elements which depends upon the geometry of the array and also the inter element distance. Considering the fact that the radiation pattern of an array is derived by the superposition of all the elements of its array, a beam or specific radiation pattern can be achieved in a desired / particular direction by just tuning the loads on the parasitic elements. Single-RF transmission was in focus in the previous works and many techniques and arbitrary schemes were introduced for signal models and derivation of loads. It consisted of beam-space [4–7] models initially where radiation of the array is based on the ad-hoc approach because it does not involve any conditions that ensure the radiation of the array. Some design guidelines are presented in [8] for single-active / multi-passive (SAMP) PAAs which indeed ensure that the array will radiate. Another signal model is presented in [9], where arbitrary precoding schemes [10–11] are shown that derive the loads while incorporating the radiation conditions for SAMPs. Since MAMPs have not been addressed vastly and lack the design guidelines, we have derived radiation conditions in the closed form that ensure the radiation of the MAMP array [12].

This chapter provides (for the first time at the time of its publication) closed-form expressions [12] to be incorporated in the algorithm (AO-SBA) to compute the load values. These values are incorporated in a MAMP array to ensure that the array radiates. It is shown with examples by designing MAMP array in CST microwave studio. A comparison of radiation patterns is given by emulating two different MAMPs. One of them is not subject to any conditions and the other is taking into account the radiation conditions.

## 2.2. PAA LOADS AND COUPLING MATRIX

To ensure strong electromagnetic coupling, PEs have to be placed in close vicinity of the active element in a SAMP array. A MAMP can be produced when several SAMP arrays are placed close to each other (theoretically the distance is  $0.5\lambda$  to avoid coupling), in this case the mutual coupling is experienced by all the elements of the PAA.

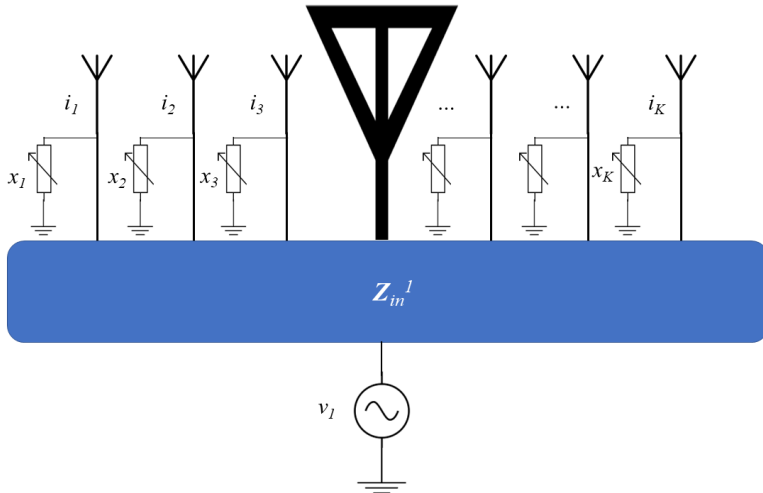


Figure 2-1 Geometry of the Single-Active / Multi-Passive antenna array.

From Figure 2-1, it can be seen that the input impedance depends upon the currents at the antenna elements. The generated currents can be expressed as:

$$\mathbf{i} = [\mathbf{Z}_M + \mathbf{Z}_L]^{-1} \mathbf{v}_M \quad (2.1)$$

equation (2.1) and the Figure 2-1 show that the current at each element is  $i$ , if total number of elements in the array are  $M$ , then  $\mathbf{i} = [i_1, i_2, i_3, \dots, i_M]^T$  is the current vector, the  $i_m$  is the scalar complex current at the  $m$ -th element in the MAMP array,  $[\ ]^T$

represents the vector transpose. Current at each element is dependent on the load values and the mutual coupling among the elements. The load matrix written as  $\mathbf{Z}_L = \text{diag}(x_1, x_2, \dots, x_M) \in \mathbf{C}^{M \times M}$ , where  $x_m$  is the tunable load of the  $m$ -th element of the array if the  $m$ -th element is passive, else it's source resistance ( $50\Omega$ ) if it is active.  $\mathbf{Z}_M \in \mathbf{C}^{M \times M}$  is the mutual coupling matrix which depends on the PAA's geometry;  $\mathbf{v}_M \in \mathbf{C}^{M \times 1}$  is the source voltage vector. The setup of Figure 2-1 shows that there is one RF chain, where the active element is connected to a source and the parasitic elements are grounded through loads (passive components). The distance between the elements is a multiple of wavelength  $\lambda$ , just placed in the close vicinity of active elements to enhance the mutual coupling among them. Equation 2.1 can be expressed for a SAMP as below:

$$\begin{bmatrix} Z_{11} + x_1 & Z_{12} & \cdots & Z_{1K} \\ Z_{21} & Z_{22} + x_2 & \cdots & Z_{2K} \\ \vdots & \vdots & \ddots & \vdots \\ \vdots & \vdots & \cdots & \vdots \\ Z_{K1} & Z_{K2} & \cdots & Z_{KK} + x_K \end{bmatrix} \begin{bmatrix} i_1 \\ i_2 \\ \vdots \\ i_K \end{bmatrix} = \begin{bmatrix} 0 \\ \vdots \\ v_1 \\ \vdots \\ 0 \end{bmatrix} \quad (2.2)$$

where  $K$  represents the total number of antenna elements in the SAMP as shown in Figure 2-1;  $Z_{KK}$  is the self-impedance of the  $K$ -th element of the array. The tunable load values are the variables that depend on the ratio of coupling matrix and the current at the respective active element. This ratio is a product of the currents at each element of the array and the current at the active element. It can be followed by [1]:

$$x_k = -\frac{1}{i_k}(\mathbf{z}_k \mathbf{i}_K), \quad k = 1, 2, \dots, K, \quad k \neq j \quad (2.3)$$

where  $\mathbf{z}_k$  is the  $k$ -th row of the  $Z$ -matrix of (2.2), and  $\mathbf{i}_K = [i_1, i_2, \dots, i_K]^T$ ;  $j$  is the position of the active element in the array geometry and  $i_j$  represents the current at the active element in the SAMP-PAA. The input impedance of the SAMP array at its active port is given by:

$$Z_{\text{in}}^j = \sum_{k=1}^K Z_{jk} \frac{i_k}{i_j} \quad (2.4)$$

where  $Z_{\text{in}}^j$  represents the input impedance at the  $j$ -th active port. To further enhance the performance of a SAMP parasitic antenna array, the number of active elements can also be increased thus increasing the number of parasitic elements associated with the respective active elements. If the number of active elements is increased, it means the array consists of multiple SAMPs placed close to each other. The proposed system will

result in a multi-active /multi-passive (MAMP) parasitic antenna array, as shown in Figure 2-2. The system consists of multiple RF chains being fed by a vector of voltages  $\mathbf{v}_M$ , which generates currents  $\mathbf{i}$  at each element of the array. Each active element is related to respective parasitic elements by the mutual coupling induced by the currents of the neighboring elements, thus producing a SAMP. Multiple SAMPs are placed at a distance of  $\lambda/2$ , resulting in a MAMP array as shown in Figure 2-2, which is based on the mutual coupling among the elements represented as  $\mathbf{Z}_{MM}$ . Parasitic elements are placed at a distance of  $d$  which is a function of  $\lambda$ , depending on the combination of loads that produce a radiation pattern close to the ideal or desired beam (which is a beam produced by an equivalent number of elements in a Uniform Linear Array (ULA)).

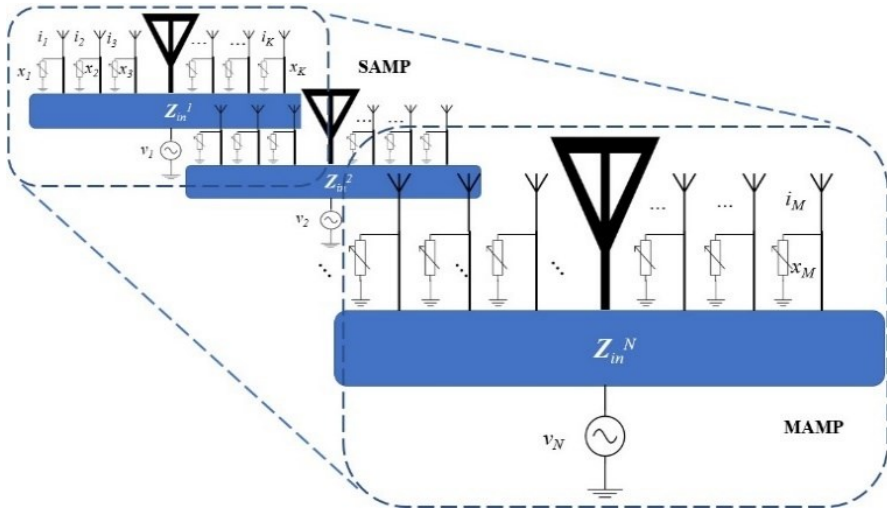


Figure 2-2 Multi-Active / Multi-Passive parasitic antenna array geometry.

When a huge number of SAMPs is placed together as shown in Figure 2-2, the equation (2.1) can be expanded for MAMPs, having  $N$  active elements means it has  $N$  number of SAMPs. The equation for MAMPs is given as:

$$\begin{bmatrix} Z_{11} + x_1 & Z_{12} & \cdots & Z_{1M} \\ Z_{21} & Z_{22} + R_1 & \cdots & Z_{2M} \\ Z_{31} & Z_{32} & \cdots & Z_{3M} \\ \vdots & \vdots & \ddots & \vdots \\ \vdots & \vdots & \ddots & \vdots \\ \vdots & \vdots & \cdots & \vdots \\ Z_{M1} & Z_{M2} & \cdots & Z_{MM} + x_M \end{bmatrix} \begin{bmatrix} i_1 \\ i_2 \\ i_3 \\ \vdots \\ \vdots \\ \vdots \\ i_M \end{bmatrix} = \begin{bmatrix} 0 \\ v_1 \\ 0 \\ \vdots \\ 0 \\ v_N \\ 0 \end{bmatrix} \quad (2.5)$$

where  $M$  is the total number of elements in a MAMP array. From equation (2.5), the variable  $x_M$  is the  $m$ -th load value of the respective parasitic element of the array. The performance of the multiport antenna array can be analyzed by using the input impedance of the ports. The input impedance connected to the RF chains incurring the effect of mutual coupling from neighboring elements can be obtained from (2.5):

$$Z_{\text{in}}^j = \sum_{m=1}^M Z_{jm} \frac{i_m}{i_j}, j \in \{1, 2, 3, \dots, N\} \quad (2.6)$$

where  $Z_{\text{in}}^j$  represents the input impedance at the  $j$ -th port active port of the MAMP array,  $Z_{jm}$  is the mutual coupling between the  $j$ -th active element and the  $m$ -th element in the MAMP array and  $i_j$  represents the current at the  $j$ -th active element in the MAMP array. It can be seen from equation (2.6) that the input impedance at a given feeding port has in principle an impact of coupling from its neighbor SAMPs as well.

### 2.3. PAAS RADIATION AND DESIGN CONDITIONS

In a general MAMP array case, where there is a strong mutual coupling among the elements due to the small distances among the elements, the radiation condition from port  $j$  of the array can be derived from equation (2.6) and is given below [12]:

$$-\text{Re} \left\{ \sum_{m=1, m \neq j}^M Z_{jm} \frac{i_m}{i_j} \right\} < \text{Re} \{Z_{jj}\} \quad (2.7)$$

The equation (2.7) expresses two possible scenarios, either the MAMP as a whole will radiate, or some of the ports will radiate. For the first case, (2.7) must hold for all  $j \in \{1, 2, 3, \dots, N\}$ , whereas for the latter case, it must hold for  $j$  belonging to any subset of  $\{1, 2, 3, \dots, N\}$ . For example, a case might occur where the MAMP array as a whole radiates and produces the desired beam shape, even though for certain feeding ports  $\text{Re} \{Z_{in}\} < 0$ . In MAMP arrays, if the distance between single active / multi-passive (SAMP) groups is large enough ( $\sim 0.5\lambda$ ), then the coupling between SAMP groups can be neglected, which results in the mutual coupling occurring among the SAMP's elements only. So, in that case the expression in (2.7) reduces to:

$$-\text{Re} \left\{ \sum_{k=(j-1)K+1, k \neq j}^{jK} Z_{jk} \frac{i_k}{i_j} \right\} < \text{Re} \{Z_{jj}\} \quad (2.8)$$

which means that the PAA must be designed in such a way that the value of the input impedance is greater than zero as a whole, or the real value of the self-impedance of each active element is large enough so that it remains a positive number when the mutual coupling effect is added into it [12].

## 2.4. MAMP DESIGN

An example is shown by considering a PAA with 4 active and 16 parasitic elements, named MAMP-I and MAMP-II. The array elements are emulated as half-wave dipoles operating at a frequency of 2.4 GHz. The distance between the active elements is  $0.5\lambda$ , whereas parasitic elements are placed at  $0.2\lambda$  from each other. An alternating optimization stochastic beamforming (AO-SBA) algorithm [14] is used to compute the loads. Radiation patterns are obtained based on a precoding scheme which is beamforming. A MAMP array with 4 active and 16 parasitic elements is presented in Figure 2-3, based on point sources. An emulated structure of a proposed MAMP array can be seen in Figure 2-4 from CST microwave studio; this tool is used for the computational analysis of the proposed MAMP array. The distance between the neighboring active elements is  $0.5\lambda$  and between the neighboring parasitic elements is  $0.2\lambda$ . The dipoles cannot be modeled as ideal in CST so finite length halfwave dipoles are considered and simulated at the frequency of 2.4 GHz. The material used for the dipoles is a perfect conductor and the diameter of each dipole is  $\lambda/500$ .

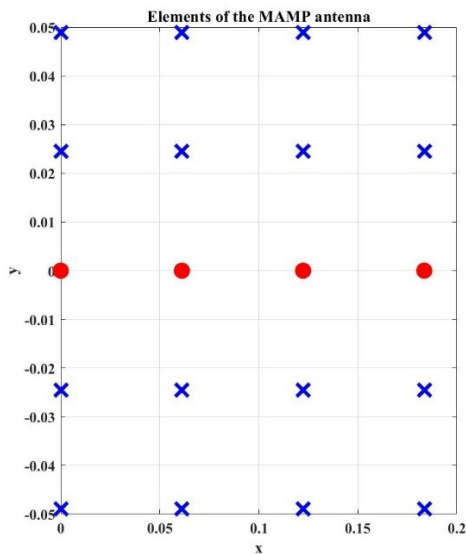


Figure 2-3 The geometry of a multi-active / multi-passive antenna array with four (red-colored) active elements and sixteen (blue-colored) parasitic elements. The distance between SAMPSS (active elements) is  $\lambda/2$  and the distance between the parasitic elements is  $0.2*\lambda$ .

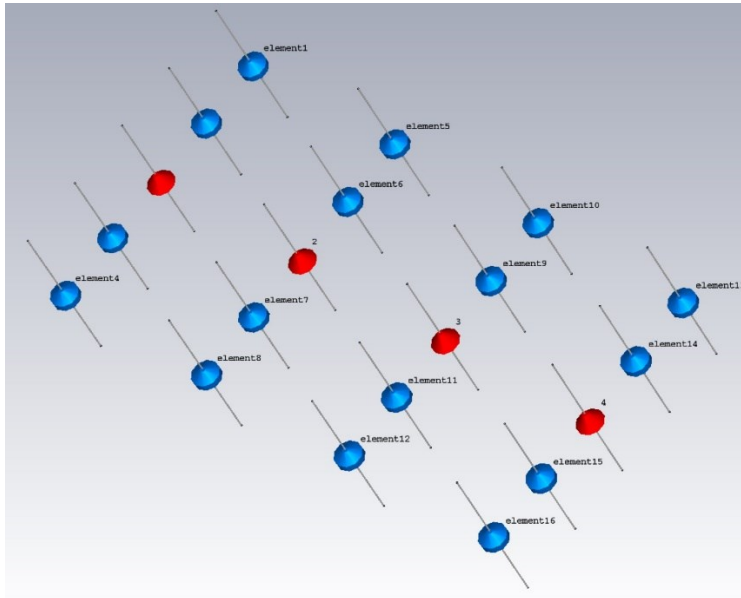


Figure 2-4 MAMP antenna array designed in CST microwave studio. Red-colored dots are active ports for feeding the array, and blue dots are parasitic elements with respective capacitive or inductive values.

## 2.5. RESULTS AND DISCUSSION

Two different sets of loads have been obtained using SBA to show the application of radiation conditions. The comparison of results is shown in the form of radiation patterns, normalized gain and the error between the desired and the ideal gain of a ULA. Two MAMPs are considered with same parameters such as frequency and distance among the elements. MAMP-I produces results without the application of radiation conditions, whereas MAMP-II is based on the proposed radiation conditions but with same parameters to that of MAMP-I. The input impedance at the 2<sup>nd</sup> port of MAMP-I is negative as shown in Table 2-1, which means either the respective port was not radiating, or the power was dissipating. The input impedance at all the feeding ports of MAMP-II is positive resulting in radiation at all the ports of the array.

Table 2-1 Input impedance at all the active ports of the MAMP antenna array.

Geometry	$Z_{in}^1$	$Z_{in}^2$	$Z_{in}^3$	$Z_{in}^4$
<b>MAMP-I</b>	15.0096 +59.0513i	-2.1484 +59.1588i	4.4715 +66.0439i	8.3983 +56.5592i
<b>MAMP-II</b>	42.1995 +84.7396i	1.8763 +47.5545i	4.3926 +67.3247i	13.2302 +65.4366i

Despite the negative input impedance at one of the ports of the MAMP-I, it shows significantly good radiation pattern and the beam which is directed towards  $\varphi=90^\circ$ .

### 2.5.1. MAMP-I

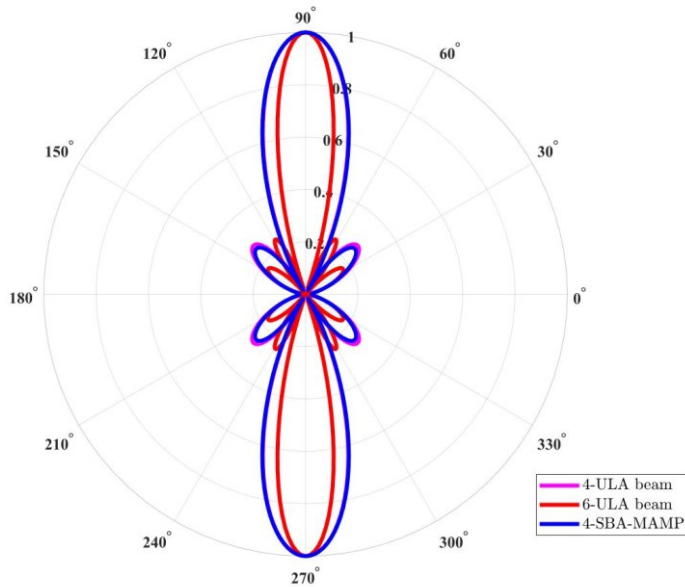


Figure 2-5 Representation of the radiation patterns: the red color represents the radiation pattern of a six-element uniform linear array, and the magenta represents a four-element ULA, whereas blue color is representing radiation pattern of a MAMP.

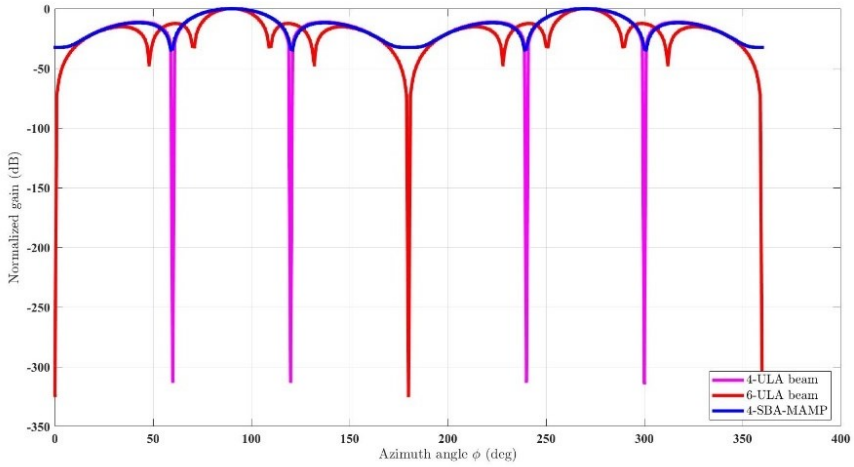


Figure 2-6 Comparison of the normalized gains with that of achieved by 6-element ULA, 4-element ULA and a MAMP with 4 active and 16 parasitic elements.

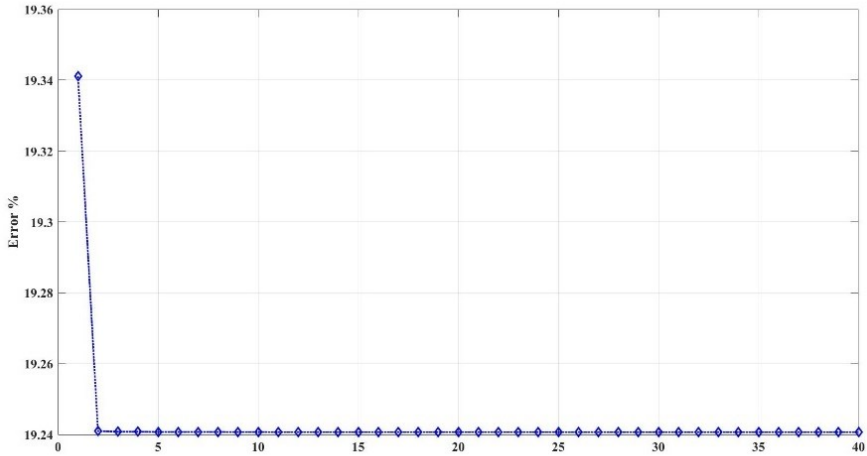


Figure 2-7 Error is calculated during each iteration when both the radiation patterns, the proposed MAMP and ULA are compared.

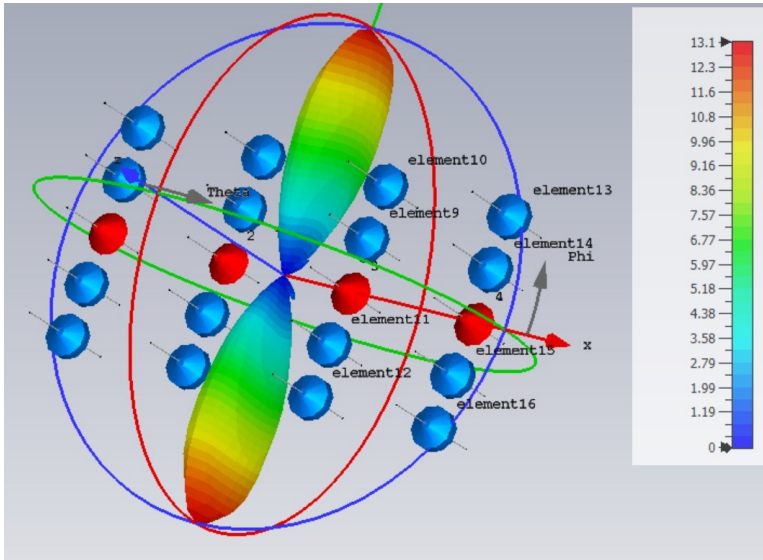


Figure 2-8 3D radiation pattern of the MAMP-I, where port 2 is having a negative input impedance.

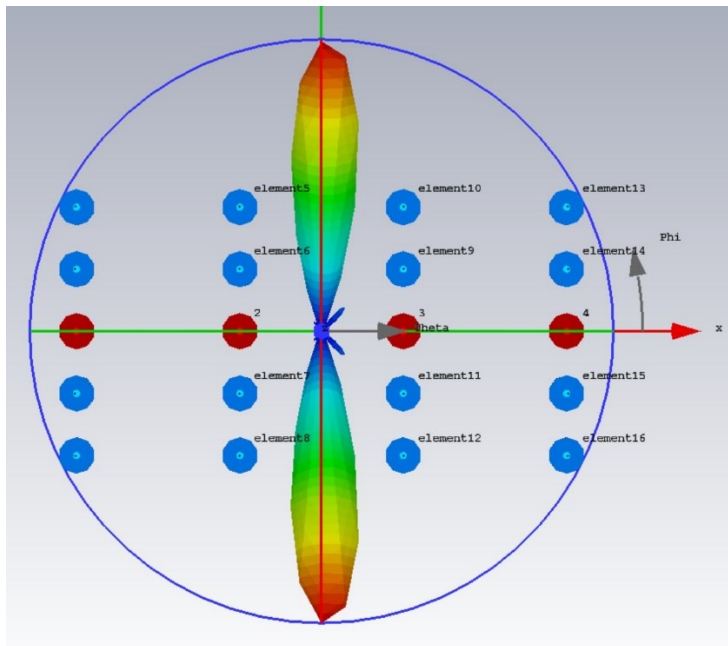


Figure 2-9 Top view of the 3D radiation pattern of the MAMP-I.

As an example, MAMP-I is designed where it has 4 active and 16 parasitic elements also shown in Figures 2-3 and 2-4. The SBA is utilized to produce the loads for parasitic elements without applying any radiation conditions. The radiation pattern is in good shape and can be seen in Figure 2-5. The blue-colored curve represents the MAMP-I, and the red represents the conventional ULA with six elements. Clearly, it can be seen that by using MAMPs, the RF chains can be reduced, and a similar beam can be produced by reducing RF assembly. A comparison of normalized gain can be seen in Figure 2-6, where the nulls are almost in similar angles. Although the error is 19.24% as shown in Figure 2-7, the results are still promising. The error is actually calculated after comparing the radiation patterns of desired beam pattern of MAMP to that of a ULA. To verify the results of MAMP-I, simulations were carried out in CST microwave studio. Figure 2-4 shows the geometry of the MAMP-I emulated in the CST. The load values for the parasitic elements were generated using SBA. Then these loads were fed to CST simulation, and it produced similar results. Figures 2-8 and 2-9 show the 3D radiation pattern of MAMP-I with good directivity of 13.1. We know that the MAMP-I has a negative impedance at its port-2; despite that, it produces an overall good radiation beam both using SBA and the CST simulation, but, in reality, there is power dissipation or absorption at the 2<sup>nd</sup> port because of the mismatch.

## 2.5.2. MAMP-II

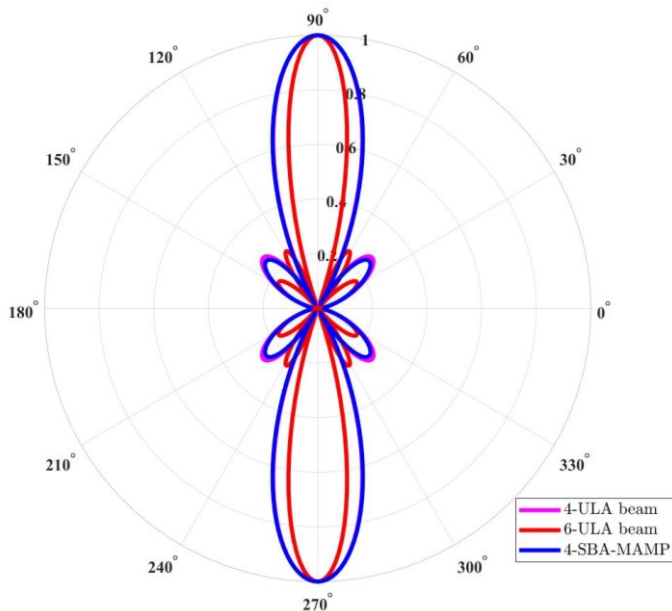


Figure 2-10 Representation of the radiation patterns: the red color represents the radiation pattern of a 6-element uniform linear array, and the magenta represents a 4-element ULA, whereas blue color is representing radiation pattern of a MAMP.

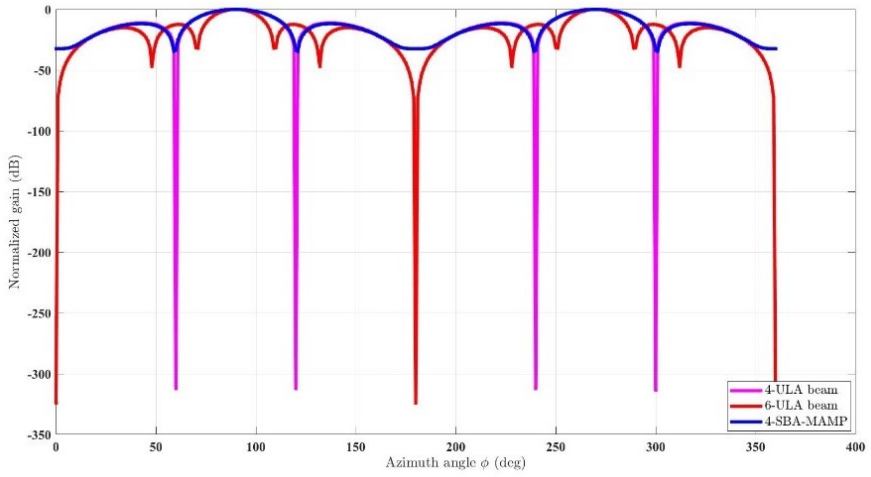


Figure 2-11 Comparison of the normalized gains with that of achieved by 6-element ULA, 4-element ULA and a MAMP with 4 active and 16 parasitic elements.

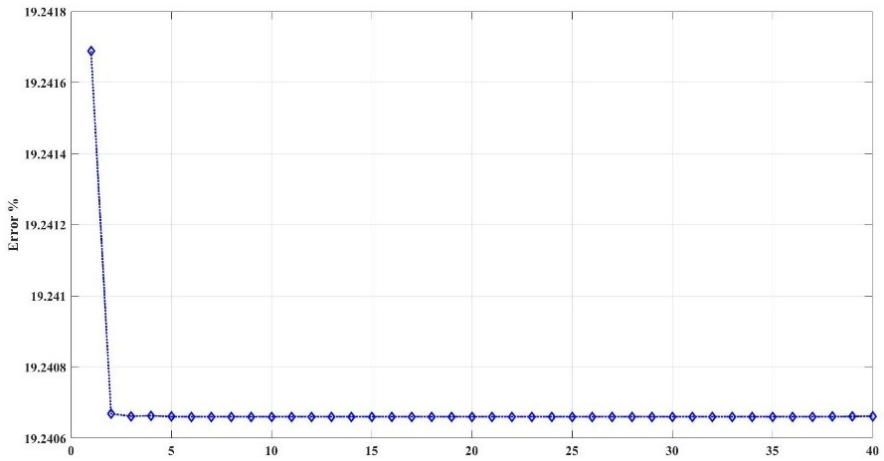


Figure 2-12 Error is calculated during each iteration when both the radiation patterns, the proposed MAMP and ULA are compared.

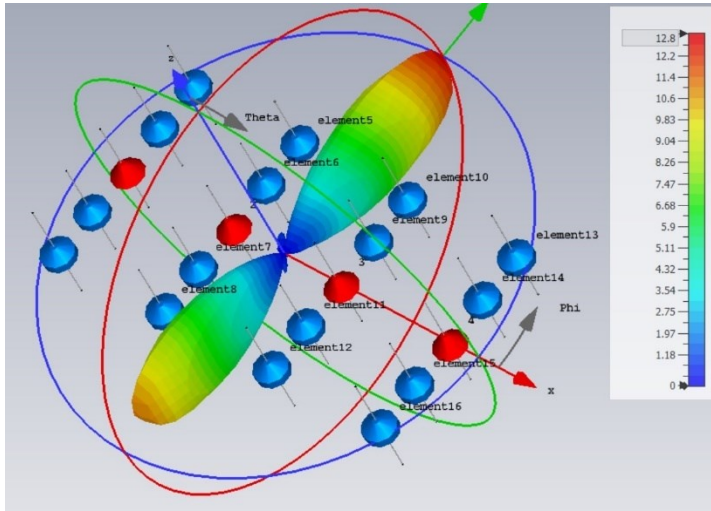


Figure 2-13 3D radiation pattern of the MAMP-II, where all the feeding ports have an input impedance which is greater than  $\zeta_0$ .

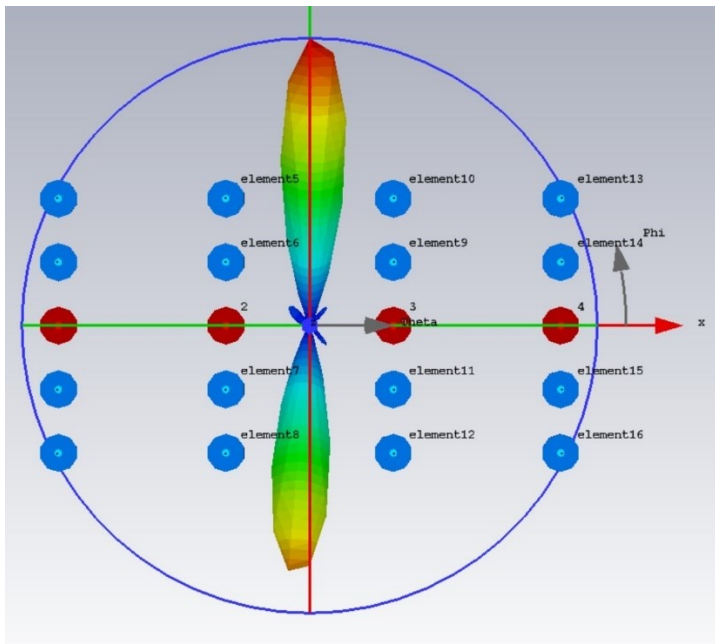


Figure 2-14 Top view of the 3D radiation pattern of the MAMP-II.

To prove the point, as another example, MAMP-II is considered with same number of active and parasitic elements as we have in MAMP-I. All the parameters are same such as: frequency, distance among the elements, and SBA variables. In MAMP-II, radiation conditions are introduced to get the positive input impedances. The values of the input impedances are given in Table 2-1. Again, all the loads are obtained using SBA and then embedded in CST simulations. Figures 2-5 and 2-10 show that there is no visible difference between the radiation patterns. The normalized gains are also in similar fashion. The error is 0.001% less than the error in MAMP-I, which is not significantly a higher difference. Figures 2-9 and 2-14 show the 3D radiation patterns of MAMP-I and MAMP-II, where it can be seen that the results of both MAMP-I and MAMP-II are comparable. So, it is mandatory for the given constraints to be met in order for the structure to radiate and be an excellent candidate for MIMO communications.

## **2.6. CONCLUSION**

By employing different examples, we have presented that practically the same beams may be produced by a PAA-MAMP, even though the radiation constraints for each case may differ significantly. Radiation conditions (2.7) and (2.8) are developed to be incorporated for computing the load values to make sure that the array radiates. The need for the constraints is shown and proved by using different examples of the MAMP array. Two examples show that even though the radiation patterns are similar, there still might be a possibility that the array is not radiating enough with good efficiency because of the power dissipation at some of its ports. The radiation patterns are obtained using CST microwave studio and are compared. The outcomes of this chapter are applied in subsequent chapters to further enhance the MAMP performance.

## 2.7. REFERENCES

- [1] A. Kalis, A. G. Kanatas, C. B. Papadidas, *Parasitic Antenna Arrays for Wireless MIMO Systems*, Springer 2014.
- [2] Constantine A. Balanis, *Antenna Theory: Analysis and Design*, Hoboken, NJ, USA: Wiley, 2012.
- [3] D. M. Pozar, *Microwave Engineering*, Hoboken, NJ, USA: Wiley, 2012.
- [4] A. Kalis, A. Kanatas, and C. B. Papadidas, "A novel approach to MIMO transmission using a single RF front end," *IEEE J. Sel. Areas Commun.*, vol. 26, no. 6, pp. 972–980, Aug. 2008.
- [5] O. Alrabadi, C. B. Papadidas, A. Kalis, and R. Prasad, "A universal encoding scheme for MIMO transmission using a single active element for PSK modulation schemes," *IEEE Trans. Wireless Commun.*, vol. 8, no. 10, pp. 5133–5142, Oct. 2009.
- [6] V. Barousis, A. Kanatas, and A. Kalis, "Beam-space-domain analysis of single-RF front-end MIMO systems," *IEEE Trans. Veh. Technol.*, vol. 60, no. 3, pp. 1195–1199, Mar. 2011.
- [7] O. Alrabadi, J. Perruisseau-Carrier, and A. Kalis, "MIMO transmission using a single RF source: Theory and antenna design," *IEEE Transactions on Antennas Propagation*, vol. 60, no. 2, pp. 654–664, Feb. 2012.
- [8] V. Barousis and C. B. Papadidas, "Arbitrary precoding with single-fed parasitic arrays: Closed-form expressions and design guidelines," *IEEE Wireless Commun. Lett.*, vol. 3, no. 2, pp. 229–232, Apr. 2014.
- [9] V. Barousis, C. B. Papadidas, and R. Muller, "A new signal model for MIMO communication with compact parasitic arrays," in Proc. 6th ISCCSP, pp. 109–113, 2014.
- [10] L. Zhou, F. A. Khan, T. Ratnarajah, and C. B. Papadidas, "Achieving arbitrary signals transmission using a single radio frequency chain", *IEEE Transactions on Communications*, vol. 63, no. 12, pp. 4865–4878, December 2015.
- [11] A. Li, C. Masouros, and C. B. Papadidas, "MIMO transmission for single-fed ESPAR with quantized loads," *IEEE Transactions on Communications*, vol. 65, no. 7, pp. 2863–2876, 2017.
- [12] M. H. Tariq, D. K. Ntaikos and C. B. Papadidas, "Design Guidelines for Multi-Active/Multi-Passive Parasitic Antenna Arrays," in *IEEE Antennas and Wireless Propagation Letters*, vol. 19, no. 12, pp. 2141–2144, Dec. 2020, doi: 10.1109/LAWP.2020.3024803.
- [13] Y. Zhou, R. Adve, and S. Hum, "Design and evaluation of pattern reconfigurable antennas for MIMO applications," *IEEE Trans. On Antennas and Propagation*, vol. 62, no. 3, pp. 1084–1092, Mar. 2014.
- [14] G. K. Papageorgiou, D. Ntaikos, and C. B. Papadidas, "Efficient beamforming with Multi-Active Multi-Passive antenna arrays," *IEEE 19th SPAWC*, Kalamata Greece, June 25–28, 2018.

# CHAPTER 3. HYBRID BEAMFORMING USING MULTI-ACTIVE/MULTI- PASSIVE PARASITIC ANTENNA ARRAYS

Multi-Active / Multi-Passive (MAMP) Parasitic Antenna Arrays (PAA) have shown significant potential in recent wireless communications due to their reduced cost, weight, and complexity. The MAMP typically consists of a few active feeding ports and multiple parasitic elements coupled with neighboring elements thus resulting in a combined beam similar to that of a conventional Multiple-Input Multiple-Output (MIMO) antenna array. In this study, the MAMP antenna array is designed such that it guarantees that the array radiates based on a set of radiation conditions. Passive load values are calculated using a stochastic beamforming algorithm (SBA), and it is ensured that the MAMP array satisfies the radiation conditions. The radiation efficiency of the MAMP array is calculated, for the first time to the best of our knowledge, through closed-form expressions. This allows us to incorporate the radiation efficiency as a performance target, in the computation of the array's loads and weights. We do so, indicatively, on a previously proposed algorithm (SBA) and show a good match between the calculated and simulated results via the CST simulation tool.

## 3.1. INTRODUCTION

Multiple-Input Multiple-Output transmission has attracted a plethora of researchers and scientists in recent years due to its benefits for spatial multiplexing and large antenna and diversity gain. These benefits increase as the number of antennas increases; however, this comes at the expense of size, cost, and complexity of the required radiofrequency (RF) chains. The size and the cost of multiple antenna systems have been reduced by utilizing a single RF chain in the past few years when the idea was first introduced by Harrington [1]. The research community has since significantly contributed to the concept of Electronically Steerable Parasitic Array Radiators (ESPAR). If parasitic elements are placed at a very close distance from the active element, then the induced currents may affect the beam pattern generated by the array [2–3].

Many different techniques and approaches have been proposed in the past to achieve beamforming using ESPARs, such as the Hamiltonian method [4], an algorithm based on sequential perturbation [5], a cross-correlation coefficient maximization technique [6], and simultaneous perturbation stochastic approximation (SPSA) [7]. A technique for spatial multiplexing of QPSK symbols has been introduced by Bains and Kalis which is known as the beam space model [8–11]. Some applications have also been proposed

using ESPAR, for example, the Reactance Domain Multiple Signal Classification (RD-MUSIC) algorithm [12], a system for the implementation of direction of arrival (DOA) estimation based on a rotational invariant technique (ESPRIT) [13]. In the early approaches of ESPARs, it was ensured that the array radiates based on the estimation of loads while neglecting the radiation conditions being incorporated in the algorithms.

Design guidelines and radiation constraints were introduced for the first time in [14] to ensure that the array will radiate. Later, significant work has been done on the single fed RF transmission based on those radiation conditions such as a new signal model with an arbitrary precoding scheme proposed in [15], quantized load selection [16], and transmission with peak power constraint [17]. The research activity has mostly focused on ESPAR arrays where an active element (AE) is fed through a single RF chain, including currents on its neighboring parasitic elements (PE), also denoted as a single-active / multi-passive (SAMP) system. The current on the elements is altered through different values of the loads grounded via PEs [18]. Enhanced performance of the multi antenna transmission is ensured by increasing the number of active elements, thus creating multi-active / multi-passive parasitic antenna arrays.

A stochastic beamforming algorithm is presented to emulate the radiation pattern of the ideal Uniform Linear Array (ULA) with that of the MAMP array by reducing the error [18, 26]. A significant match is shown between the radiation patterns of the MAMP and ULA in both 2D and 3D with a 50% reduction of RF chains, but there is no constraint that ensures the radiation at all ports of the array. It means that there might be a possibility where the arrays might have similar radiation patterns but some of the ports are not radiating, and power is absorbed instead. In this case, the radiation efficiency of the array is low or below a certain desired level. We derived new conditions in the closed form [19], where it is observed that for multi-active arrays, there might be a state when some of the active ports are matched and radiating, and some are not radiating where there is also a possibility that the array as a whole is not radiating because of the effect of mutual coupling and combination of load values.

All these observations make it difficult to analyze the antenna array performance because of the mutual coupling and the total radiation by the array. So, to analyze the multi-port antenna array, the Total Active Reflection Coefficient (TARC) is considered a reliable parameter [21]. TARC takes into account the mutual coupling in the form of S-parameters with arbitrary inputs. The TARC is important for MIMO systems because it takes the interport antenna coupling, port matching, and the effect due to the different phases at each input port of the antenna. TARC is also used to find the efficiency of the array [22].

Several improvements are required in the presented previous works, including an extension of the array from a single active element to multiple active elements, ensuring the radiation conditions for the arrays in some of the works and in some cases mostly the load values are active load values which are difficult to simulate and, in some cases,

even harder to implement. In this work, we propose a solution for all these potential issues by applying it to the stochastic beamforming algorithm provided in [20] for MAMPs. As the previous algorithms and techniques do not suffice the capability of a MAMP array, we used radiation efficiency as a parameter in the cost function to find the optimized loads and weights. This is an extension of the SBA in order to find the passive imaginary load values which ensure that the array as a whole radiates and calculated the radiation efficiency of the MAMP parasitic antenna array. The results are verified by using the CST simulation tool while MATLAB was used for numerical analysis.

### 3.2. SYSTEM MODEL

The system consists of multiple RF chains being fed by a vector of voltages  $\mathbf{v}_M$ , which generates currents  $\mathbf{i}$  at each element of the array. Each active element is related to respective parasitic elements by the mutual coupling induced by the currents of the neighboring elements, thus producing a SAMP. Multiple SAMPs are placed at a distance of  $\lambda/2$ , resulting in a MAMP array as shown in Figure 3-1, which is based on the mutual coupling among the elements represented as  $\mathbf{Z}_{MM}$ . Parasitic elements are placed at a distance of  $d$  which is a function of  $\lambda$ , depending on the combination of loads that produce a radiation pattern close to the ideal or desired beam, which is a beam produced by an equivalent number of elements in a ULA.

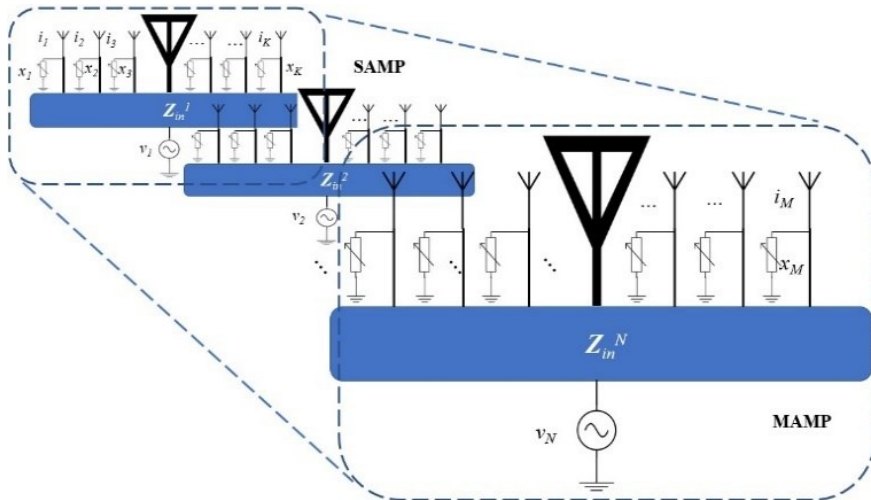


Figure 3-1 Multi-Active / Multi-Passive parasitic antenna array geometry.

The elements are placed in close vicinity to the active elements to get a strong mutual coupling through strong induced currents. The generated currents are given as:

$$\mathbf{i} = [\mathbf{Z}_{MM} + \mathbf{Z}_L]^{-1} \mathbf{v}_M \quad (3.1)$$

where  $\mathbf{i}$  is the vector representing currents at all elements of the MAMP array.  $\mathbf{Z}_L$  is a matrix representing the source resistance at all the active elements and the load values of parasitic elements. Equation (3.1) can be expanded for the MAMPs as given in [19]:

$$\begin{bmatrix} Z_{11} + x_1 & Z_{12} & \cdots & Z_{1M} \\ Z_{21} & Z_{22} + R_1 & \cdots & Z_{2M} \\ Z_{31} & Z_{32} & \cdots & Z_{3M} \\ \vdots & \vdots & \ddots & \vdots \\ \vdots & \vdots & \ddots & \vdots \\ \vdots & \vdots & \cdots & \vdots \\ Z_{M1} & Z_{M2} & \cdots & Z_{MM} + x_M \end{bmatrix} \begin{bmatrix} i_1 \\ i_2 \\ i_3 \\ \vdots \\ \vdots \\ \vdots \\ i_M \end{bmatrix} = \begin{bmatrix} 0 \\ v_1 \\ 0 \\ \vdots \\ 0 \\ v_N \\ 0 \end{bmatrix} \quad (3.2)$$

From equation (3.2), the variable  $x_m$  is the  $m$ -th load value of the respective parasitic element of the array, where  $i_m$  is the current at the  $m$ -th element and  $v_j$  is the voltage at the  $j$ -th active element in the MAMP array, and  $j \in \{1, 2, 3, \dots, N\}$ . The performance of the multiport antenna array can be analyzed by using the input impedance of the ports. The input impedance connected to the RF chains incurring the effect of mutual coupling from neighboring elements can be obtained from (3.2):

$$Z_{\text{in}}^j = \sum_{m=1}^M Z_{jm} \frac{i_m}{i_j}, j \in \{1, 2, 3, \dots, N\} \quad (3.3)$$

where  $Z_{\text{in}}^j$  represents the input impedance at the  $j$ -th port,  $Z_{jm}$  is the mutual coupling between the  $j$ -th active element and the  $m$ -th element in the MAMP array and  $i_j$  represents the current at the  $j$ -th active element in the MAMP array.

### 3.3. RADIATION CONDITIONS

The expression in (3.3) has been used as a constraint in [19] to ensure the radiation of the MAMP array. The mutual coupling among the elements can drive the real part of the input impedance to a negative value i.e.,  $Z_{\text{in}}^j < 0$ , which means that the power is not

radiated by the array and is dissipated instead. The radiation condition for a MAMP array is given by [19]:

$$-\text{Re} \left\{ \sum_{m=1, m \neq j}^M Z_{jm} \frac{i_m}{i_j} \right\} < \text{Re} \{Z_{jj}\} \quad (3.4)$$

So, for the array to radiate, the input impedance at all the feeding ports must be greater than zero or it must be a positive number that remains greater than the self-impedance  $Z_{jj}$  of the respective active element. The developed algorithm makes sure that the input impedance at all the feeding ports is greater than zero, which ensures that the array radiates as a whole.

These radiation conditions do not suffice the desired array performance because previously derived constraints guarantee array radiation when either of the active port is radiating or all the elements are radiating based on the comparison of radiation patterns regardless of the overall array efficiency. Radiation efficiency is one of the most significant parameters of a multi-port antenna array that shows an overall reliable array performance. From [21], we know that the radiation efficiency of the antenna array is:

$$\eta = \frac{P_{rad}}{P_{in}} \quad (3.5)$$

$$\Gamma_T = \sqrt{1 - \frac{P_{rad}}{P_{in}}} \quad (3.6)$$

where the total active reflection coefficient ( $\Gamma_T$ ) is given by  $\Gamma_T$  which in turn can be written in terms of radiation efficiency. The TARC is considered the most valuable parameter to analyze the performance of a multiport array because it considers the mutual coupling among the elements, and it takes into account the weights of the voltages which are in the form of different amplitudes and phases. If antenna elements are ideal and lossless, from (3.5) and (3.6), we can get,

$$\eta = 1 - \Gamma_T^2 \quad (3.7)$$

where  $\Gamma_T$  for two active ports can be defined as:

$$\Gamma_T = \sqrt{\frac{|V_1 S_{11} + V_2 S_{12}|^2 + |V_1 S_{21} + V_2 S_{22}|^2}{|V_1|^2 + |V_2|^2}} \quad (3.8)$$

From (3.8), the efficiency is expressed in terms of S-parameters, whereas SBA needs Z-parameters to justify (3.2). S-parameters can be converted to Z-parameters using some conversion expression, these formulae are given for a two-port network by Pozar in [3].

$$S_{11} = \frac{(Z_{11} - Z_0)(Z_{22} + Z_0) - Z_{12}Z_{21}}{(Z_{11} + Z_{22})(Z_{22} + Z_0) - Z_{12}Z_{21}} \quad (3.9)$$

$$S_{12} = \frac{2Z_{12}Z_0}{(Z_{11} + Z_{22})(Z_{22} + Z_0) - Z_{12}Z_{21}} \quad (3.10)$$

$$S_{21} = \frac{2Z_{21}Z_0}{(Z_{11} + Z_{22})(Z_{22} + Z_0) - Z_{12}Z_{21}} \quad (3.11)$$

$$S_{22} = \frac{(Z_{11} + Z_0)(Z_{22} - Z_0) - Z_{12}Z_{21}}{(Z_{11} + Z_{22})(Z_{22} + Z_0) - Z_{12}Z_{21}} \quad (3.12)$$

The generalized form of the above conversions for multiple antenna elements is obtained using (3.2).

$$S_{ii} = \frac{((Z_{NN} + x_k) - Z_0)(Z_{MM} + Z_0) - Z_{NM}Z_{MN}}{((Z_{NN} + x_k) + Z_0)(Z_{22} + Z_0) - Z_{NM}Z_{MN}} \quad (3.13)$$

$$S_{ij} = \frac{2Z_{NM}Z_0}{((Z_{NN} + x_k) + Z_0)(Z_{MM} + Z_0) - Z_{NM}Z_{MN}} \quad (3.14)$$

$$S_{ji} = \frac{2Z_{MN}Z_0}{((Z_{NN} + x_k) + Z_0)(Z_{22} + Z_0) - Z_{NM}Z_{MN}} \quad (3.15)$$

$$S_{jj} = \frac{((Z_{NN} + x_k) + Z_0)(Z_{MM} - Z_0) - Z_{NM}Z_{MN}}{((Z_{NN} + x_k) + Z_0)(Z_{22} + Z_0) - Z_{NM}Z_{MN}} \quad (3.16)$$

The extended form of expressions is given in (3.13) to (3.16) to compute S-parameters among the elements of the MAMP array, where  $i \in \{1,2,3, \dots, N\}$ ,  $j \in \{1,2,3, \dots, M\}$  and  $i \neq j$ .  $x_k$  is the  $k$ -th load value of the respective parasitic element. So, from (3.8), if there is no coupling among the elements, and the array is ideal, then the radiation efficiency of the array will be one, but in the case of the MAMP array, there will be coupling among the neighboring elements so it will be a number between zero and one. The constraint comes up as if the  $\eta$  of the array is one if the total active reflection coefficient is zero.

So, the new constraint is  $0 < \eta < 1$

If  $\Gamma_T = \mathbf{0}$ , then  $\eta = 1$

Any desired  $\eta$  for a MAMP array with  $N$  number of elements, the efficiency of the MAMP array is given by:

$$\eta = 1 - \sqrt{\frac{\sum_{i=1}^N \left( \left| \sum_{j=1}^N v_j S_{ij} \right|^2 \right)}{\sum_{i=1}^N |v_i|^2}} \quad (3.17)$$

### 3.4. ALTERNATING OPTIMIZATION STOCHASTIC BEAMFORMING ALGORITHM

The alternating optimization approach is extended for the stochastic beamforming algorithm in [18] by introducing the new radiation conditions which guarantee that the array is radiating as a whole or some of the elements are radiating depending upon how strictly we wish to apply the constraints.

The cost function that we attempt to optimize can be viewed as a function of both the loads and the voltage vector. Thus, for a selected antenna array structure that determines the set S of AEs and the impedance matrix Z, the targeted cost function that we attempt to minimize is given by:

$$L(\mathbf{x}_{Sc}, \mathbf{w}) := \omega \left[ 1 - \left( \frac{|b^H \mathbf{a}(\mathbf{x}_{Sc}, \mathbf{w})|}{\|b\|_2 \|\mathbf{a}(\mathbf{x}_{Sc}, \mathbf{w})\|_2} \right) \right] + \mu [1 - (\eta(\mathbf{x}_{Sc}, \mathbf{w}))], \quad (3.18)$$

Where  $\omega + \mu = 1$ ,

$\omega$  is the weight for the radiation pattern and  $\mu$  is the weight for the radiation efficiency,

$$\mathbf{w} = \begin{bmatrix} \text{real}(\mathbf{v}_S) \\ \text{imag}(\mathbf{v}_S) \end{bmatrix}, \text{ and}$$

$$\mathbf{a}(\mathbf{x}_{Sc}, \mathbf{w}) = \mathbf{S}^T (\mathbf{Z} + \text{diag}(\mathbf{I}_S \mathbf{x}_S + j \mathbf{I}_{Sc} \mathbf{x}_{Sc}))^{-1} \mathbf{v}(\mathbf{w}), \quad (3.19)$$

$$\mathbf{v}(\mathbf{w}) = \mathbf{I}_S (\mathbf{w}_{1:N_a} + j \mathbf{w}_{(N_a+1):2N_a}),$$

$$\mathbf{S} = [S(\phi_1), \dots, S(\phi_N)]$$

The optimization in (3.18) is non-linear with respect to both variables  $\mathbf{x}_{Sc}$  and  $\mathbf{w}$ .  $\mathbf{S}$  is the steering matrix of the MAMP antenna and  $\mathbf{b}$  is the radiation pattern of the desired beam pattern. We attempt to solve the optimization task with an alternating optimization stochastic approach. Our proposed scheme is summarized in Algorithm 1.

---

**Algorithm 1** Alternating Optimization Stochastic Beamforming Algorithm

---

- 1: **function** AO-SBA ( $\mathbf{b}$ ,  $(\beta_m)_{m=1}^M$ ,  $S$ ,  $\mathbf{Z}$ ,  $\mathbf{S}$ ,  $\tau$ ,  $N_m$ ,  $T_{er}$ ,  $\epsilon_{ps}$ ,  $\omega$ ,  $\mu$ )
- 2:  $m \leftarrow 0$ ,  $\mathbf{x}_{Sc} = [0, \dots, 0]^T$ ,  $\mathbf{w} \leftarrow [\mathbf{1}^T, \mathbf{0}^T]^T$
- 3: **while**  $m < M$  **do**
- 4:  $m \leftarrow m + 1$ ,  $n \leftarrow 0$ ,  $k \leftarrow 0$
- 5:  $err_x \leftarrow \frac{1}{\epsilon_{ps}}$ ,  $err_w \leftarrow \frac{1}{\epsilon_{ps}}$
- 6: **while**  $n < N_m$  **and**  $err_x \geq T_{er}$  **do**
- 7:      $n \leftarrow n + 1$ ,  $\mathbf{x}_{old} \leftarrow \mathbf{x}_{Sc}$
- 8:     Create:  $\boldsymbol{\delta}_x \sim B\left(1, \frac{1}{2}\right)$  with values  $\pm 1$
- 9:      $\mathbf{x}_{Sc}^+ = \mathbf{x}_{Sc} + \beta_m \boldsymbol{\delta}_x$ ,  $\mathbf{x}_{Sc}^- = \mathbf{x}_{Sc} - \beta_m \boldsymbol{\delta}_x$
- 10:      $L_x^+ = L(\mathbf{x}_{Sc}^+, \mathbf{w})$ ,  $L_x^- = L(\mathbf{x}_{Sc}^-, \mathbf{w})$

- 11:  $\xi_x = \frac{1}{2\beta_m} (L_x^+ - L_x^-) \frac{1}{\delta_x}$
- 12:  $\mathbf{x}_{Sc} = \mathbf{x}_{Sc} - \tau \xi_x, err_x = \frac{\|\mathbf{x}_{Sc} - \mathbf{x}_{old}\|_2}{\|\mathbf{x}_{old}\|_2 + eps}$
- 13: **end while**
- 14: **while**  $k < N_m$  **and**  $err_v \geq T_{er}$  **do**
- 15:  $k \leftarrow k + 1, \mathbf{w}_{old} \leftarrow \mathbf{w}$
- 16: Create:  $\delta_w \sim B\left(1, \frac{1}{2}\right)$  with values  $\pm 1$
- 17:  $\mathbf{w}^+ = \mathbf{w} + \beta_m \delta_w, \mathbf{w}^- = \mathbf{w} - \beta_m \delta_w$
- 18:  $L_v^+ = L(\mathbf{x}_{Sc}, \mathbf{w}^+), L_x^- = L(\mathbf{x}_{Sc}, \mathbf{w}^-)$
- 19:  $\xi_w = \frac{1}{2\beta_m} \frac{(L_v^+ - L_v^-) \mathbf{1}}{\delta_w}$
- 20:  $\mathbf{w} = \mathbf{w} - \tau \xi_w, err_w = \frac{\|\mathbf{w} - \mathbf{w}_{old}\|_2}{\|\mathbf{w}_{old}\|_2 + eps}$
- 21: **end while**
- 22: **while**  $real(\mathbf{Z}_{in}^j) > 0$ , **do** Given by (3.3) and (3.4)
- 23:  $p \leftarrow p + 1, j \in \{1, 2, 3, \dots, N\}$
- 24: Go to **function** AO-SBA
- 25: **while**  $0 < \eta < 1$
- 26:  $p \leftarrow p + 1$
- 27:  $\omega + \mu = 1,$
- 28:  $\eta = 1 - \Gamma_T^2, \Gamma_T = \sqrt{1 - \frac{P_{rad}}{P_{in}}}$
- 29: **end while**
- 30: **end while**

31:  $Er(m) \leftarrow L(\mathbf{x}_{sc}, \mathbf{w})$

Given by (3.18) and (3.19)

32: **end while**

33: **end function**

**Ensure:**  $Er_{1:M}, \mathbf{x}_{sc}, \mathbf{w}, \eta$

---

The algorithm is following the iterative approach to find the optimized loads and the weights with reduced error whereas the degree of the cost function smoothing is achieved by using the smoothing sequence  $(\beta_m)_{m=1}^M$ . The process repeats M times for different smoothing steps until the local minimum probability is reduced. A random vector  $\delta$  is created using the binomial distribution, then the cost function samples are computed. It leads to the approximation of the gradient until its convergence. This estimates the approximation and returns the estimated solution; otherwise, the iteration counter is increased by one.

The global minimization corresponds to a radiation pattern identical to the desired pattern, but the convergence time will be expanded since in this case the smoothing sequence should be larger, increasing the number of required cycles until the termination of the overall process [20]. The estimated solution provides the computed loads which gives the corresponding input impedance at each port. So, the finds the load values that satisfy the criteria and the radiation conditions while minimizing the error between the two radiation patterns, i.e., ideal radiation pattern achieved from a ULA and with the desired radiation pattern obtained from a proposed MAMP. The algorithm uses basic formula from Balanis and Ohm's law to find the impedances thus calculates the corresponding weights at the active feeding ports. As per the radiation conditions introduced in chapter 2, the real part of the input impedance must be greater than zero, to assure that each antenna element is radiating. A new cost function is introduced, by integrating the radiation efficiency of the MAMP array. The algorithm minimizes the error between the radiation patterns and optimizes the maximum radiation efficiency.

## 3.5. MAMP DESIGN AND RESULTS

### 3.5.1. COMPUTATION OF LOADS

A multi-active / multi-passive parasitic antenna array is considered with 2 active and 12 parasitic elements. The load values are obtained using SBA with new radiation conditions such that the whole array radiates. The desired radiation efficiency of the array is calculated by using the equation (3.17). There is a possibility that the SBA generates the negative load values (negative real part of the loads, which means the negative resistive

part) which is difficult to implement in real-time. So, the algorithm is modified in such a way that it ensures the following four steps:

1. the algorithm computes the radiation efficiency of the array by using given parameters,
2. it compares the radiation patterns of the proposed MAMP array with that of the ideal radiation pattern produced by the ULA,
3. it generates the optimized passive load values,
4. it performs checks to satisfy all the radiation conditions which ensure that the whole array radiates, and the input impedance is greater than zero at all feeding ports.

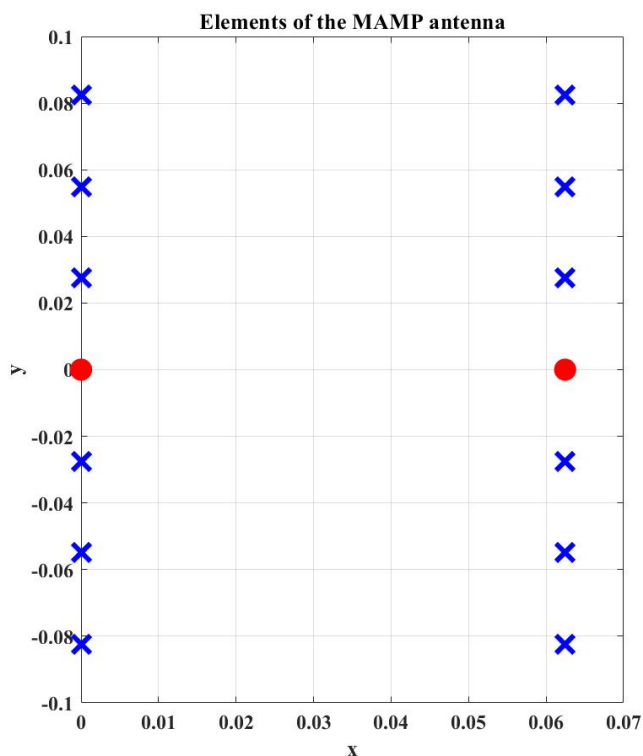


Figure 3-2 MAMP geometry in MATLAB; blue-colored crosses represent the parasitic elements, and the red dots represent the active elements.

The resonant frequency is 2.4GHz and the elements are considered as point sources for the calculation of loads. The mutual coupling and the self-impedance of the elements are

calculated using Balani's equations which are based on point sources. The active elements are placed at half wavelength whereas the parasitic elements are placed at  $0.22*\lambda$  from each other. The elements must be placed close enough so that the effect of mutual coupling constructs in such a way that it produces higher currents at the neighboring elements. Many iterations were carried out before finalizing the inter-element distance. An optimized value is obtained after multiple calculations and that satisfies all the conditions and constraints.

The optimal value may not produce the realistic values of the loads, and it may not have enough efficiency, so the algorithm has to go through more iterations. The tradeoff between the efficiency and the ideal radiation pattern exists and it can be obtained by getting the error in terms of the comparison between the radiation pattern of the proposed MAMP array and the radiation pattern of the ideal ULA. This can be controlled by using the weights as defined in the cost function (3-18). This pattern is achieved after many iterations of the algorithm based on specific sequence and parameter variations of the algorithm to get the optimized loads and weights for the required radiation efficiency and the radiation pattern. Where the values are;  $M = 40$ ,  $\tau = 100$ ,  $MAXITER = 10000$ ,  $T_{er} = 10^{-6}$ ,  $eps = 10^{-10}$ ,  $\omega = 0.65$ ,  $\mu = 0.35$ .

The sequence and variation parameters might have to change to get the optimized results for different angles to achieve the beam steering. As the tradeoff exists between the radiation efficiency and the radiation pattern so is the difference in the values of the above parameters. It is very difficult to achieve the optimized and desired results with the same values of the parameters. So, in order to get the beam steering, the distance between the elements can be changed, but this is a big challenge to find the beam steering angles with a fixed distance among the elements. The sequence parameters play a crucial role in computing the load values for the desired radiation efficiency and the desired radiation pattern. After many iterations and computations, the proposed distance is obtained which ensures beam steering at different angles with a fixed inter-element distance. At this stage, algorithm is considering the same weights at both active ports due to the complexity of implementation and experimentation at the later stage.

Another challenge is to find out the optimized passive load values and then the realistic load values. The sequence parameters control the limit of digits as well as the load values, which makes it either possible or not to implement the parasitic antenna array. Prior knowledge of the values for passive components existing in the market is necessary to get the easily available load values.

### 3.5.2. SIMULATIONS USING CST MICROWAVE STUDIO

The MAMP array setup as shown in Figure 3-2 is emulated in CST microwave studio to get the emulated results of the proposed antenna array. The geometry of the array is shown in Figure 3-3, where finite length half-wave dipoles are considered to develop the

proposed MAMP array in CST as it is not possible to simulate a point source in simulation tools. The thickness of the dipoles is decided after the survey, where some copper tubes are commercially available. The frequency of the operation is 2.4GHz. FR-4 is used as a substrate to support the copper cylinders. The active elements are fed by two microstrip feed lines and are excited by using SMA connectors. Both the active monopoles are fed by using SMA connectors through microstrip lines and are grounded partially, whereas all the monopoles are embedded on the top layer with copper pads and are grounded through via holes. The monopoles on the top are connected to passive components and are embedded on the pads at the top layer, see Figure 3-4(a). These passive components are then grounded through via holes and connected to the grounded monopoles, as shown in Figure 3-4(b). CST simulations are performed using the time domain and the integral solvers, whereas the CST license is provided by Aalborg University, Denmark.

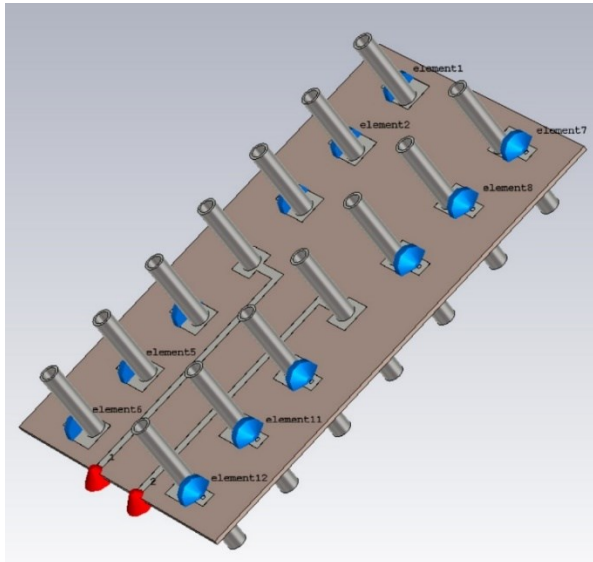
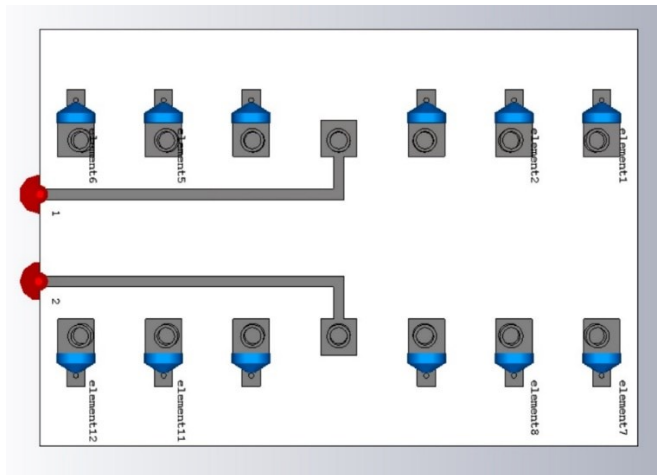
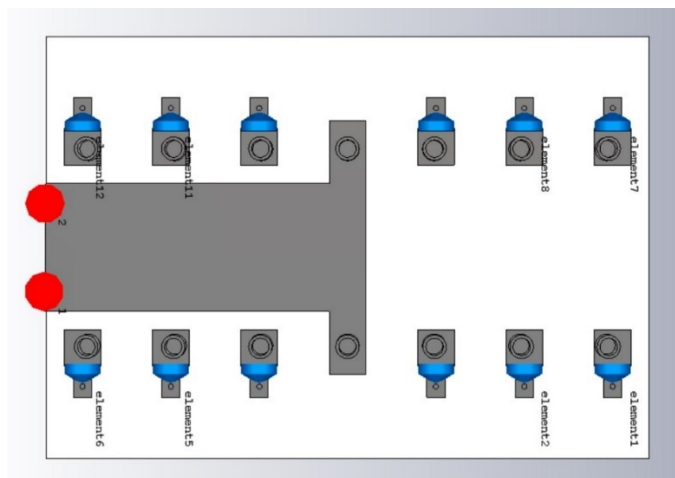


Figure 3-3 The geometry of the MAMP array in CST, the cylinders are half-wave dipoles connected to passive components and grounded through via holes. The blue dots are the loads (passive components, capacitors, or inductors calculated from SBA) whereas the red dots are the feeding ports to feed the active elements.

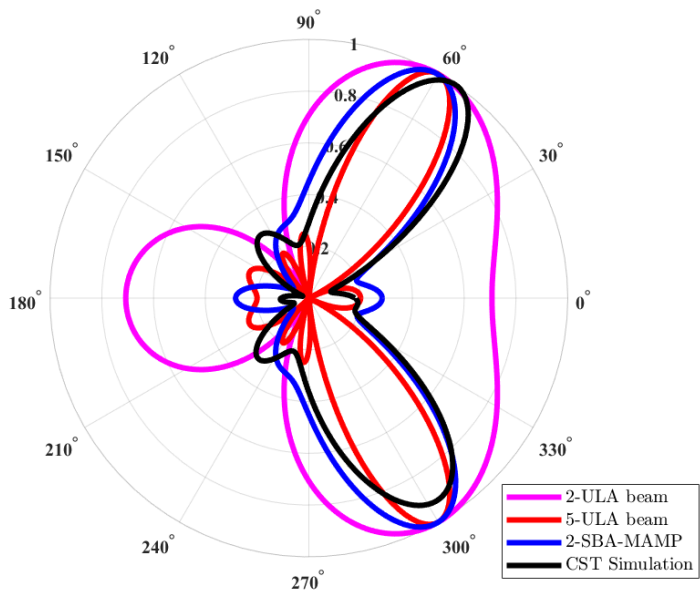


(a)

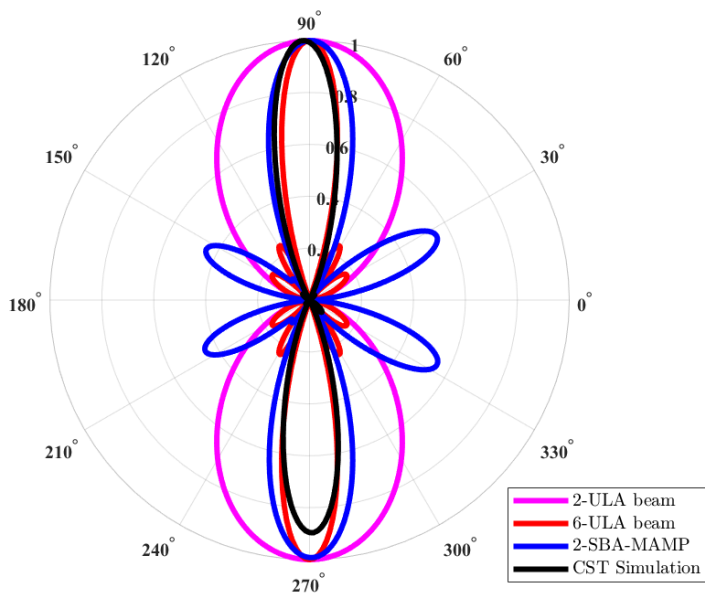


(b)

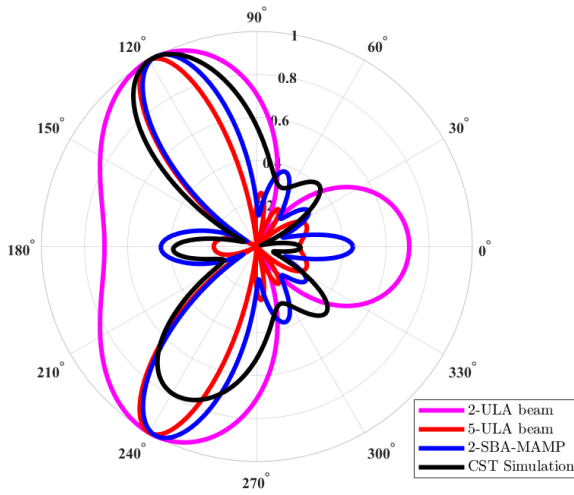
Figure 3-4 The geometry of the MLAMP in CST: (a) Top view of the structure, (b) bottom view.



(a)

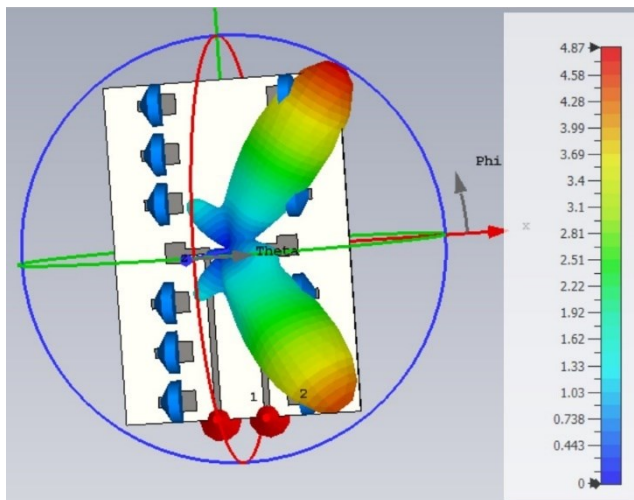


(b)

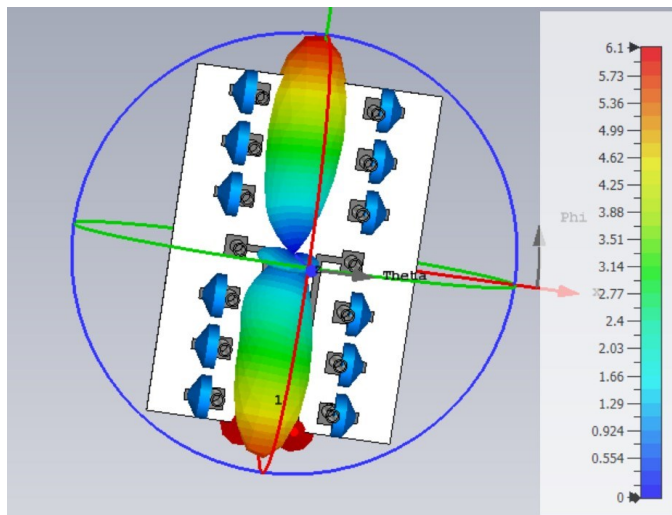


(c)

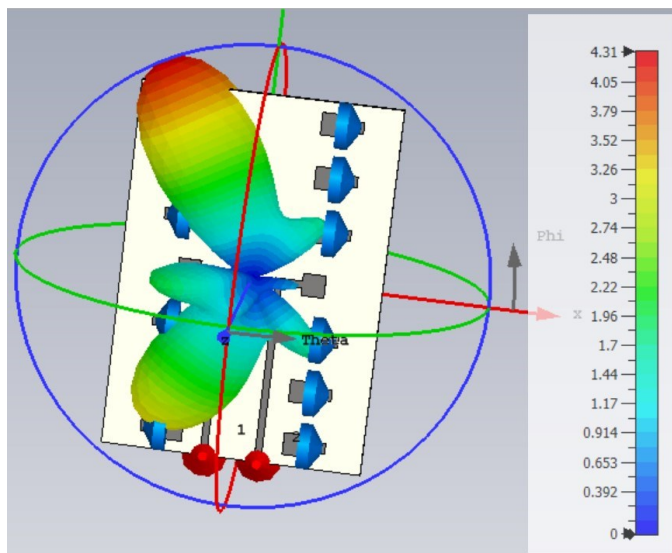
Figure 3-5 Calculated and simulated radiation pattern of MAMP PAA, comparison of the radiation patterns where magenta is representing a ULA with 2 active elements, red is for the 5 ULA to be compared with the MAMP beam, blue is the calculated beam pattern of MAMP using SBA based on different combination of loads and black is the radiation pattern of MAMP array obtained from CST simulations: (a) beam directed towards  $\varphi = 60^\circ$  (b) beam directed towards  $\varphi = 90^\circ$  (c) beam directed towards  $\varphi = 120^\circ$ .



(a)



(b)

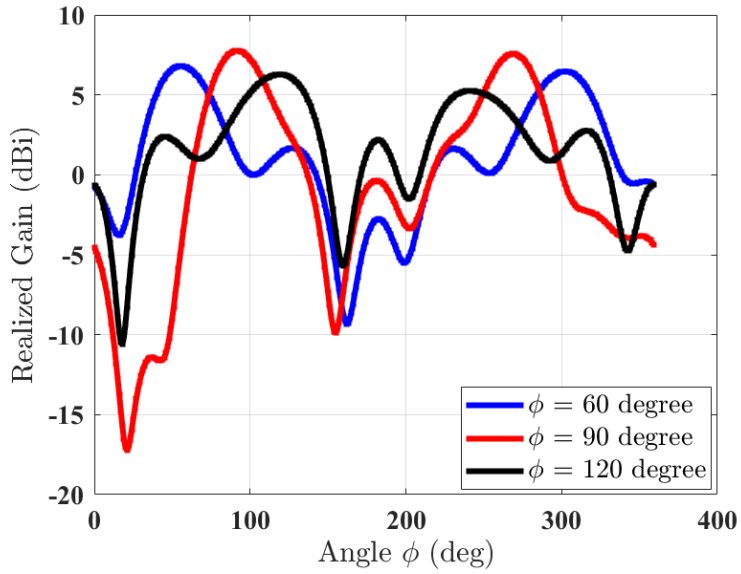


(c)

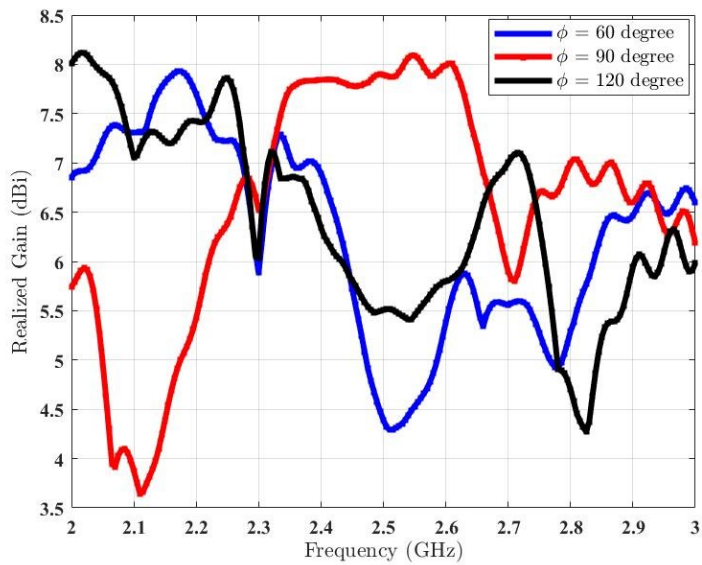
Figure 3-6 The 3D Radiation pattern of the MAMP array obtained from CST simulations: (a) beam directed towards  $\varphi = 60^\circ$  (b) beam directed towards  $\varphi = 90^\circ$  (c) beam directed towards  $\varphi = 120^\circ$ .

A comparison of the radiation patterns is shown in Figures 3-5 (2D polar plots) and 3-6 (3D radiation patterns). The radiation patterns are computed using the SBA for a number of examples and different angles. For a specific application, the proposed MAMP is compared with a 5-active element ULA. The curve in red color represents the ideal radiation pattern of a 5-dipole ULA. The magenta represents the ideal beam of a ULA but with the same number of elements as the number of active elements in MAMP. The radiation pattern computed by SBA for the MAMP is presented in blue color, whereas the simulated radiation pattern of the MAMP is represented in black color. This figure can be explained in three steps:

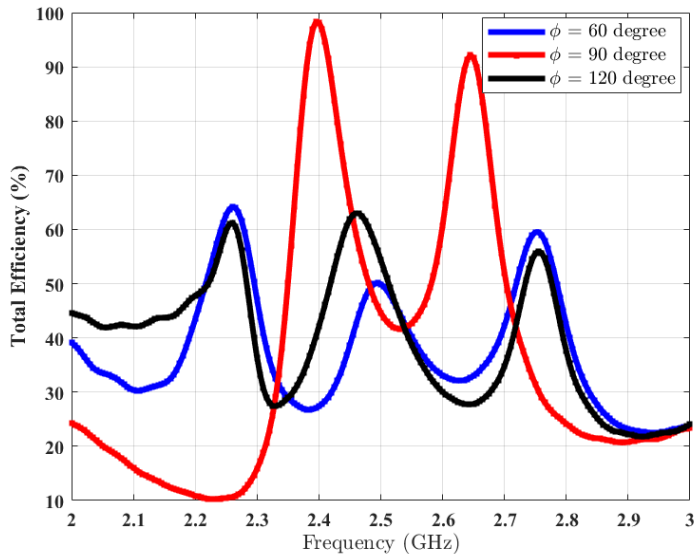
1. At first, the comparison between the MAMP and the ULAs shows that the desired radiation pattern or beam can be obtained by reducing the number of active elements thus the number of RF chains. Even with the reduced number of active elements, we can still get a similar beam which is similar to the conventional ULAs.
2. Then the comparison is between the simulated and the calculated beams by CST and the algorithm. The side lobes in simulated results are bigger than the calculated beams. This most likely is due to the non-ideal finite length designs in the simulation tool. The calculated beams are based on the ideal point sources whereas the ideal simulations are not possible in the simulation tool. Sometimes, residues add up to give higher values at the end of each iteration.
3. Figure 3-5 shows the beamforming at different selected angles. Different beam angles can be obtained by just changing the load values at the parasitic elements. Different examples are shown with the (a) beam directed towards  $\varphi = 60^\circ$  (b) beam directed towards  $\varphi = 90^\circ$  and (c) beam directed towards  $\varphi = 120^\circ$ .



(a)



(b)



(c)

Figure 3-7 Comparison of different parameters of MAMP array while the beam was directed towards  $\varphi = 60^\circ$ ,  $\varphi = 90^\circ$  and  $\varphi = 120^\circ$  (a) max realized gain against the  $\varphi$  angle (b) max realized gain at the given frequency for all the beam steering angles (c) total efficiency of the MAMP at the given frequency for all the beam steering angles.

A comparison of different parameters such as realized gain and total efficiency is shown in Figure 7. The different colors of curves represent the beam steered towards the specific desired direction. The peak realized gain for an angle directed towards  $\varphi = 60^\circ$ ,  $\varphi = 90^\circ$  and  $\varphi = 120^\circ$  is 6.8dBi, 7.75dBi and 6.28dBi respectively. The 3dB angular beamwidth in each case is 44.30, 40.80 and 55.20 respectively. The total efficiency of the MAMPs is 27.3%, 98% and 42% respectively.

### 3.5.3. MAMP ANTENNA ARRAY PROTOTYPE

The MAMP antenna array prototype is developed at University College London (UCL). Figure 3-7 shows the developed antenna, where copper dipoles are embedded on the FR substrate. The developed prototype is tested using a network analyzer to see the resonance of the antenna. Figure 3-8 shows the setup for the measurements of the S-parameters. Where the antenna ports are connected to the power splitter/combiner and the input of the VNA is connected to the splitter's input port. MAMP antenna is also

tested in an anechoic chamber in a facility at Intracom Defense (IDE), Greece. The radiation pattern of the prototype is measured in the chamber. The measurements setup and the developed antenna are shown in Figure 3-9.

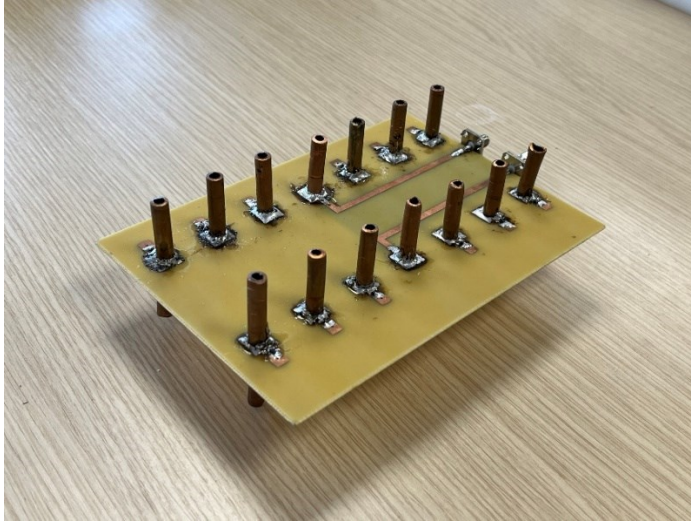


Figure 3-8 MAMP antenna array prototype.

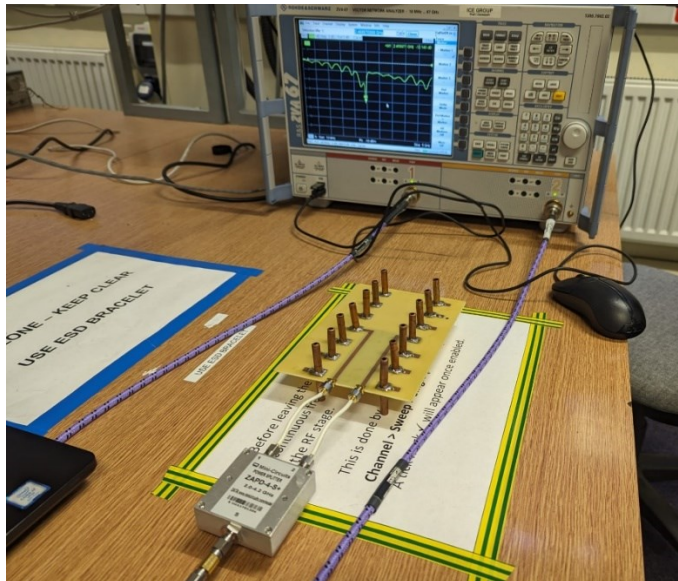


Figure 3-9 Setup for measuring the S-parameters using a vector network analyzer.

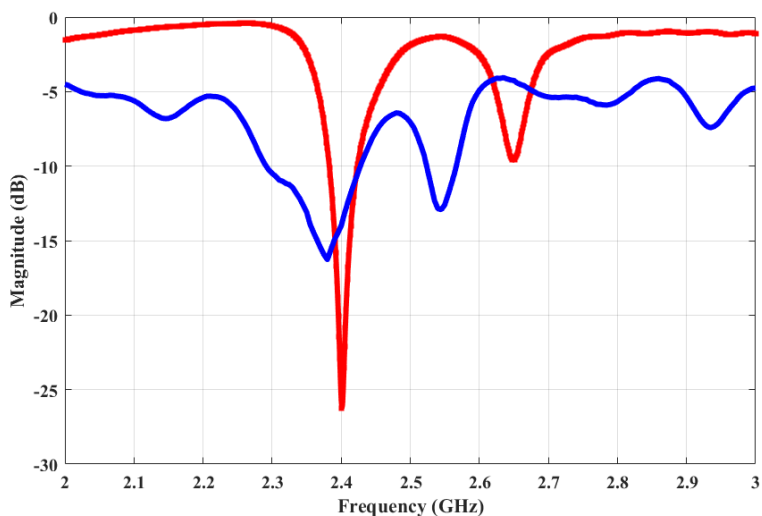
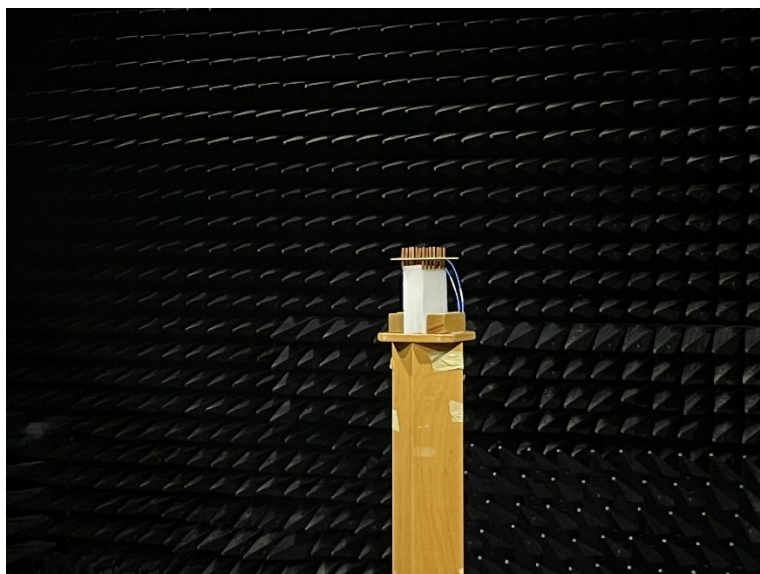
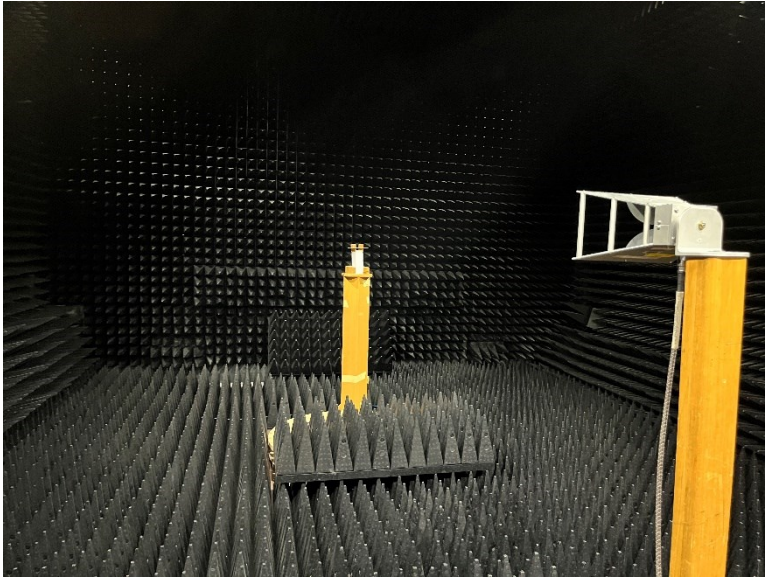


Figure 3-10 Measured and simulated S-parameters of the MLAMP antenna array. The red curve represents the simulated while the blue is representing the measured S-parameters of the structure.



(a)



(b)

Figure 3-11 Measuring radiation pattern in the anechoic chamber: (a) antenna under test (b) setup for the measurement of radiation pattern.

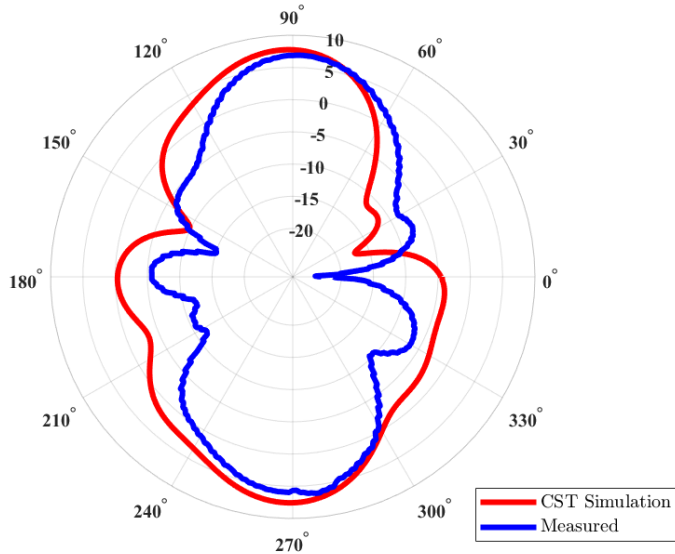


Figure 3-12 Measured and simulated radiation patterns of the MAMP antenna array.

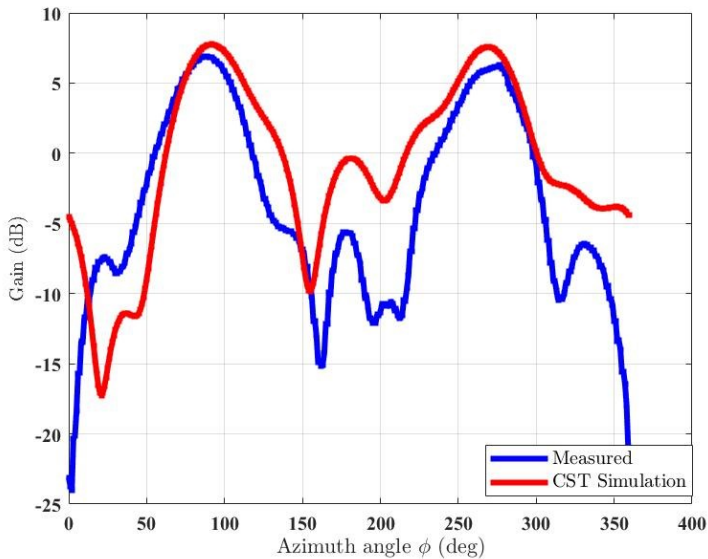


Figure 3-13 Measured and simulated gain of the MAMP antenna array.

The computed load values for all the beam steering angles are given in Table 3-1.

Table 3-1. Load values for parasitic elements

Elements	Beam steering angle					
	$\varphi = 60^\circ$		$\varphi = 90^\circ$		$\varphi = 120^\circ$	
	C(pF)	L(nH)	C(pF)	L(nH)	C(pF)	L(nH)
Element-1	1.13	-	-	0.667	-	9.9
Element-2	1.64	-	-	6.8	0.39	-
Element-3	1.59	-	0.3	-	-	5.3
Element-4	1.60	-	0.3	-	-	5.48
Element-5	1.64	-	-	7.2	0.39	-
Element-6	1.13	-	-	0.667	-	10.8
Element-7	-	1.91	10	-	1.32	-
Element-8	0.45	-	-	12	1.26	-
Element-9	-	7.1	0.3	-	1.46	-
Element-10	-	6.86	0.3	-	1.46	-
Element-11	0.45	-	-	12	1.26	-
Element-12	-	1.89	10	-	1.31	-

Figure 3-12 shows both the simulated and the measured radiation pattern of the antenna array. The shapes are similar, the peaks and the nulls, whereas the measured radiation

pattern has a smaller beamwidth. The peak gain of the simulated antenna is **7.75dBi** whereas the peak gain of the measured antenna is **6.9dBi**. The difference in the peak gains could be due to the cable losses and the connectors. It can also be due to the losses at passive components. The simulated radiation efficiency of the MAMP is **98%**. Both simulated and measured results depict the excellent performance of the MAMP array at the given frequency. The beamforming is also shown with the development of hardware design. The peak gain of the proposed antenna can be further enhanced by placing a reflector to reduce the back lobe. It can also be enhanced by adding a greater number of parasitic elements and then further the active element as per the requirements of the application. Implementation of the MAMPs for replacement of conventional MIMO systems is a possible future extension of the state of the art. The domain can be further expanded in different domains, for example, to find the possible weights and the spatial multiplexing for MIMO, implementation of varactors for the beamforming, etc.

In previous works, (see Table 3-2) authors considered only ensuring the radiation of the array, but radiation efficiency was neglected. We have introduced another constraint which says that the radiation efficiency of the array must be equal to or greater than  $\xi$  to make sure that the MAMP array is radiating and is also radiating enough to cope with the requirements of a well-matched radiating antenna array. In this example, radiation efficiency is introduced in the cost function where loads and weights are optimized based on the stochastic beamforming. The computed loads and weights are incorporated in the cost function to calculate the radiation efficiency and the radiation pattern of the MAMP array.

Table 3-2. Comparison between the proposed work and the reported works

Previous work	Key technique	Radiation constraint	Load values	Radiation efficiency	Prototype development
Hamiltonian method [4]	Beamforming using ESPARs	No radiation constraints	Complex	No	No
Sequential perturbation [5]	Beamforming using ESPARs	No radiation constraints	Complex	No	No
Cross-correlation coefficient maximization technique [6]	Beamforming using ESPARs	No radiation constraints	Complex	No	Yes
Simultaneous perturbation stochastic approximation (SPSA) [7]	Beamforming using ESPARs	No radiation constraints	Complex	No	No
Beam space model [8–11]	spatial multiplexing of QPSK symbols	No radiation constraints	Complex	No	Yes

Reactance Domain Multiple Signal Classification (RD-MUSIC) algorithm [12]	Implementation of direction of arrival estimation	No radiation constraints	Complex	No	No
Rotational invariant technique (ESPRIT) [13]	Implementation of direction of arrival estimation	No radiation constraints	Complex	No	Yes
Design guidelines and the radiation constraints [14]	Beamforming using PAAs	For single-RF	Complex	No	No
Arbitrary precoding scheme [15]	Beamforming using PAAs	Only for single-RF	Complex	No	No
Quantized load selection [16]	Angle of arrival estimation	Only for single-RF	Complex	No	No
Transmission with peak power constraint [17]	Angle of arrival estimation	Only for single-RF	Complex	No	No
Stochastic beamforming algorithm [18]	Beamforming using PAAs	No radiation constraints	Reactive only	No	No
Design Guidelines [19]	Beamforming using PAAs	For MAMP / partial	Complex	No	No
Stochastic beamforming algorithm [20]	Beamforming using PAAs	Only for single-RF	Yes	No	No
Arbitrary Signal model [23]	MIMO transmission	Only for single-RF	Complex	No	No
Arbitrary signal [24]	MIMO transmission	Only for single-RF	Complex	No	No
Quantization of loads [25]	MIMO transmission	Only for single-RF	Complex	No	No
Beam steering [26]	MIMO ESPARs	Only for single-RF	Complex	No	Yes
Stochastic beamforming algorithm [27]	Beamforming using PAAs	No radiation constraints	Reactive only	No	No
[Our work] Stochastic beamforming algorithm	Beamforming using PAAs	For a whole MAMP	Reactive only	RE integrated in cost function	Yes

### 3.6. REFERENCES

- [1] A. Kalis, A. G. Kanatas, C. B. Papadias, *Parasitic Antenna Arrays for Wireless MIMO Systems*, Springer 2014.
- [2] C. A. Balanis, *Antenna Theory: Analysis and Design*, Hoboken, NJ, USA: Wiley, 2012.
- [3] D. M. Pozar, *Microwave Engineering*, Hoboken, NJ, USA: Wiley, 2012.
- [4] A. Komatsuzaki, S. Saito, K. Gyoda and T. Ohira, "Hamiltonian approach to reactance optimization in ESPAR antennas," *Asia-Pacific Microwave Conference. Proceedings (Cat. No.00TH8522)*, pp. 1514-1517, 2000.
- [5] Jun Cheng, Y. Kamiya and T. Ohira, "Adaptive beamforming of ESPAR antenna using sequential perturbation," *IEEE MTT-S International Microwave Symposium Digest (Cat. No.01CH37157)*, vol.1, pp. 133-136, 2001.
- [6] Chen Sun, A. Hirata, T. Ohira and N. C. Karmakar, "Fast beamforming of electronically steerable parasitic array radiator antennas: theory and experiment," *IEEE Transactions on Antennas and Propagation*, vol. 52, no. 7, pp. 1819-1832, July 2004.
- [7] J. C. Bucheli Garcia, M. Kamoun and A. Sibille, "On the performance of ESPAR for spatial multiplexing in reception," *IEEE Wireless Communications and Networking Conference (WCNC)*, pp. 1-5, 2019.
- [8] A. Kalis, A. Kanatas, and C. B. Papadias, "A novel approach to MIMO transmission using a single RF front end," *IEEE Journal on Selected Areas Communications*, vol. 26, no. 6, pp. 972-980, Aug. 2008.
- [9] O. Alrabadi, C. B. Papadias, A. Kalis, and R. Prasad, "A universal encoding scheme for MIMO transmission using a single active element for PSK modulation schemes," *IEEE Transactions on Wireless Communications*, vol. 8, no. 10, pp. 5133-5142, Oct. 2009.
- [10] V. Barousis, A. Kanatas, and A. Kalis, "Beamspace-domain analysis of single-RF front-end MIMO systems," *IEEE Transaction on Vehicular Technologies.*, vol. 60, no. 3, pp. 1195-1199, Mar. 2011.
- [11] O. Alrabadi, J. Perruisseau-Carrier, and A. Kalis, "MIMO transmission using a single RF source: Theory and antenna design," *IEEE Transactions on Antennas and Propagation*, vol. 60, no. 2, pp. 654-664, Feb. 2012.

- [12] Chen Sun, Nemai Chandra Karmakar, "Direction of Arrival Estimation Based on a Single Port Smart Antenna Using MUSIC Algorithm with Periodic Signals", *International Journal of Electronics and Communication Engineering*, Vol:1, No:11, 2007.
- [13] E. Taillefer, A. Hirata and T. Ohira, "Reactance-domain ESPRIT algorithm for a hexagonally shaped seven-element ESPAR antenna," in *IEEE Transactions on Antennas and Propagation*, vol. 53, no. 11, pp. 3486-3495, Nov. 2005.
- [14] V. Barousis and C. B. Papadias, "Arbitrary precoding with single-fed parasitic arrays: Closed-form expressions and design guidelines," *IEEE Wireless Communications Letters*, vol. 3, no. 2, pp. 229–232, Apr. 2014.
- [15] L. Zhou, F. A. Khan, T. Ratnarajah and C. B. Papadias, "Achieving Arbitrary Signals Transmission Using a Single Radio Frequency Chain," *IEEE Transactions on Communications*, vol. 63, no. 12, pp. 4865-4878, Dec. 2015.
- [16] A. Li, C. Masouros and C. B. Papadias, "MIMO Transmission for Single-Fed ESPAR with Quantized Loads," *IEEE Transactions on Communications*, vol. 65, no. 7, pp. 2863-2876, July 2017.
- [17] L. Zhou, F. A. Khan, T. Ratnarajah and C. B. Papadias, "Single-RF Multi-Antenna Transmission with Peak Power Constraint," *IEEE Transactions on Communications*, vol. 65, no. 12, pp. 5197-5208, Dec. 2017.
- [18] G. K. Papageorgiou, D. Ntaikos and C. B. Papadias, "Efficient Beamforming with Multi-Active Multi-Passive Antenna Arrays," *IEEE 19th International Workshop on Signal Processing Advances in Wireless Communications (SPAWC)*, pp. 1-5, Kalamata, Greece, 2018.
- [19] M. H. Tariq, D. K. Ntaikos and C. B. Papadias, "Design Guidelines for Multi-Active/Multi-Passive Parasitic Antenna Arrays," *IEEE Antennas and Wireless Propagation Letters*, vol. 19, no. 12, pp. 2141-2144, Dec. 2020.
- [20] V. Barousis, A. G. Kanatas, A. Kalis and C. Papadias, "A Stochastic Beamforming Algorithm for ESPAR Antennas," *IEEE Antennas and Wireless Propagation Letters*, vol. 7, pp. 745-748, 2008.
- [21] M. Capek, L. Jelinek and M. Masek, "Finding Optimal Total Active Reflection Coefficient and Realized Gain for Multiport Lossy Antennas," *IEEE Transactions on Antennas and Propagation*, vol. 69, no. 5, pp. 2481-2493, May 2021.

- [22] M. Wang, T. -H. Loh, Y. Zhao and Q. Xu, "A Closed-Form Formula of Radiation and Total Efficiency for Lossy Multiport Antennas," *IEEE Antennas and Wireless Propagation Letters*, vol. 18, no. 12, pp. 2468-2472, Dec. 2019.
- [23] V. I. Barousis, C. B. Papadias and R. R. Müller, "A new signal model for MIMO communication with compact parasitic arrays," *6th International Symposium on Communications, Control and Signal Processing (ISCCSP)*, pp. 109-113, Athens, Greece, 2014.
- [24] L. Zhou, F. A. Khan, T. Ratnarajah, and C. B. Papadias, "Achieving arbitrary signals transmission using a single radio frequency chain", *IEEE Transactions on Communications*, vol. 63, no. 12, pp. 4865-4878, December 2015.
- [25] A. Li, C. Masouros, and C. B. Papadias, "MIMO transmission for single-fed ESPAR with quantized loads," *IEEE Transactions on Communications*, vol. 65, no. 7, pp. 2863-2876, 2017.
- [26] Y. Zhou, R. Adve, and S. Hum, "Design and evaluation of pattern reconfigurable antennas for MIMO applications," *IEEE Transactions on Antennas and Propagation*, vol. 62, no. 3, pp. 1084–1092, Mar. 2014.
- [27] G. K. Papageorgiou, M. Sellathurai, D. K. Ntaikos and C. B. Papadias, "3D Beamforming with Multi-Active Multi-Passive Antenna Arrays Using Stochastic Optimization," *IEEE 21st International Workshop on Signal Processing Advances in Wireless Communications (SPAWC)*, pp. 1-5, Atlanta, GA, USA, 2020.

# CHAPTER 4. PROPAGATION MEASUREMENTS AND CHANNEL MODELING

Many mmWave measurements were performed as part of the thesis. Considering the importance of mmWave frequencies for future wireless communications, self-backhauling via small cell stations or fixed wireless base stations is considered as a primary application for the measurements campaign. Where, a fixed wireless access point is mounted on a streetlamp post and provides a gigabit wireless backhaul without an optic fiber or any cable through a glass window and through vegetation. The work is related to the title of the thesis and gets the motivation from the EU's ITN project PAINLESS. This work is related to the previous chapters to give a complete treatment for self-backhauled base stations. A MAMP is not considered at this stage due to the complexity in the design and fabrication restrictions at such higher frequencies. A complete setup scenario can be considered with a MAMP for an access /fronthaul link and mmWave horn for the backhauling. There are many factors that determine the performance of wireless communications. One such factor is attaining appropriate coverage, especially for mmWave bands. It is imperative to have models that evaluate wireless communication systems' performance. Such models should also be able to assess the requirements in general scenarios. Another factor, which will also aid in meeting the rising data traffic demands, is the broad spectrum in mm bands. To design dependable systems, it is highly important to comprehend the link losses at these frequencies. One revolutionary system in wireless communications could be using FWA at 60GHz. This would result in obtaining high data rates without relying on physical connections, for instance via optic fibers or copper cables. However, link losses due to several factors, for instance, scattering, blockage, etc. must be taken into consideration. Comprehensive data has been collected through multiple mmWave and cm (60 GHz) measurement campaigns in Athens, Greece. These campaigns were conducted from outdoor to indoor scenarios at different locations ranging from inside the campus to off campus to downtown Athens. Path loss, angular spread and curve fitting are shown for multiple outdoor to indoor scenarios and are presented with very useful outcomes at 60Ghz.

## 4.1. INTRODUCTION

Wireless communication systems are thriving with the increased global demand for internet connectivity, mobile devices, and smart-city applications. According to reports,

there will be a drastic increase in the quantity of connected devices by the end of 2025 [1–3]. The demand for faster data services has resulted in the need for a large amount of bandwidth. This has become the chief goal of 5G services with an aim to increase the frequency spectrum and coverage [4–7]. Reliability plays a vital role in coverage to achieve high benefits of wireless networks, which could only be done by the development of accurate propagation models for mmWave frequencies. In the past few years, scientists have performed rigorous research in the quest to present different models and measurements [8–16]. Numerous studies have been conducted in the fifth-generation technology to determine path loss by considering various factors such as antenna height, distance and frequency, etc. [17–19]. Certain models have shown a suitable accuracy, which is supported by large experimental data, for instance, the alpha-beta-gamma model and the closed in model [20]. Antenna height and propagation frequency affect the internal modeling. It is possible to cover a large area with the help of increased height of the transmitting antenna. However, if the area is beyond 300m, improvements are required in the subject area as proven in [21–22].

Ray tracing [23–24] and empirical models [25] are some of the renowned approaches for propagation modeling in communications. Although ray tracing needs detailed environmental information, it can predict full impulse response to handle general environments. Detailed information includes specifications of interior walls, furniture information as well as vegetation. Different empirical models have shown that path gain depends on gain for certain scenarios instead of considering distance and line of sight or non-line of sight [26]. It is, therefore, imperative to develop models that are more compliant with local conditions. The ideal models are accurate, simply implemented, and depend solely on available environmental factors. Empirical models are not dependent on complex programming but reducing site-specific measurements would be worthy [27]. An analytical model for universal path gain laws has been introduced which is achieved by a numerical solution over rooftop propagation, outdoor to indoor, through trees and foliage in the streets.

#### **4.1.1. LIMITING FACTORS FOR MILLIMETER WAVE COMMUNICATIONS**

1. Atmospheric absorption of signals occurs due to various gases in the atmosphere [3].
2. The attenuation due to rain and snow can be dealt with by an increase in the antenna gain [19]. The rain direction and size of the rain drops and even the clouds can affect this.
3. Higher antenna gain is a pre-requisite for achieving optimal beamforming at millimeter waves [29].
4. The beam steerable antenna principle is important to counter interference [45, 30].

5. The biggest challenge for mmWave communications is penetrating buildings. This is in contrast to microwave systems that don't face this challenge [31].
6. Due to scattering, many differences occur in signals during short distances. It is important to consider these differences in the designs of sending and receiving the signal [32].
7. Reflection phenomenon can cause a change in the channel frequency response due to the multipaths of identical signals.
8. Some measurements have reported that signals are lost due to diffraction [33].
9. The human body can also cause blockage of the signal and should be considered as well [34–35].
10. Millimeter waves are affected by an increased path loss [43–45].  
Other weather factors like rain, hail dust, and fog attenuate frequencies beyond 10 GHz [46].

#### 4.1.2. CHANNEL MODELING

It is imperative for simulation models that simulate propagation to be both reproducible and cost-effective. Channel models aid in the accurate deployment of transmission systems. Developing a channel model entails detailed environmental conditions, for instance, urban/suburban/rural scenarios, foliage, and building materials, and technical parameters, for instance, frequency, distance, antenna heights, and gains. The present world requires higher data rates due to increased demands, which requires efficient 5G deployment. 5G in turn requires a higher bandwidth which can be acquired by mmWave frequencies. Channel propagation on mmWave frequencies is a gigantic challenge because of shorter wavelengths due to increased absorption rates, path loss, etc.

Researchers, scientists, and numerous organizations are developing different 5G models. One of these organizations is the Third Generation Partnership Project (3GPP TR 38.901 [37]). This project aims to develop channel models at the frequency range of 6 to 100 GHz [43]. Another model is the 5G Channel Model. This model is based on big data obtained by a plethora of measurement campaigns organized by a number of academic institutes and companies around the world [40]. Two major projects, sponsored by the European Union, are METIS and mmMAGIC [38, 32]. In this chapter, a new channel model is discussed for 60GHz wireless propagation which seems an extension of [27] where universal path gain models and solutions are presented in closed forms for 28GHz. Path gain curve fitting is shown in the latter part of this chapter considering outdoor to indoor scenarios compared to the theoretical models and the data achieved through comprehensive channel measurement campaigns in Athens, Greece.

#### 4.2. OUTDOOR TO OUTDOOR

We present the findings from a cmWave channel measurement campaign [50] performed in different indoor and outdoor scenarios as part of our contribution to the mmWave

Network Project Group of the Telecom Infra Project (see <https://telecominfraproject.com/mmwave/>). Indoor scenarios included workspace environments such as office rooms, corridors, etc. whereas, outdoor scenarios included urban and suburban environments. A set of two 802.11ad Terragraph™ Channel Sounder nodes (provided by Facebook under TIP) equipped with massive MIMO antenna arrays integrated with phase shifters was used as the transmitter and the receiver for the characterization of the 60GHz cmWave channel. The measurement results include path loss, received power, input and output SNR and delay spread values for each specified beam combination. Urban, suburban and indoor environments were tested in both Line of Sight (LoS) and Non-Line of Sight (N-LoS) configurations.

The sounder nodes were used as transmitter and receiver nodes for measuring and characterizing the 60GHz mmWave channel. The nodes were provided by the Telecom Infra Project (TIP) community, along with the respective software and other peripherals. Each node has a massive 288-element mmWave antenna array whose beam width and beam direction can be controlled by phase shifters. By choosing different modes, the beamwidth of the nodes can be varied from 2.8° to 102° and the specific beam could be scanned from -45° to 45° in either elevation or azimuth planes. Path loss, received power, input and output SNR and delay spread values of the measurements are provided by the accompanied software. The transmitter has a gain of 20dB with narrowest beamwidth of 2.8° whereas the receiver has 30dB gain with 8.5° beamwidth. The measurements were carried out in three different phases and in each phase, different scenarios were considered, all these scenarios are shown in Table 4-1.

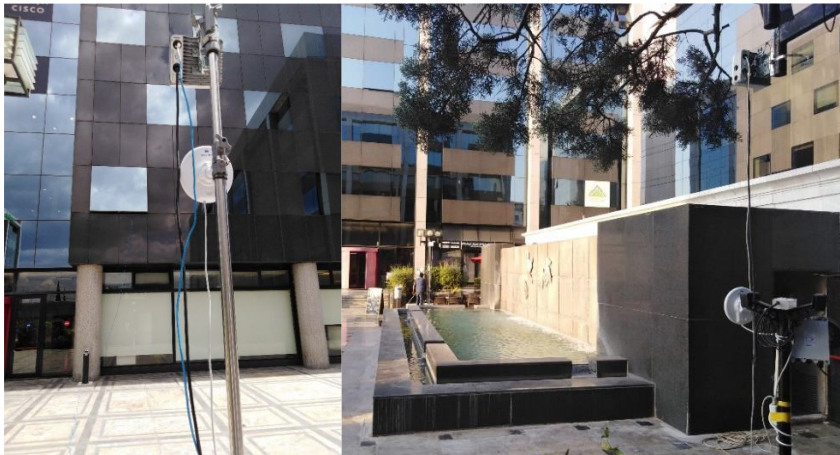
Table. 4-1 Consolidated different phases/scenarios

Scenario	Tx /Rx location	Tx-Rx distance (m)	Tx/Rx height (m)	Setup
S2	Pole/Pole	55	3.5/3.5	Outdoor-Urban
S3	Pole/Lamp-pole-I	10	2.7/2.7	Outdoor-Urban
S4	Pole/Lamp-pole-II	15	2.7/2.7	Outdoor-Urban
S5	Pole/Lamp-pole-III	22	2.7/2.7	Outdoor-Urban
S6	Pole/Lamp-pole-IV	30	2.7/2.7	Outdoor-Urban
S7	Pole/Lamp-pole-V	40	2.7/2.7	Outdoor-Urban
S8, S9	Left side of the fountain/ Right side of the fountain	24	3/3	Outdoor-Urban
S10	Ground/ First Floor	10	2/6	Outdoor-Urban

S11	Car/ Radio Tower	30–90	2/20	Outdoor-Suburban
-----	------------------	-------	------	------------------



Figure 4-1 Indoor LoS measurements setup: (a) a conference room setup with a distance of 2–6m between Tx and Rx (b) Measurements in the corridor where the distance between Tx and Rx is 20m.



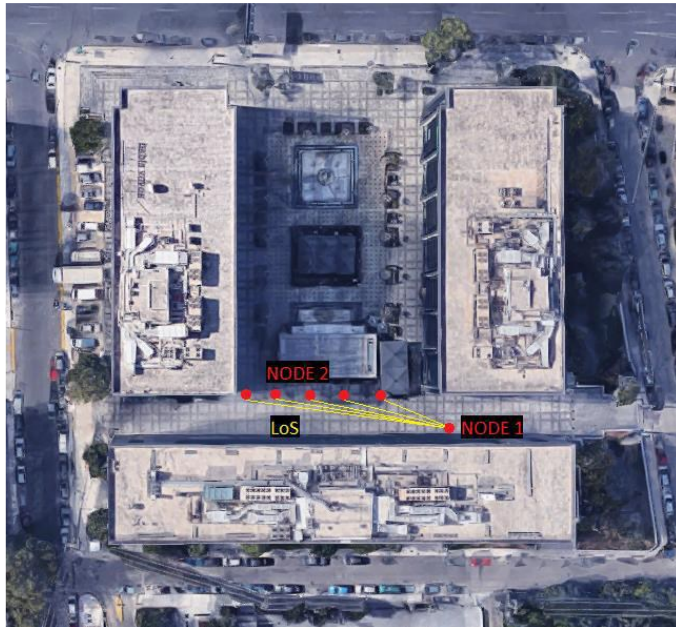


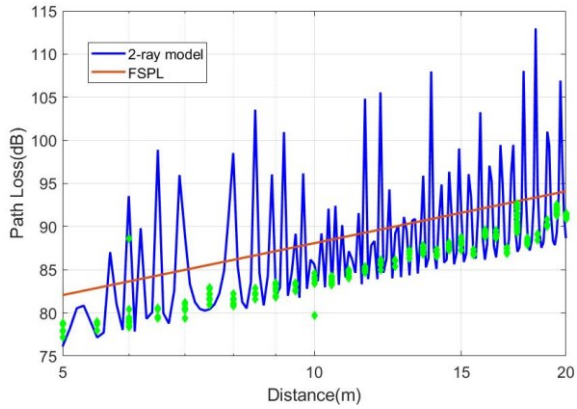
Figure 4-2 Outdoor-outdoor propagation measurements setup for the Facebook sounder nodes outside urban Monumental Plaza in Athens, Greece, sounder nodes are mounted on a street lamp post at a height of 2.7m.



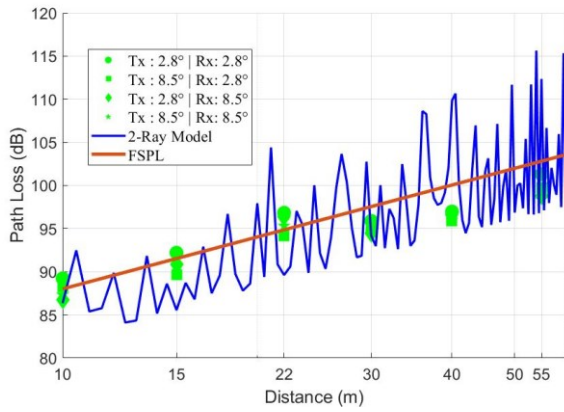
Figure 4-3 Outdoor-outdoor propagation measurements setup for the Facebook sounder nodes in suburban environment, where one sounder is mounted on a commercial telecom provider COSMOTE's tower and the second node is on the roof of a moving SUV.



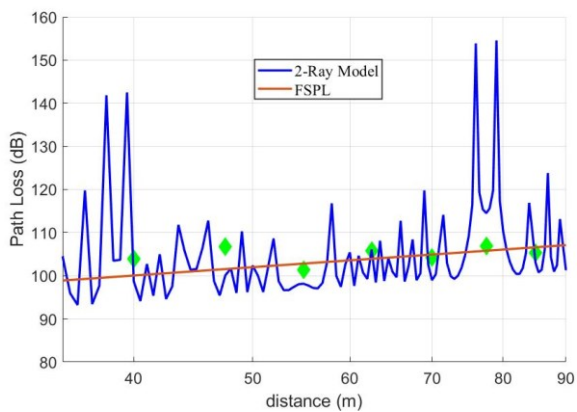
Figure 4-4 Outdoor-outdoor propagation measurements setup for the Facebook sounder nodes in urban environment outside monumental plaza, where both sounder nodes are mounted on lamp posts. The measurements are carried out across a water fountain to see the reflections and the scattering.



(a)



(b)



(c)

Figure 4-5 Measured Pathloss between Tx and Rx over different distances, compared with FSPL and 2-Ray Pathloss models for: (a) Indoor (b) Outdoor urban-Pole to lamp-poles (c) Suburban

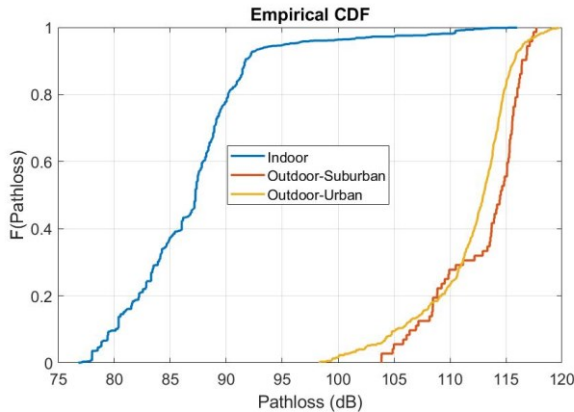


Figure 4-6 The cumulative distribution function (CDF) of pathloss for indoor, outdoor urban and suburban scenarios.

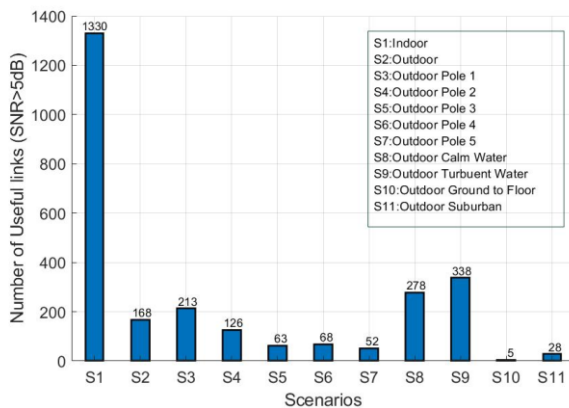


Figure 4-7 The number of useful links in different scenarios when the SNR is greater than 5dB.

A number of measurements were carried out in Athens in the urban and suburban environments for different outdoor-outdoor and some indoor scenarios. The data collected through these measurement campaigns can assist the development of channel models for the deployment of fixed wireless access points and for the backhauling. A 34dB loss over the Free Space Path Loss (FSPL) can be observed in Figure 4-5 perhaps

due to the window attenuation. For the indoor measurements, it shows that the 2-ray model is achieved. At higher distances, the path loss is consistent with free space model. It was not possible to establish a connection in the presence of thick foliage with the narrowest beam. In the presence of turbulent water, it was easier to establish more links.

### **4.3. OUTDOOR TO INDOOR**

#### **4.3.1. NOKIA PHASE-I**

In the American College of Greece (ACG) main campus in Athens, Greece, we have performed extensive outdoor to indoor channel measurements at 60 GHz [50]. The equipment is provided by NOKIA Bell Labs, New Jersey, and it consists of two channel sounders: a transmitter with omnidirectional antenna and a receiver with a horn – this receiver spins from 0 to 360 degrees and provides power measurements at each degree. The measurements were carried out for distances up to 220 meters in different buildings of the campus. These measurements included different parameters, for instance, path loss, angular spread, and received power. A total of 2.4 million individual power measurements were conducted. These measurements [51] aided the assessment of wireless channel for mmWaves.

Channel measurements for indoor, suburban, and urban environments were performed in [51–54] where the path loss was measured between 100–110 dB at the distance range of 40 and 90 meters. This measurement was performed in a suburban environment with line-of-sight scenario. Studies have reported penetration losses during outdoor to indoor channel measurements; these penetration losses mainly depend on the material and the type of glass windows and the incidence angles [55–59]. In the study [61], it is reported that the LOS component can be degraded significantly upon misalignment, thereby leading to a bigger bit error rate. This was reported for an indoor-to-outdoor setting by adopting a BPSK scheme. Although these works have contributed to the examination of many propagation issues at 60GHz communications, they lack the statistical significance of the sample size.

#### **4.3.2. NOKIA PHASE-II**

##### **4.3.2.1 Scenarios and the Setup**

In the second phase of the campaign, we performed off-campus mmWave (60 GHz) measurements. Extensive runs consisted of multiple scenarios (also shown in Table 4-2) starting from the ACG dorms to the building in downtown Athens. Measurements were carried out for the outdoor to indoor scenarios, where the Rx unit was placed on the balcony and then inside the lounge to see the penetration loss through the windows. The transmitting antenna is mounted on a tripod at a height of 3.5m. The objective of these

measurements was to see the oblique angles and the LOS/NLOS for fixed wireless access using street furniture. Path gain plots have been generated to analyze the data. The measurements setup are shown in Figures 4-8, 4-12 & 4-16, where transmitter is placed in a street and the receiver terminal is across the street behind the foliage either in the balcony or inside the building. The operating frequency of the equipment is  $f_c = 60$  GHz, bandwidth  $W = 20$  kHz, max. speed of the spinner is 300 rpm and it can collect up to 702 samples. The Omni at the transmitter has 5dBi gain ( $30^\circ$  HPBW in elevation) whereas big horn at Rx has a gain of 24.9dBi (HPBW  $10^\circ$  in Azim and  $9^\circ$  in Elev). Measurements were performed in the following locations and the scenarios are mentioned in the table below.

Table 4-2 Possible scenarios for the channel measurements at different locations

Locations		Level	Proposed Scenarios		Actual Scenarios
Residence-4	R4	Level – 1	Rx in balcony	S-I	S-I
			Rx inside	S-II	S-II
		Level – 4	Rx in balcony	S-III	S-III
			Rx inside	S-IV	Not possible
ACG External Apartments	EA-I	Level – 4	Rx in balcony	S-V	S-IV
			Rx inside	S-VI	S-V
	EA-II	Level – 3	Rx in balcony	S-VII	S-VI
			Rx inside	S-VIII	Not Possible

### 4.3.2.2 Balcony Measurements

Channel sounders consist of Omni at the transmitter and a horn at the receiver. The horn spins at a max speed of 300rpm and collects the data points for each angle with a step size of one degree. Figure 4-8 shows the scenario when the spinner (Rx unit) is placed in the balcony across the vegetation depth and across the street. The distances and the path gain is calculated according to Bell Lab Model [27]. The Tx is placed across the street at a distance of  $d_s$  whereas Rx is at the balcony after the vegetation with width of  $d_v$  and the range between the omni and the horn is  $r$ .

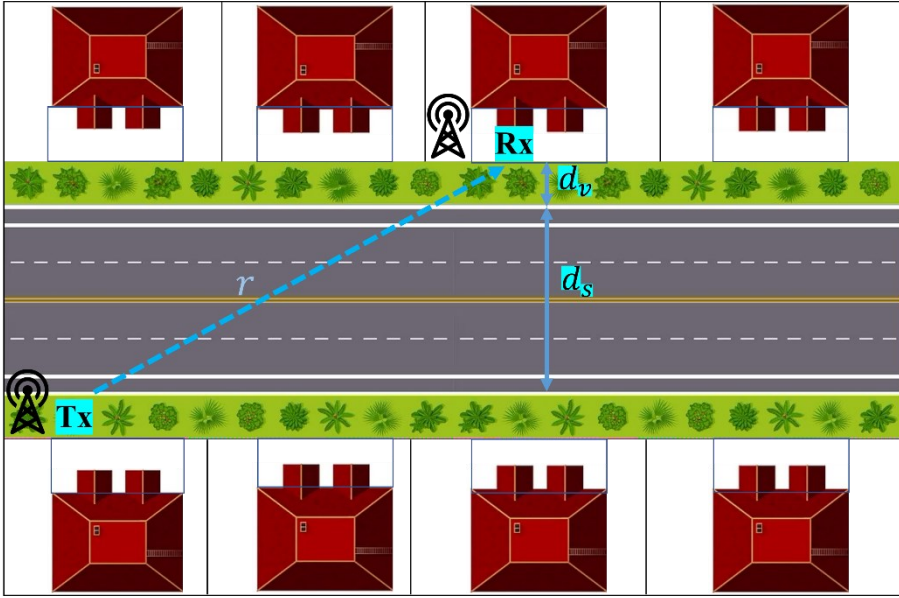


Figure 4-8 Outdoor-Indoor Measurements setup: (a) from street terminal to balcony behind foliage (b) from street terminal to inside terminal behind foliage and the windows.

Path gain for this scenario is given in (4.1), where  $K_v$  (Np/m) is the absorption due to the foliage (for 60GHz, it is 0.79),  $\gamma_g$  is the ground reflection coefficient and  $\gamma_w$  is the wall reflection coefficient. Assuming the scattering and the reflection from across the street walls and the ground is zero at 60GHz and  $T_{eff}=1$  (absorption/penetration through wall between free space transmitter source and the vegetation). The average path gain for this scenario is given by

$$P_{O-I} = \frac{\lambda^2 d_s^2 e^{-K_v d_v}}{8\pi^2 r^4} T_{eff} \left(1 + |\gamma_g|^2\right) \left(1 + |\gamma_w|^2\right) \quad (4.1)$$

Many measurements were collected in Athens' dorms and external apartments for fixed wireless access at 60Ghz. The path gain is measured for varying street distances and the ranges between the transmitter and the receiver. For example, the  $d_s$  is 1 to 3 meters and  $d_v$  is 4m in the case of R4 whereas  $d_s$  is 6m in the case of external apartments and  $d_v$  is 3m. The path gain is shown in Figures 4-9 to 4-11. The path gain is measured for all the balconies where Rx is behind the foliage and the Tx is mounted on a moving mast. The Rx-Tx height difference ranges from 0 to 13m depending on the floor level of the respective building. The trees are not uniformly present in the street, there are some gaps between the trees, which use different  $T_{eff}$  for each scenario depending upon the vegetation depths and the distances.



Figure 4-9 Top and the front view of the residence building (R4), total distance is 240 meters (-104 to 136m) moving from left to the right side of the building.



Figure 4-10 Left and right side of the street facing the building R4.

### Conditions on the day of Measurements

- Slightly cloudy day
- No wind
- Resolution 2m
- Overall altitude height difference was 4m
- Busy road, heavy traffic
- Pavement was busy as well, many pedestrians
- Dense vegetation
- Neighboring buildings were of the same height with glass windows

- R4 has double tinted glass on some levels.
- Metal railing horizontally and vertically across the double-tinted glass
- A big lounge area for students: three sofa sets, three sets of tables and chairs, three desks with PCs, small library. It has two doors, wooden and glass respectively, and two glass windows

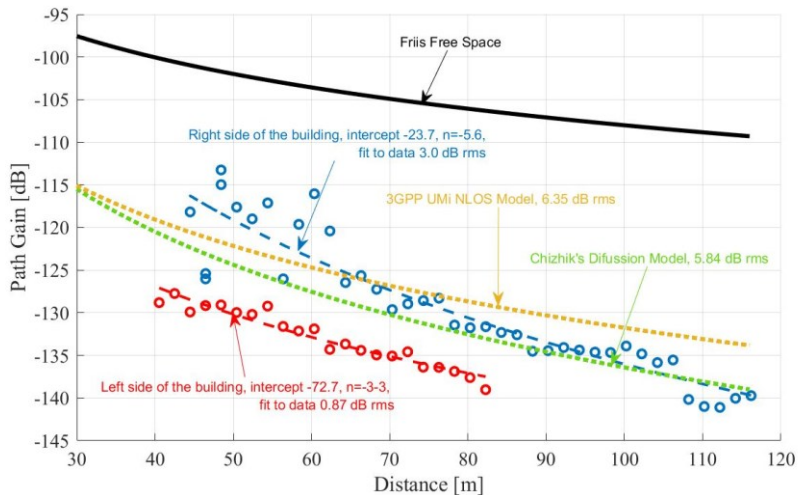


Figure 4-11 Path gain measured in the street from left to right side against the distances for R4 when the receiver is placed at 1<sup>st</sup> floor in the balcony (1m away from the railing). Tx is at 3.5 height, Rx is placed in the balcony at a height difference of 1.65m. Vegetation depth is 4m and the street distance is 3m.

The path gain as shown in Figure 4-11 shows that the left side of the street gives only 0.87dB rms error to linear data fit while the right side of the street is 3dB away from the linear data fit. The Bell Lab model is very close to the data fit with only 5.8dB rms error to all the measurements.

### 4.3.2.3 Over-the-Top Measurements

In this scenario, the Tx is mounted on a tripod at a height of  $Z_m = 3.5\text{m}$  and is placed across the street at a distance of  $w = 10.5\text{m}$  from the receiver. The receiver unit is placed behind the foliage and on the balcony of 3rd floor of the external apartments, then on the 4th floor of the R4 and EA. Rx is 1m away from the railing which is 1m high from the floor and it is a double-tinted glass.

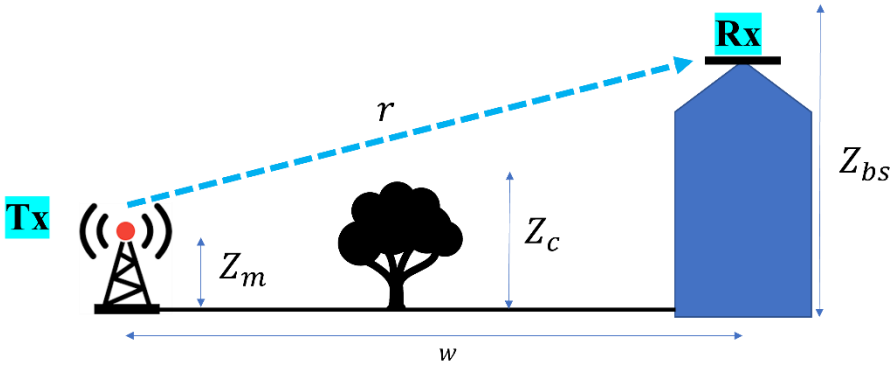


Figure 4-12 Over the top measurements' scenario where Tx is placed at a height of 3.5m and  $w = 10.5m$  away from the Rx.

The proposed path gain is given below.

$$P_{OT} = \frac{\lambda^2 (Z_{bs} - Z_c)^2 e^{-K_v(Z_c - Z_m)}}{8\pi^2 r^4} T_{eff} (1 + |\gamma_g|^2) \quad (4.2)$$

$Z_{bs}$  is the height of the base station (Rx in this case) which is from the ground to the horn,  $Z_c$  is the clutter height or the top of the trees.  $Z_m$  is the height of the mast where transmitter is mounted. As there are a few trees above the terminal in the street and at some points there is free space,  $T_{eff}$  is different in this case which can be found using the equations (4.3–4.5).

$$T_{eff} = |T|^2 \frac{2}{\pi} \tan^{-1} \left( \frac{w_1 w_2}{2d_{in} \sqrt{2d_{in}^2 + w_1^2 + w_2^2}} \right) \quad (4.3)$$

$$T_{eff} = |T|^2 \frac{2}{\pi} \tan^{-1} \left( \frac{w_1}{2d_{in}} \right) \quad (4.4)$$

$$T_{eff} = |T|^2 \quad (4.5)$$

where  $T$  is defined as the power transmission coefficient, and it is different for each material.  $w_1 * w_2$  is the dimension of the defined material that covers the aperture (it could be a wooden door or a glass window etc.). When  $w_2$  is much larger, then the equation (4.2) is left with (4.4) which further reduces to (4.5) in case of free space or air when  $T_{eff} = 1$ .



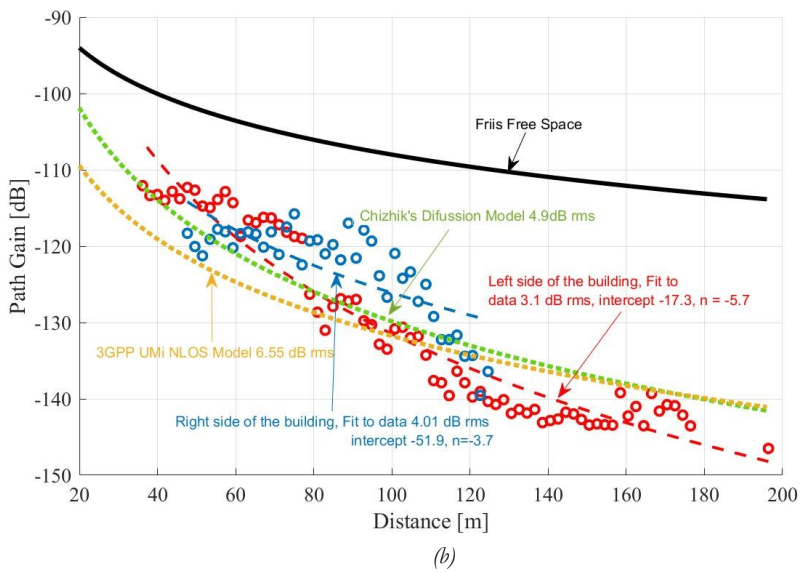
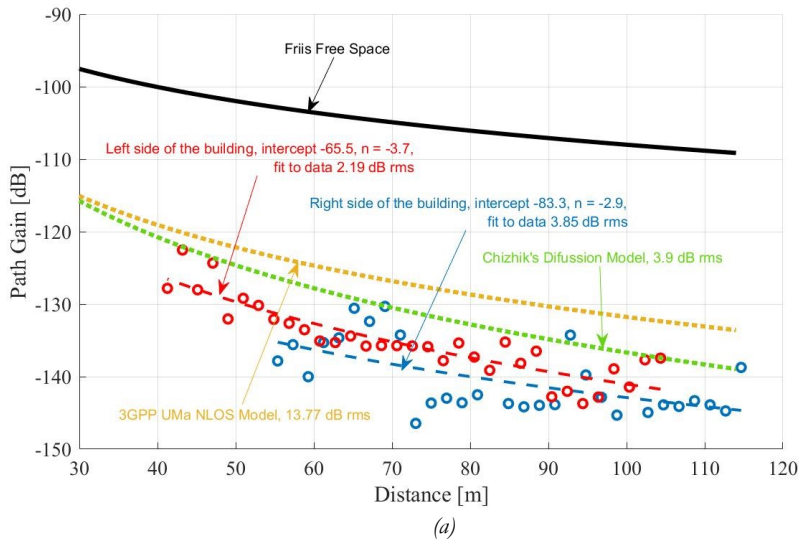
Figure 4-13 Top and front views of the external apartments. The total length of the street is 130m to the left side and 196m to the right side.

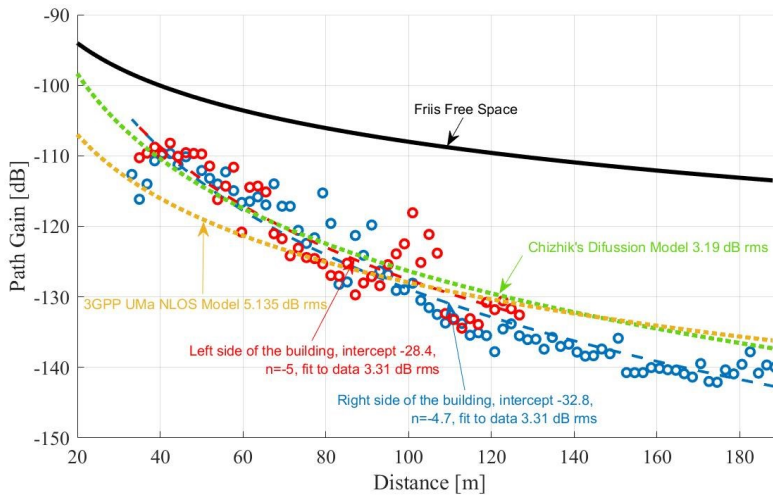


Figure 4-14 Left and right side of the view of street while looking from the balcony at 3<sup>rd</sup> floor.

### Conditions on the Day of Measurements

- It was a sunny day
- Overall altitude height difference 9m
- Mostly concrete buildings of same height (4–5 floors), some with double glass windows
- Busy road, but less traffic
- Pavement was busy as well
- Rx 1m away from railing
- Sofa, tables, and some chairs inside



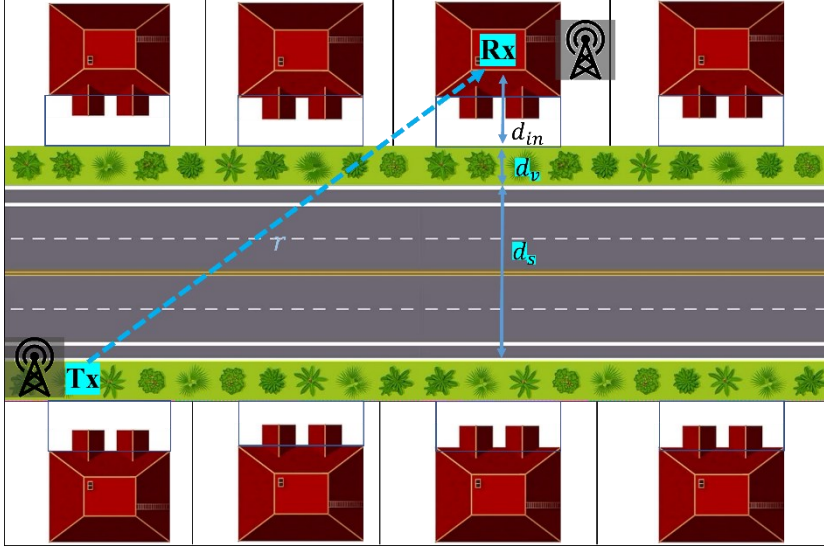


(c)

Figure 4-15 Path gain measured versus the distance for R4 and external apartments (EA): (a) Receiver is on the 4th floor of the R4 building, (b) receiver is on the 3rd floor of the EA (c) receiver is at 4<sup>th</sup> floor of EA building.

In over-the-top scenario, for both buildings when Rx is on the balcony at 4th floor, the height difference between Tx and Rx is about 9m and 13m respectively. This height difference will introduce vertical misalignment for links at short distances. For example, links that are 9m away in horizontal distance will have a vertical misalignment of 45 deg, which might be much larger than the 30-deg HPBW in elevation of the omni Tx and 10-deg HPBW in elevation of the spinning horn. So, those locations have been excluded during the analysis from the path gain. At some points, the transmitter was in LOS of the receiver because of the height difference in the street (the street was steeper on the left side of the receiver) in the case of R4.

#### 4.3.2.4 Inside Measurements



(b)

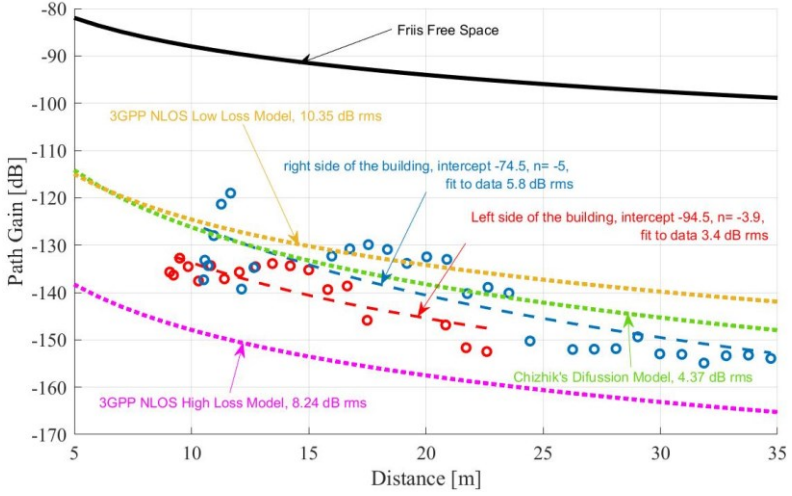
Figure 4-16 Outdoor-Indoor measurements setup scenario, Rx is placed inside the lounge and 1m away from the glass window.

In this scenario, the Rx is placed inside the apartment and 1m away from the windows, whereas the width of the balcony is  $d_{in}$ . The vertical distance between the Tx and the Rx is  $d_s$  while  $d_v$  is the vegetation depth. The average path gain for the terminal behind the foliage and inside the lounge is given by

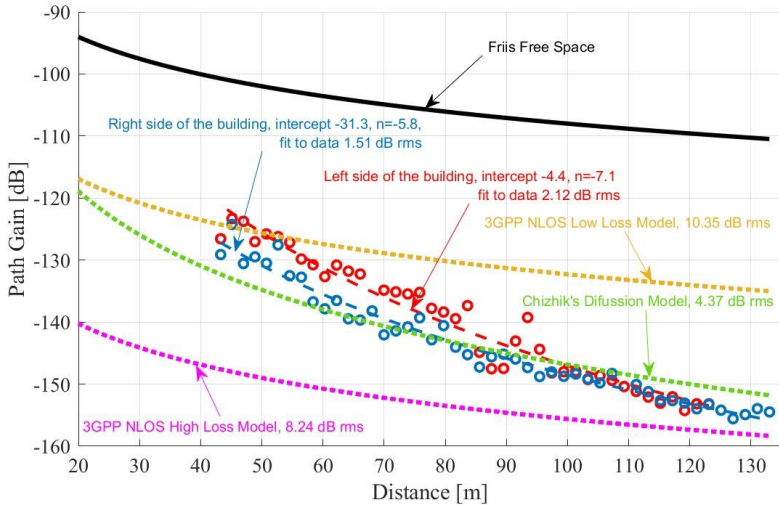
$$P_{O-I} = \frac{\lambda^2 d_p^2 e^{-K_v d_v} |T_{eff}|^2 e^{-K_{in} d_{in}}}{8\pi^2 r^4} (1 + |\gamma_g|^2) (1 + |\gamma_w|^2) \quad (4.6)$$

For inside measurements, the signals reach horn after two stages; at first, they pass through the vegetation and reach the balcony from the free space above the railing then the signals penetrate through the glass window. The foliage absorption is represented by  $K_v = 0.79$ , whereas it passes through the windows as well and the absorption through walls and other interior objects is given by  $K_{in}$  which is 0.17 in this case.  $T_{eff}$  is calculated by considering the fact that the signal passes through the vegetation and then goes above the railing to pass through the glass windows. It can be found by using the equations

(4.3) and (4.4) where the value of  $T_{eff}$  changes for both EA and R4 because of the different width of the balcony. As the indoor absorption factor adds up in the path gain, the  $T_{eff}$  is a multiplication of both  $T_{eff1}$  and  $T_{eff2}$  which are the wall penetration losses for windows (0.5 in our case) and the penetration through the balcony railing and vegetation respectively.



(a)



(b)

Figure 4-17 Outdoor-Indoor path gain versus the distance: (a) Rx is placed inside the dorm R4 on the 1st floor (b) Rx is at 4<sup>th</sup> floor of EA and inside the apartment, Rx is placed 1m away from the glass window in both cases.

Table 4-3 Root Mean Square (RMS) errors of path gain models of Athens' streets.

Location	Street parameters	Bell lab model rms Error	Data fit rms
R4 1 <sup>st</sup> Floor Balcony	$d_v = 4m,$ $d_s = 3m,$ $T_{eff} = 0.5$	5.84	Left side=0.87 Right side=3
R4 4 <sup>th</sup> Floor Balcony	$Z_{bs} = 13m,$ $Z_c = 10m,$ $T_{eff} = 0.5,$ $w = 10.5m,$ $d_{in} = 1m,$ $Z_m = 3.5$	3.9	Left side=2.19 Right side=3.85
EA 3 <sup>rd</sup> Floor Balcony	$Z_{bs} = 10m,$ $Z_c = 4.5m,$ $T_{eff} = 1,$ $d_s = 6m,$ $d_v = 1,$ $d_{in} = 1m,$ $Z_m = 3.5$	4.9	Left side=3.13 Right side=4.01
EA 4 <sup>th</sup> Floor Balcony	$Z_{bs} = 13m,$ $Z_c = 4.5m,$ $T_{eff} = 1,$ $d_s = 9m,$ $d_v = 1,$ $d_{in} = 1m,$ $Z_m = 3.5$	3.14	Left side=3 Right side=3.31
R4 1 <sup>st</sup> Floor Inside	$d_v = 2.5m,$ $d_s = 7m,$ $T_{eff} = 0.07$	3.7	Left side=3.4 Right side=5.83
EA 4 <sup>th</sup> Floor Inside	$Z_{bs} = 13m,$ $Z_c = 4.5m,$ $T_{eff} = 0.05,$ $d_s = 9m,$ $d_v = 1,$ $d_{in} = 1m,$ $Z_m = 3.5$	4.37	Left side=2.12 Right side=1.51
<b>Average</b>		4.3	3.02

Universal path gain models developed by NOKIA Bell Labs [27] have been incorporated and the rms errors of the path gain models are shown in Table 4-3. The overall rms error of the Bell Lab model is less than 5dB and the overall rms of linear fit to data is 3.02dB. The inside measurements at R4-4th floor and EA-3rd floor could not be carried out because of the huge penetration loss through double glass windows. The penetration through double glass is 40dB and through the single plain glass it is 3dB, so  $T_{\text{eff}} = 0.5$  in this case. The path loss exponent for the propagation through the vegetation for lower heights is 3 and around 1 for LOS. The path loss exponent for the NLOS for the balconies at R4 and EA is 3.5 and for the inside propagation the exponent is around 2.

#### 4.4. REFERENCES

- [1] William Lehr, Fabian Queder, Justus Haucap, “5G: A new future for Mobile Network Operators, or not?”, *Telecommunications Policy*, Volume 45, Issue 3, 2021, 102086, ISSN 0308-5961, <https://doi.org/10.1016/j.telpol.2020.102086>.
- [2] M. Series, “Guidelines for the evaluation of radio interface technologies for IMT-2020”, ITU, Report ITU-R M.2412-0 (10/2017), 2017.
- [3] Ayyaz S, Qamar U, Nawaz R (2018) HCF-CRS: A Hybrid Content based Fuzzy Conformal Recommender System for providing recommendations with confidence. *PLoS ONE* 13(10): e0204849. <https://doi.org/10.1371/journal.pone.0204849>
- [4] Mushtaq Talib et al., “Comprehensive Overview on Millimeter Wave Communications for 5G Networks Concentrating on Propagation Models for Different Urban Environments”, 3rd International Conference on Mathematics and Applied Science (ICMAS 2022), *Journal of Physics: Conf. Ser.* 2322 012095, 2022.
- [5] S. Rangan, T. S. Rappaport and E. Erkip, “Millimeter-Wave Cellular Wireless Networks: Potentials and Challenges,” in *Proceedings of the IEEE*, vol. 102, no. 3, pp. 366-385, March 2014, doi: 10.1109/JPROC.2014.2299397.
- [6] X. She, “Special Articles on LTE-Advanced Technology, Ongoing Evolution of LTE toward IMTAdvanced”, *NTT DOCOMO Technical Journal MIMO and CoMP in LTE-Advanced*, vol. 12, no. 2, pp. 20–28.
- [7] B. Krenik, “4G wireless technology: When will it happen? What does it offer?,” 2008 *IEEE Asian Solid-State Circuits Conference*, Fukuoka, Japan, 2008, pp. 141-144, doi: 10.1109/ASSCC.2008.4708715.
- [8] N. T. T. Docomo, “5G Channel Model for bands up to 100 GHz”, 5G workshops, 2015.
- [9] K. Haneda et al., “Indoor 5G 3GPP-like channel models for office and shopping mall environments,” 2016 *IEEE International Conference on Communications Workshops (ICC)*, Kuala Lumpur, Malaysia, 2016, pp. 694-699, doi: 10.1109/ICCW.2016.7503868.
- [10] S. Deng, M. K. Samimi and T. S. Rappaport, “28 GHz and 73 GHz millimeter-wave indoor propagation measurements and path loss models,” 2015 *IEEE International Conference on Communication Workshop (ICCW)*, London, UK, 2015, pp. 1244-1250, doi: 10.1109/ICCW.2015.7247348.

- [11] T. S. Rappaport and S. Deng, "73 GHz wideband millimeter-wave foliage and ground reflection measurements and models," 2015 IEEE International Conference on Communication Workshop (ICCW), London, UK, 2015, pp. 1238-1243, doi: 10.1109/ICCW.2015.7247347.
- [12] K. Haneda et al., "5G 3GPP-Like Channel Models for Outdoor Urban Microcellular and Macrocellular Environments," 2016 IEEE 83rd Vehicular Technology Conference (VTC Spring), Nanjing, China, 2016, pp. 1-7, doi: 10.1109/VTCspring.2016.7503971.
- [13] S. Nie, G. R. MacCartney, S. Sun and T. S. Rappaport, "72 GHz millimeter wave indoor measurements for wireless and backhaul communications," 2013 IEEE 24th Annual International Symposium on Personal, Indoor, and Mobile Radio Communications (PIMRC), London, UK, 2013, pp. 2429-2433, doi: 10.1109/PIMRC.2013.6666553.
- [14] K. Haneda, N. Omaki, T. Imai, L. Raschkowski, M. Peter and A. Roivainen, "Frequency-Agile Pathloss Models for Urban Street Canyons," in IEEE Transactions on Antennas and Propagation, vol. 64, no. 5, pp. 1941-1951, May 2016, doi: 10.1109/TAP.2016.2536170.
- [15] G. R. MacCartney and T. S. Rappaport, "Study on 3GPP rural macrocell path loss models for millimeter wave wireless communications," 2017 IEEE International Conference on Communications (ICC), Paris, France, 2017, pp. 1-7, doi: 10.1109/ICC.2017.7996793.
- [16] T. S. Rappaport, G. R. MacCartney, M. K. Samimi and S. Sun, "Wideband Millimeter-Wave Propagation Measurements and Channel Models for Future Wireless Communication System Design," in IEEE Transactions on Communications, vol. 63, no. 9, pp. 3029-3056, Sept. 2015, doi: 10.1109/TCOMM.2015.2434384.
- [17] S. Sun et al., "Propagation Path Loss Models for 5G Urban Micro- and Macro-Cellular Scenarios," 2016 IEEE 83rd Vehicular Technology Conference (VTC Spring), Nanjing, China, 2016, pp. 1-6, doi: 10.1109/VTCspring.2016.7504435.
- [18] S. Jaekel, L. Raschkowski, K. Börner and L. Thiele, "QuaDRiGa: A 3-D Multi-Cell Channel Model With Time Evolution for Enabling Virtual Field Trials," in IEEE Transactions on Antennas and Propagation, vol. 62, no. 6, pp. 3242-3256, June 2014, doi: 10.1109/TAP.2014.2310220.
- [19] Weiler, R.J., Peter, M., Keusgen, W. et al. Quasi-deterministic millimeter-wave channel models in MiWEBA. J Wireless Com Network 2016, 84 (2016). <https://doi.org/10.1186/s13638-016-0568-6>

- [20] A. M. Al-samman, T. A. Rahman, M. H. Azmi, and M. N. Hindia, "International Journal of Electronics and Communications ( AEÜ ) Large-scale path loss models and time dispersion in an outdoor line-of-sight environment for 5G wireless communications", *AEUE - Int. J. Electron. Commun.*, vol. 70, no. 11, pp. 1515–1521, 2016.
- [21] X. Zhao, S. Li, Q. Wang, M. Wang, S. Sun and W. Hong, "Channel Measurements, Modeling, Simulation and Validation at 32 GHz in Outdoor Microcells for 5G Radio Systems," in *IEEE Access*, vol. 5, pp. 1062-1072, 2017, doi: 10.1109/ACCESS.2017.2650261.
- [22] A. M. Al-samman, T. A. Rahman, and M. H. Azmi, "Indoor Corridor Wideband Radio Propagation Measurements and Channel Models for 5G Millimeter Wave Wireless Communications at 19 GHz , 28 GHz , and 38 GHz Bands", *Journal of wireless communications and mobile computing*, vol. 2018, 2018.
- [23] V. Erceg, S. J. Fortune, J. Ling, A. J. Rustako, and R. A. Valenzuela, "Comparisons of a computer-based propagation prediction tool with experimental data collected in urban microcellular environments," *IEEE J. Sel. Areas Commun.*, vol. 15, no. 4, pp. 677–684, May 1997.
- [24] K. Rizk, J.-F. Wagen, and F. Gardiol, "Two-dimensional ray-tracing modeling for propagation prediction in microcellular environments," *IEEE Trans. Veh. Technol.*, vol. 46, no. 2, pp. 508–518, May 1997.
- [25] Technical Specification Group Radio Access Network; Study on Channel Model for Frequencies From 0.5 to 100 GHz (Release 16), document TR 38.901 V16.1.0, 3GPP, Dec. 2019.
- [26] WINNER II Channel Models, document IST-4-027756, D1.1.2 V1.2, 2007.
- [27] D. Chizhik, J. Du and R. A. Valenzuela, "Universal Path Gain Laws for Common Wireless Communication Environments," in *IEEE Transactions on Antennas and Propagation*, vol. 70, no. 4, pp. 2928-2941, April 2022. doi: 10.1109/TAP.2021.3121173.
- [28] F. Al-Ogaili and R. M. Shubair, "Millimeter-wave mobile communications for 5G: Challenges and opportunities," 2016 IEEE International Symposium on Antennas and Propagation (APSURSI), Fajardo, PR, USA, 2016, pp. 1003-1004, doi: 10.1109/APS.2016.7696210.
- [29] T. A. Thomas, M. Rybakowski, S. Sun, T. S. Rappaport, H. Nguyen, and I. Z. Kovács, "A Prediction Study of Path Loss Models from 2-73 . 5 GHz in an Urban-Macro Environment", pp. 6–10, 2016.

- [30] S. Sun, G. R. MacCartney and T. S. Rappaport, “A novel millimeter-wave channel simulator and applications for 5G wireless communications,” 2017 IEEE International Conference on Communications (ICC), Paris, France, 2017, pp. 1-7, doi: 10.1109/ICC.2017.7996792.
- [31] J. Ryan, G. R. MacCartney and T. S. Rappaport, “Indoor office wideband penetration loss measurements at 73 GHz,” 2017 IEEE International Conference on Communications Workshops (ICC Workshops), Paris, France, 2017, pp. 228-233, doi: 10.1109/ICCW.2017.7962662.
- [32] Katsuyuki Haneda and others, “Measurement Results and Final mmMAGIC Channel Models Measurement Results and Final mmMAGIC Channel Models”, 2017.
- [33] S. Deng, G. R. MacCartney and T. S. Rappaport, “Indoor and Outdoor 5G Diffraction Measurements and Models at 10, 20, and 26 GHz,” 2016 IEEE Global Communications Conference (GLOBECOM), Washington, DC, USA, 2016, pp. 1-7, doi: 10.1109/GLOCOM.2016.7841898.
- [34] M. K. Samimi and T. S. Rappaport, “Local multipath model parameters for generating 5G millimeter-wave 3GPP-like channel impulse response,” 2016 10th European Conference on Antennas and Propagation (EuCAP), Davos, Switzerland, 2016, pp. 1-5, doi: 10.1109/EuCAP.2016.7481410.
- [35] A. Al-Shuwaili and T. M. Jamel, “5G Channel Characterization at Millimeter-Wave for Baghdad City: An NYUSIM-based Approach,” 2021 18th International Multi-Conference on Systems, Signals & Devices (SSD), Monastir, Tunisia, 2021, pp. 468-473, doi: 10.1109/SSD52085.2021.9429348.
- [36] J. G. Andrews et al., “What Will 5G Be?,” in IEEE Journal on Selected Areas in Communications, vol. 32, no. 6, pp. 1065-1082, June 2014, doi: 10.1109/JSAC.2014.2328098.
- [37] T. Report, —TR 138 901 - V14.0.0 - 5G; Study on channel model for frequencies from 0.5 to 100 GHz (3GPP TR 38.901 version 14.0.0 Release 14), vol. 0, 2017.
- [38] D. Number, P. Name, and T. I. Society, —Deliverable D1.4 METIS Channel Models, ICT-317669-METIS/D1.4 ver 3, Affiliation: ICT-317669: Mobile and wireless communications Enablers for the Twenty-twenty Information Society, 2015.
- [39] M. K. Samimi and T. S. Rappaport, “3-D statistical channel model for millimeter-wave outdoor mobile broadband communications,” 2015 IEEE International

- Conference on Communications (ICC), London, UK, 2015, pp. 2430-2436, doi: 10.1109/ICC.2015.7248689.
- [40] T. Report, —TR 138 900 - V14.2.0 - LTE; 5G; Study on channel model for frequency spectrum above 6 GHz (3GPP TR 38.900 version 14.2.0 Release 14), vol. 0, 2017.
- [41] B. T. S. Rappaport, S. Su, and S. Member, —5G Channel Model with Improved Accuracy and Efficiency in mmWave Bands, *IEEE future networks, 5G and beyond*, vol. 1, no. 1, pp. 25–26, 2017.
- [42] T. S. Rappaport, S. Sun and M. Shafi, “Investigation and Comparison of 3GPP and NYUSIM Channel Models for 5G Wireless Communications,” 2017 IEEE 86th Vehicular Technology Conference (VTC-Fall), Toronto, ON, Canada, 2017, pp. 1-5, doi: 10.1109/VTCFall.2017.8287877.
- [43] G. R. Maccartney, T. S. Rappaport, S. Sun and S. Deng, “Indoor Office Wideband Millimeter-Wave Propagation Measurements and Channel Models at 28 and 73 GHz for Ultra-Dense 5G Wireless Networks,” in *IEEE Access*, vol. 3, pp. 2388-2424, 2015, doi: 10.1109/ACCESS.2015.2486778.
- [44] S. Sun et al., “Investigation of Prediction Accuracy, Sensitivity, and Parameter Stability of Large-Scale Propagation Path Loss Models for 5G Wireless Communications,” in *IEEE Transactions on Vehicular Technology*, vol. 65, no. 5, pp. 2843-2860, May 2016, doi: 10.1109/TVT.2016.2543139.
- [45] M. K. Samimi and T. S. Rappaport, “3-D Millimeter-Wave Statistical Channel Model for 5G Wireless System Design,” in *IEEE Transactions on Microwave Theory and Techniques*, vol. 64, no. 7, pp. 2207-2225, July 2016, doi: 10.1109/TMTT.2016.2574851.
- [46] Hao Xu, T. S. Rappaport, R. J. Boyle and J. H. Schaffner, “Measurements and models for 38-GHz point-to-multipoint radiowave propagation,” in *IEEE Journal on Selected Areas in Communications*, vol. 18, no. 3, pp. 310-321, March 2000, doi: 10.1109/49.840191.
- [47] N. O. Oye and T. J. O. Afullo, “Measurements and Analysis of Large-Scale Path Loss Model at 14 and 22 GHz in Indoor Corridor,” in *IEEE Access*, vol. 6, pp. 17205-17214, 2018, doi: 10.1109/ACCESS.2018.2802038.
- [48] T. Nitsche, C. Cordeiro, A. B. Flores, E. W. Knightly, E. Perahia and J. C. Widmer, “IEEE 802.11ad: directional 60 GHz communication for multi-Gigabit-per-second Wi-Fi [Invited Paper],” in *IEEE Communications Magazine*, vol. 52, no. 12, pp. 132-141, December 2014, doi: 10.1109/MCOM.2014.6979964.

- [49] C. Cordeiro, “The pursuit of tens of gigabits per second wireless systems [Industry Perspectives],” in *IEEE Wireless Communications*, vol. 20, no. 1, pp. 3-5, February 2013, doi: 10.1109/MWC.2013.6472190.
- [50] M. H. Tariq, I. Chondroulis, P. Skartsilas, N. Babu and C. B. Papadias, “mmWave Massive MIMO Channel Measurements for Fixed Wireless and Smart City Applications”, 2020 IEEE 31st Annual International Symposium on Personal, Indoor and Mobile Radio Communications, 2020, pp. 1-6, doi: 10.1109/PIMRC48278.2020.9217375.
- [51] N. Ntetsikas et al., “60 GHz Outdoor to Indoor (O2I) Propagation Measurements in a University Campus,” 2022 IEEE 23rd International Workshop on Signal Processing Advances in Wireless Communication (SPAWC), Oulu, Finland, 2022, pp. 1-5, doi: 10.1109/SPAWC51304.2022.9833968.
- [52] C. A. L. Diakhate, J. Conrat, J. Cousin and A. Sibille, “Millimeter-wave outdoor-to-indoor channel measurements at 3, 10, 17 and 60 GHz, “ 2017 11th European Conference on Antennas and Propagation (EUCAP), 2017, pp. 1798-1802, doi: 10.23919/EuCAP.2017.7928696.
- [53] J. Lu, D. Steinbach, P. Cabrol, P. Pietraski and R. V. Pragada, “Propagation characterization of an office building in the 60 GHz band”, The 8th European Conference on Antennas and Propagation (EuCAP 2014), 2014, pp. 809-813, doi: 10.1109/EuCAP.2014.6901885.
- [54] E. Semaan, F. Harrysson, A. Furuskar and H. Asplund, “Outdoor- to-indoor coverage in high frequency bands”, 2014 IEEE Globecom Workshops (GC Wkshps), 2014, pp. 393-398, doi: 10.1109/GLOCOMW.2014.7063463.
- [55] Cheng, L., Bao, W., Liu, N., Yue, G., Zou, X., Qiu, R. C., “Study of propagation characteristics of outdoor-to-indoor channel in the 60-GHz band”, *Journal of Communications and information Networks*, 1(2), 93-101, 2016.
- [56] S. Y. Jun et al., “Penetration Loss at 60 GHz for Indoor-to-Indoor and Outdoor-to-Indoor Mobile Scenarios,” 2020 14th European Conference on Antennas and Propagation (EuCAP), Copenhagen, Denmark, 2020, pp. 1-5, doi: 10.23919/EuCAP48036.2020.9135581.
- [57] Kamboh, U.R., Ullah, U., Khalid, S. et al. Path loss modelling at 60 GHz mmWave based on cognitive 3D ray tracing algorithm in 5G. *Peer-to-Peer Netw. Appl.* 14, 3181–3197 (2021). <https://doi.org/10.1007/s12083-021-01101-w>
- [58] M. Biswal et al., “On the Characterization of Beam Misalignment in Outdoor-to-Indoor 60 GHz mmWave Channel,” 2021 15th European Conference on Antennas

- and Propagation (EuCAP), Dusseldorf, Germany, 2021, pp. 1-5, doi: 10.23919/EuCAP51087.2021.9411018.
- [59] J. Du, D. Chizhik, R. Feick, M. Rodríguez, G. Castro and R. A. Valenzuela, "Suburban Fixed Wireless Access Channel Measurements and Models at 28 GHz for 90% Outdoor Coverage," in *IEEE Transactions on Antennas and Propagation*, vol. 68, no. 1, pp. 411-420, Jan. 2020, doi: 10.1109/TAP.2019.2935110.
- [60] D. Chizhik, J. Du, R. Feick, M. Rodríguez, G. Castro and R. A. Valenzuela, "Path Loss and Directional Gain Measurements at 28 GHz for Non-Line-of-Sight Coverage of Indoors With Corridors," in *IEEE Transactions on Antennas and Propagation*, vol. 68, no. 6, pp. 4820-4830, June 2020, doi: 10.1109/TAP.2020.2972609.
- [61] Study on channel model for frequencies from 0.5 to 100 GHz. 3rd Generation Partnership Project (3GPP), Tech. Rep., 38. 3GPP 2020.
- [62] Montgomery, D. C., & Runger, G. C., "Applied statistics and probability for engineers", John Wiley & Sons, 2010.
- [63] L. J. Greenstein, S. S. Ghassemzadeh, V. Erceg and D. G. Michelson, "Ricean  $\mathcal{K}$ -Factors in Narrow-Band Fixed Wireless Channels: Theory, Experiments, and Statistical Models," in *IEEE Transactions on Vehicular Technology*, vol. 58, no. 8, pp. 4000-4012, Oct. 2009, doi: 10.1109/TVT.2009.2018549.
- [64] A. M. Al-Samman, T. A. Rahman, M. H. Azmi, A. Sharaf, Y. Yamada and A. Alhammadi, "Path loss model in indoor environment at 40 GHz for 5G wireless network," 2018 IEEE 14th International Colloquium on Signal Processing & Its Applications (CSPA), Penang, Malaysia, 2018, pp. 7-12, doi: 10.1109/CSPA.2018.8368676.
- [65] T. S. Rappaport, J. N. Murdock and F. Gutierrez, "State of the Art in 60-GHz Integrated Circuits and Systems for Wireless Communications," in *Proceedings of the IEEE*, vol. 99, no. 8, pp. 1390-1436, Aug. 2011, doi: 10.1109/JPROC.2011.2143650.

## CHAPTER 5. EXPERIMENTS AND PROOF OF CONCEPT DEMOS

MAMP prototype is developed and after the measurements at an anechoic chamber, it was integrated in different projects to show the proof of concept and demonstration. The MAMP antenna is tested for both the Wi-Fi and the backhauling to see the performance by integrating it in already developed applications.

1. FIREMAN project (for access link)
2. 5G/4G backhaul setup using USRPs (for backhauling)

### 5.1. FIREMAN SETUP

FIREMAN (Framework for the Identification of Rare Events via MACHine learning and IoT Networks) is a European research project funded under the CHIST-ERA scheme.

An IoT based data collection platform is developed at the SWiFT Lab, where IoT sensors are connected with a data collection hub (access point) and the transmitted power at these sensor nodes can be controlled using a graphical user interface (GUI). This GUI also enabled us to send commands and receive data from sensors. The objective of this project is to increase the battery life of the sensor nodes by connecting them with the pointed or directional beams, which increases the gain in a particular direction and thus reducing the transmission power at the sensor nodes. The setup of the project demonstration is presented in Figure 5-1.

The platform uses several Raspberry pi's (numbered as P1 to P7 in the figure) as sensor nodes which are placed at random positions within the lab to showcase the industry environment. A TP link (access point AP) device with replaceable antennas is used as an access point. The GUI is developed to interact with the communication setup between the sensors and the AP. It can change the transmission power at the nodes depending upon the requirements to save the battery of the respective transmitting node. The AP is equipped with the MAMP antenna, and it is steered manually directing its beam towards the transmitting sensors already placed in different directions to evaluate the performance of the antenna array.

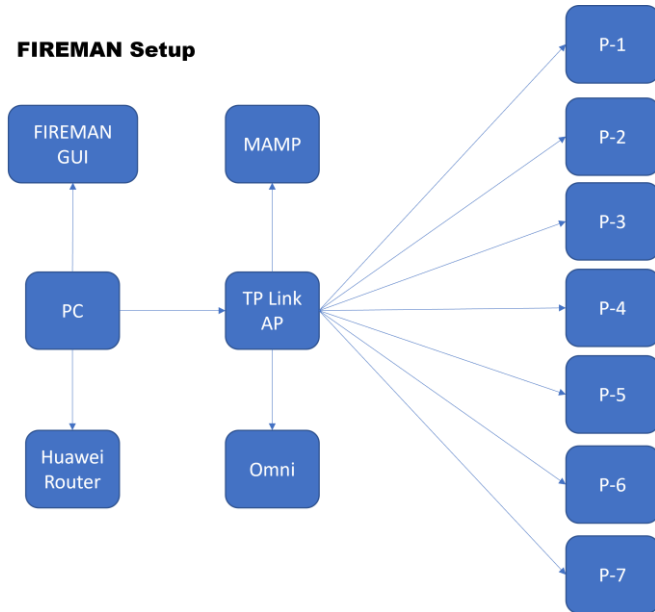


Figure 5-1 FIREMAN setup.

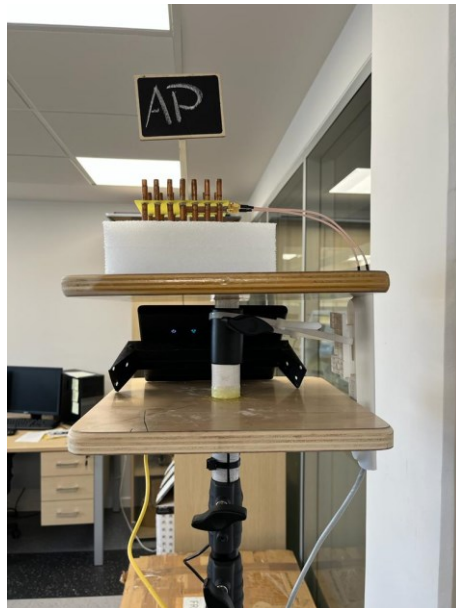


Figure 5-2 Access point omni antennas replaced with MAMP antenna array.

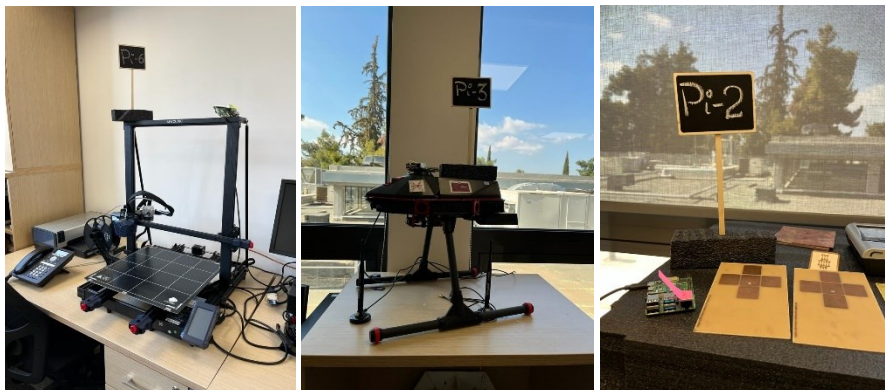


Figure 5-3 Positions of the Raspberry Pi's in the SWiFT Lab.

Figures 5-2 and 5-3 show the MAMP antenna integrated with the AP and the positions of the nodes. Status of all the connected nodes can be seen in Figure 5-4, where a GUI displays the temperature and the transmission power of the respective node. Experiments consist of the examples depending upon the transmitted power of the sensors which is initially set by the user, so as to see the difference and the performance of the MAMP in a particular direction (keeping in mind the radiation pattern of the MAMP antenna array). Figure 5-4 shows the circuit temperature and also the power being transmitted by each Pi board.

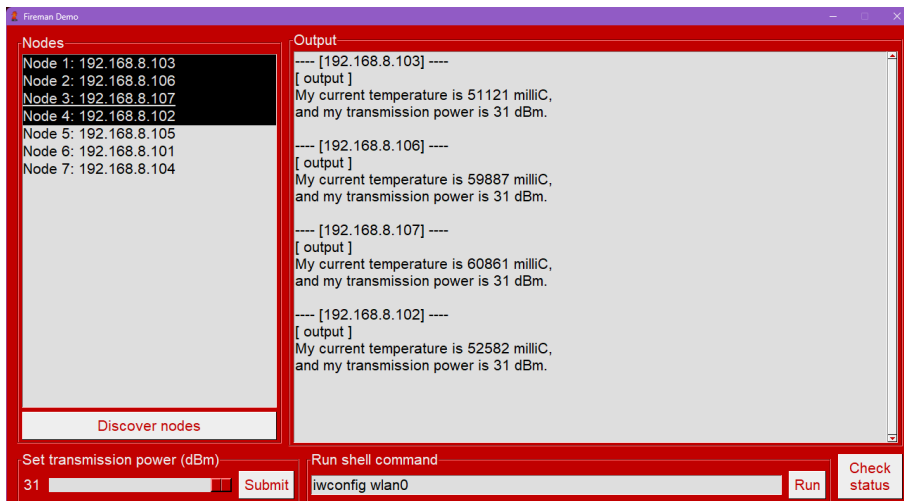


Figure 5-4 GUI which shows the connected sensor nodes, displaying the respective temperatures and the transmission powers.

PROPAGATION MEASUREMENTS AND CHANNEL MODELING

ID	Hostname	IP Address	MAC Address	Band	SSID	Active Time	Up (Byte)	Down (Byte)	RSSI (dBm)	Rate (Mbps)	Action
1	fireman-pl4	192.168.8.103	E4-5F-01-B0-18-CA	2.4GHz	Fireman	0 days 01:02:13	331k	37k	-40	72.2	 
2	fireman-pl5	192.168.8.110	E4-5F-01-B0-19-15	2.4GHz	Fireman	0 days 01:02:13	325k	35k	-41	71.9	 
3	fireman-pl1	192.168.8.105	E4-5F-01-B0-19-09	2.4GHz	Fireman	0 days 00:53:23	254k	35k	-35	72.2	 
4	fireman-pl3	192.168.8.106	E4-5F-01-27-67-45	2.4GHz	Fireman	0 days 00:53:03	251k	35k	-43	72.2	 
5	fireman-pl7	192.168.8.107	E4-5F-01-B0-19-05	2.4GHz	Fireman	0 days 00:51:43	244k	35k	-41	72.2	 
6	fireman-pl2	192.168.8.108	E4-5F-01-56-5F-D0	2.4GHz	Fireman	0 days 00:48:53	226k	37k	-37	72.2	 
7	fireman-pl6	192.168.8.109	E4-5F-01-B0-19-0C	2.4GHz	Fireman	0 days 00:47:13	210k	35k	-38	71.9	 

(a)

ID	Hostname	IP Address	MAC Address	Band	SSID	Active Time	Up (Byte)	Down (Byte)	RSSI (dBm)	Rate (Mbps)	Action
1	fireman-pl4	192.168.8.103	E4-5F-01-B0-18-CA	2.4GHz	Fireman	0 days 01:20:36	362k	38k	-39	72.2	 
2	fireman-pl5	192.168.8.110	E4-5F-01-B0-19-15	2.4GHz	Fireman	0 days 01:20:36	356k	36k	-30	72.1	 
3	fireman-pl1	192.168.8.105	E4-5F-01-B0-19-09	2.4GHz	Fireman	0 days 01:11:46	283k	35k	-35	72.2	 
4	fireman-pl3	192.168.8.106	E4-5F-01-27-67-45	2.4GHz	Fireman	0 days 01:11:26	282k	35k	-34	72.2	 
5	fireman-pl7	192.168.8.107	E4-5F-01-B0-19-05	2.4GHz	Fireman	0 days 01:10:06	274k	35k	-35	72.2	 
6	fireman-pl2	192.168.8.108	E4-5F-01-56-5F-D0	2.4GHz	Fireman	0 days 01:07:16	256k	37k	-39	72.2	 
7	fireman-pl6	192.168.8.109	E4-5F-01-B0-19-0C	2.4GHz	Fireman	0 days 01:05:36	239k	35k	-36	71.9	 

(b)

Figure 5-5 Received signal strength at the access point using MAMP antenna array: (a) the MAMP was directed towards Pi-2 (b) MAMP array was directed towards Pi-5.

Application to an IoT setup for manufacturing or an agriculture platform can be considered, where a data collection hub is integrated with the MAMP antenna array. This IoT platform consists of sensor nodes collecting data from the environmental sensors i.e., temperature, humidity, moisture etc. These sensors are sending data to Pi boards and the data is transmitted to the data collection hub as can be seen in figure 5-1. Battery life at the transmitter nodes or sensors can be increased by reducing the transmitter power at each node. The transmitter with reduced transmit power can connect to a receiver with a reliable link only if the receiver gain is large enough and it has a pointing beam towards the direction of the transmitter. A pointed beam with higher gain can be achieved using multiple antennas, which increases the power usage at the receiver unit and also increases

the hardware complexity. So, a suitable solution is to use MAMPs with reduced number of RF chains and get a beam with high gain and narrow beamwidth. For the proof of concept, a MAMP (referred to design in chapter 3) with 2 active and 12 parasitic elements is used for the above-mentioned setup. The MAMP array is intentionally designed for 2 active ports to be used for the setups available in the lab.

The prototyped MAMP antenna is integrated in the access point to evaluate the performance of the antenna array. The screenshots in figure 5-5 show the RSSI at the access point where MAMP is integrated. Our prototyped MAMP array generates a beam of 40 degrees beamwidth and a gain of 7dBi. It was directed manually towards each transmitting node to evaluate the RSSI. When the array was directing towards Pi-2, the RSSI was -37dBm. It can be seen that, among all the transmitting nodes, Pi-2 was using the lowest power to transmit the data because of the additive gain from the receiver. The experiment was repeated for Pi-5, when MAMP was pointing towards Pi-5, the RSSI was -30dBm. The RSSI at all other transmitting nodes is higher than the power transmitted by Pi-5, thereby proving the fact that the energy can be saved at sensor nodes by using a directional antenna at the receiver with higher gains.

## **5.2. ANTENNA PERFORMANCE USING USRPS**

### **5.2.1. ANTENNA PERFORMANCE FOR 4G SETUP**

4G over the air setup is considered to evaluate the backhaul performance of MAMP antenna array. At first, a reliability test was conducted by transmitting data at different speeds by analyzing the packet error loss over the channel. Later, some power measurements were performed using the USRPs integrated with SDR angel software.

The setup consists of USRPs which are configured to provide a 4G network. The MAMP antenna was connected to a 4G eNodeB transmitting on Band 1 (2650MHz), running in SISO mode. On the Tx port, the MAMP antenna was connected with the help of a power splitter. On the Rx port, an omnidirectional antenna was used to help establish the connection between the UE and the eNodeB.

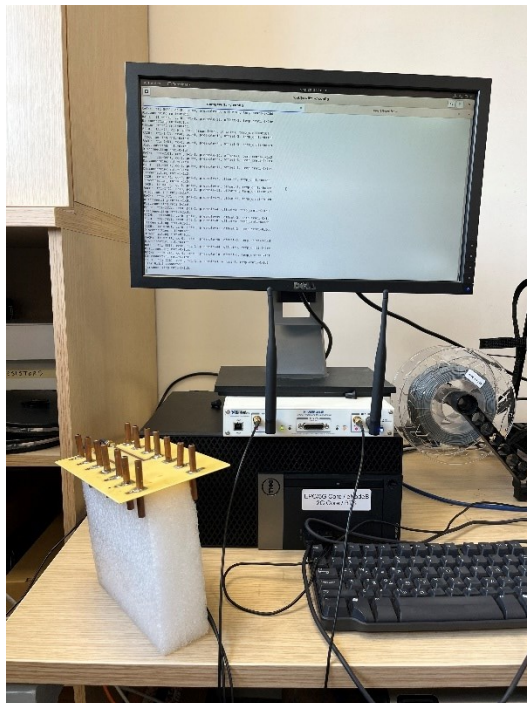


Figure 5-6 MAMP antenna connected to eNodeB (transmitter unit). The srsRAN eNodeB server debug log is visible in the background.

## Data Rate Measurements Using 4G Setup

### 5MBPS

Connecting to host 10.45.0.1, port 5201

[ 5] local 10.45.0.7 port 60339 connected to 10.45.0.1 port 5201

[ ID]	Interval	Transfer	Bitrate	Total Datagrams
[ 5]	0.00-1.00 sec	611 KBytes	5.00 Mb/s	464
[ 5]	1.00-2.00 sec	609 KBytes	4.99 Mb/s	463
[ 5]	2.00-3.00 sec	611 KBytes	5.00 Mb/s	464
[ 5]	3.00-4.00 sec	611 KBytes	5.00 Mb/s	464
[ 5]	4.00-5.00 sec	609 KBytes	4.99 Mb/s	463
[ 5]	5.00-6.00 sec	611 KBytes	5.00 Mb/s	464
[ 5]	6.00-7.00 sec	611 KBytes	5.00 Mb/s	464
[ 5]	7.00-8.00 sec	609 KBytes	4.99 Mb/s	463
[ 5]	8.00-9.00 sec	611 KBytes	5.00 Mb/s	464
[ 5]	9.00-10.00 sec	611 KBytes	5.00 Mb/s	464

-----

[ ID]	Interval	Transfer	Bitrate	Jitter	Lost/Total Datagrams
[ 5]	0.00-10.00 sec	5.96 MBytes	5.00 Mb/s	0.000 ms	0/4637 (0%) sender

[ 5] 0.00-10.03 sec 4.67 MBytes 3.90 Mbits/sec 3.093 ms 1008/4637 (22%) receiver iperf Done.

## 10MBPS

Connecting to host 10.45.0.1, port 5201

[ 5] local 10.45.0.6 port 56559 connected to 10.45.0.1 port 5201

[ ID]	Interval	Transfer	Bitrate	Total Datagrams
[ 5]	0.00-1.00 sec	1.19 MBytes	10.0 Mbits/sec	927
[ 5]	1.00-2.00 sec	1.19 MBytes	10.0 Mbits/sec	927
[ 5]	2.00-3.00 sec	1.19 MBytes	10.0 Mbits/sec	928
[ 5]	3.00-4.00 sec	1.19 MBytes	10.0 Mbits/sec	927
[ 5]	4.00-5.00 sec	1.19 MBytes	10.0 Mbits/sec	927
[ 5]	5.00-6.00 sec	1.19 MBytes	10.0 Mbits/sec	927
[ 5]	6.00-7.00 sec	1.19 MBytes	10.0 Mbits/sec	928
[ 5]	7.00-8.00 sec	1.19 MBytes	10.0 Mbits/sec	927
[ 5]	8.00-9.00 sec	1.19 MBytes	10.0 Mbits/sec	927
[ 5]	9.00-10.00 sec	1.19 MBytes	10.0 Mbits/sec	928

[ ID]	Interval	Transfer	Bitrate	Jitter	Lost/Total Datagrams
[ 5]	0.00-10.00 sec	11.9 MBytes	10.0 Mbits/sec	0.000 ms	0/9273 (0%) sender
[ 5]	0.00-10.02 sec	10.4 MBytes	8.70 Mbits/sec	0.808 ms	1186/9273 (13%) receiver iperf Done.

## 15MBPS

Connecting to host 10.45.0.1, port 5201

[ 5] local 10.45.0.7 port 38016 connected to 10.45.0.1 port 5201

[ ID]	Interval	Transfer	Bitrate	Total Datagrams
[ 5]	0.00-1.00 sec	1.79 MBytes	15.0 Mbits/sec	1390
[ 5]	1.00-2.00 sec	1.79 MBytes	15.0 Mbits/sec	1391
[ 5]	2.00-3.00 sec	1.79 MBytes	15.0 Mbits/sec	1391
[ 5]	3.00-4.00 sec	1.79 MBytes	15.0 Mbits/sec	1391
[ 5]	4.00-5.00 sec	1.79 MBytes	15.0 Mbits/sec	1391
[ 5]	5.00-6.00 sec	1.79 MBytes	15.0 Mbits/sec	1391
[ 5]	6.00-7.00 sec	1.79 MBytes	15.0 Mbits/sec	1391
[ 5]	7.00-8.00 sec	1.79 MBytes	15.0 Mbits/sec	1391
[ 5]	8.00-9.00 sec	1.79 MBytes	15.0 Mbits/sec	1391
[ 5]	9.00-10.00 sec	1.79 MBytes	15.0 Mbits/sec	1391

[ ID]	Interval	Transfer	Bitrate	Jitter	Lost/Total Datagrams
[ 5]	0.00-10.00 sec	17.9 MBytes	15.0 Mbits/sec	0.000 ms	0/13909 (0%) sender
[ 5]	0.00-10.02 sec	16.5 MBytes	13.8 Mbits/sec	0.962 ms	1065/13909 (7.7%) receiver iperf Done.

## 20MBPS

Connecting to host 10.45.0.1, port 5201

[ 5] local 10.45.0.7 port 38687 connected to 10.45.0.1 port 5201

```

[ ID] Interval      Transfer  Bitrate    Total Datagrams
[ 5] 0.00-1.00 sec 2.38 MBytes 20.0 Mbits/sec 1853
[ 5] 1.00-2.00 sec 2.38 MBytes 20.0 Mbits/sec 1855
[ 5] 2.00-3.00 sec 2.38 MBytes 20.0 Mbits/sec 1855
[ 5] 3.00-4.00 sec 2.38 MBytes 20.0 Mbits/sec 1854
[ 5] 4.00-5.00 sec 2.38 MBytes 20.0 Mbits/sec 1855
[ 5] 5.00-6.00 sec 2.38 MBytes 20.0 Mbits/sec 1854
[ 5] 6.00-7.00 sec 2.38 MBytes 20.0 Mbits/sec 1855
[ 5] 7.00-8.00 sec 2.38 MBytes 20.0 Mbits/sec 1855
[ 5] 8.00-9.00 sec 2.38 MBytes 20.0 Mbits/sec 1854
[ 5] 9.00-10.00 sec 2.38 MBytes 20.0 Mbits/sec 1855
-----
[ ID] Interval      Transfer  Bitrate    Jitter  Lost/Total Datagrams
[ 5] 0.00-10.00 sec 23.8 MBytes 20.0 Mbits/sec 0.000 ms 0/18545 (0%) sender
[ 5] 0.00-11.88 sec 19.4 MBytes 13.7 Mbits/sec 0.828 ms 3351/18427 (18%) receiver

```

*iperf Done.*

## 25MBPS

*Connecting to host 10.45.0.1, port 5201*

```

[ 5] local 10.45.0.7 port 43139 connected to 10.45.0.1 port 5201
[ ID] Interval      Transfer  Bitrate    Total Datagrams
[ 5] 0.00-1.00 sec 2.98 MBytes 25.0 Mbits/sec 2317
[ 5] 1.00-2.00 sec 2.98 MBytes 25.0 Mbits/sec 2318
[ 5] 2.00-3.00 sec 2.98 MBytes 25.0 Mbits/sec 2318
[ 5] 3.00-4.00 sec 2.98 MBytes 25.0 Mbits/sec 2318
[ 5] 4.00-5.00 sec 2.98 MBytes 25.0 Mbits/sec 2319
[ 5] 5.00-6.00 sec 2.98 MBytes 25.0 Mbits/sec 2318
[ 5] 6.00-7.00 sec 2.98 MBytes 25.0 Mbits/sec 2318
[ 5] 7.00-8.00 sec 2.98 MBytes 25.0 Mbits/sec 2318
[ 5] 8.00-9.00 sec 2.98 MBytes 25.0 Mbits/sec 2319
[ 5] 9.00-10.00 sec 2.98 MBytes 25.0 Mbits/sec 2318
-----
[ ID] Interval      Transfer  Bitrate    Jitter  Lost/Total Datagrams
[ 5] 0.00-10.00 sec 29.8 MBytes 25.0 Mbits/sec 0.000 ms 0/23181 (0%) sender
[ 5] 0.00-10.13 sec 21.5 MBytes 17.8 Mbits/sec 0.470 ms 6478/23179 (28%) receiver
iperf Done.

```

Some screenshots are presented above from the data rates' measurements that were carried out using USRPs available in the lab based on the 4G setup. From the data above it can be seen that even 25 Megabits of data can be transmitted over the channel using the prototyped MAMP with a packet loss of only 28%. 15 Mbps can be transmitted with a packet loss of 7.7%. On the other end, a HUAWEI B315 LTE router with an omnidirectional antenna was connected to another computer. Bandwidth and percentage packet error loss tests were performed with the help of the iperf3 utility. The iperf3 server is operating at the eNodeB whereas at the UE side, the iperf3 client is running with UDP

in reverse direction so that the metrics could be seen at the server. Figure 5-5 shows the iperf server with eNodeB, where the MAMP antenna is integrated. The receiver is connected to the omni antenna with the USRP receiver unit.

### 5.2.2. ANTENNA PERFORMANCE BASED ON POWER MEASUREMENTS

A comparison of received power using a MAMP antenna array and an Omni antenna is shown in the setup below. The setup consists of a transmitter and a receiver integrated with SDRangel software. A QPSK DVB-S signal was transmitted using an Omni antenna at two different frequencies i.e., 2.4GHz and 2.6GHz to see the received power at the receiver. An Omni antenna is connected to USRP B210 to receive the transmitted signal and the received power is shown in Figure 5-7. The measurements were carried at 2.6GHz because 2.4GHz is not supported in Europe for 4G/5G communications and the available SDRs do not support this band, but this antenna array was built at 2.4GHz so the performance is shown at the designed frequency and at 2.6GHz where MAMP is performing better but with lower efficiency because of the mismatch.

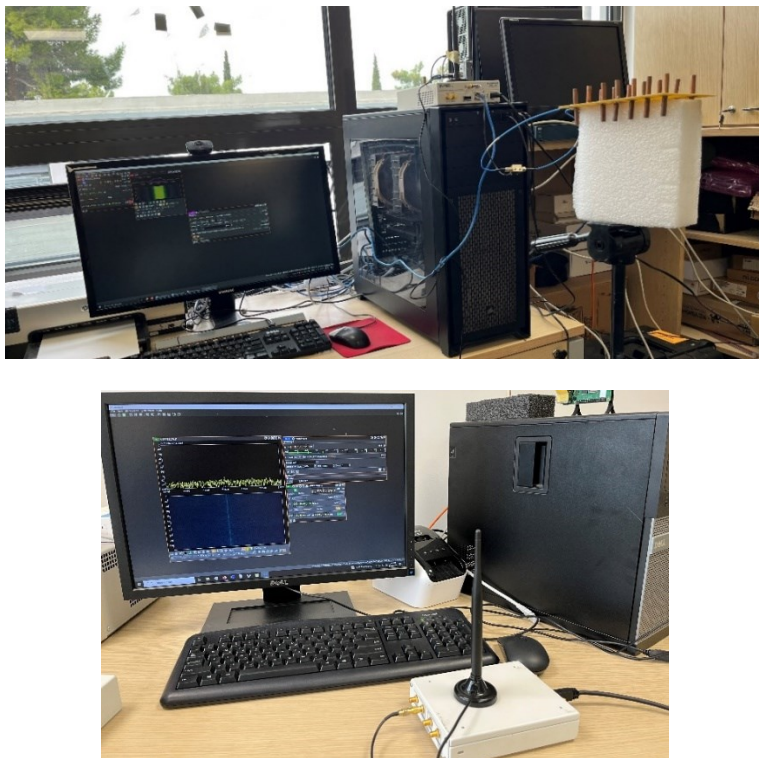
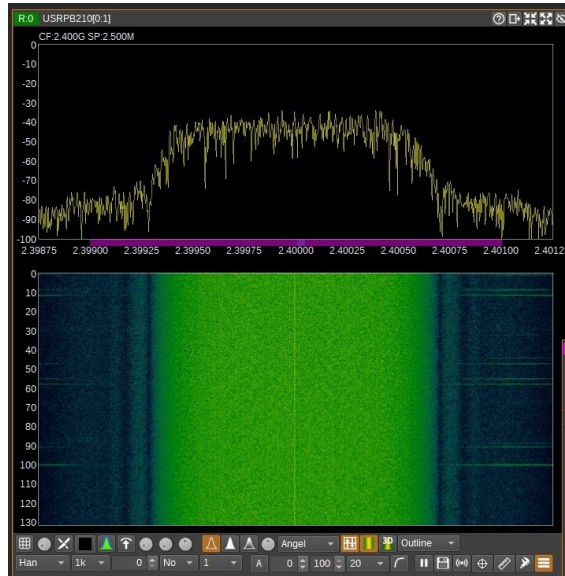
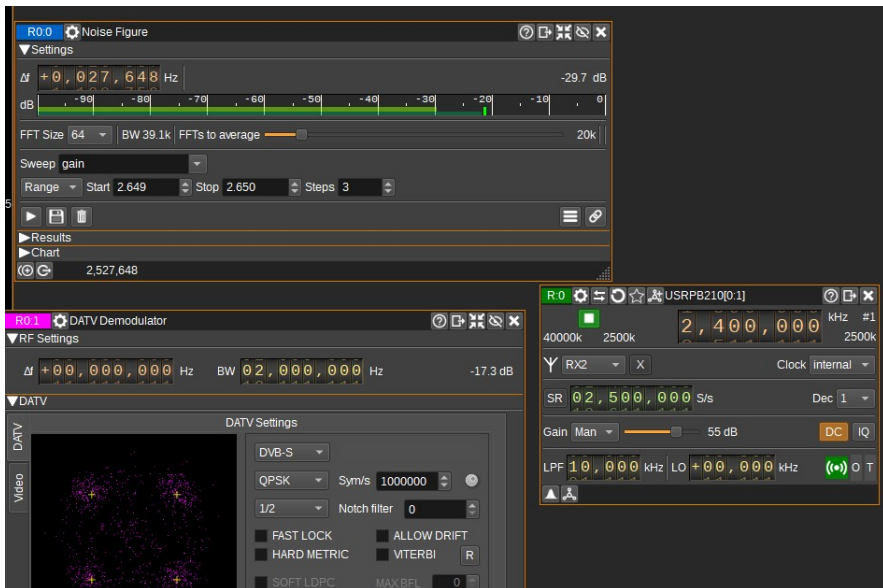


Figure 5-7 Transmitter-Receiver setup for the power measurements using SDRangel.

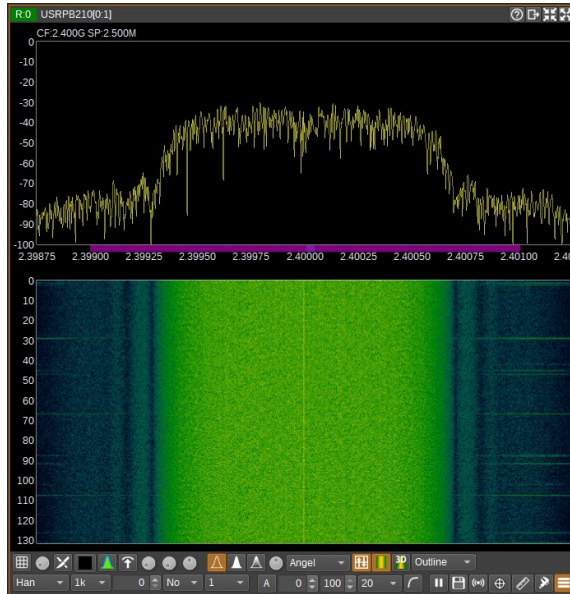
PROPAGATION MEASUREMENTS AND CHANNEL MODELING



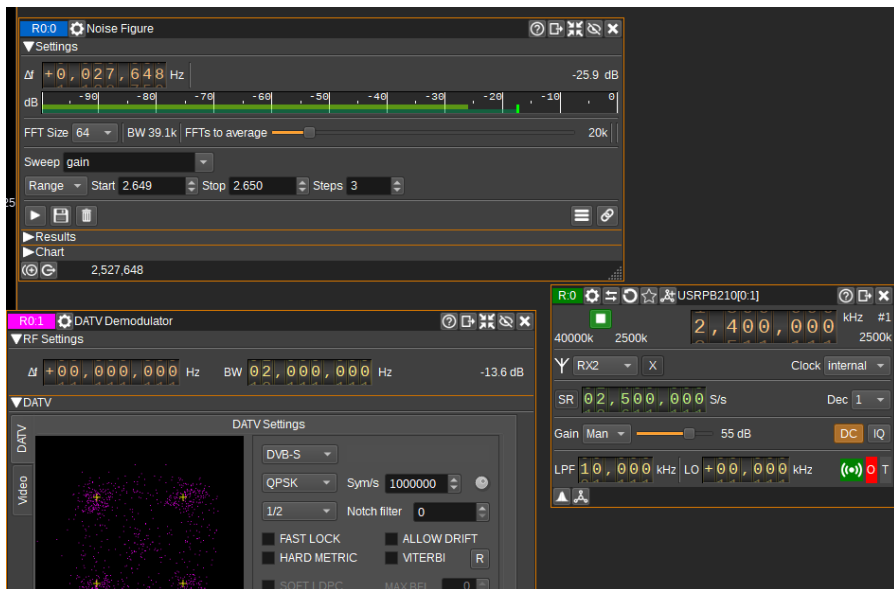
(a)



(b)



(c)

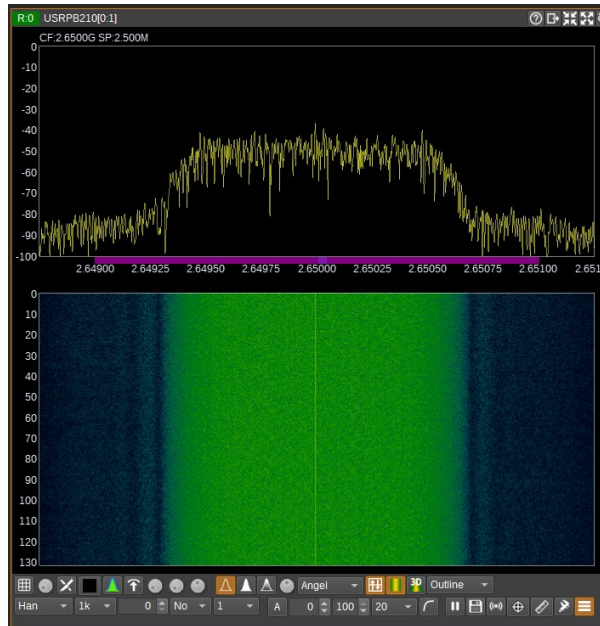


(d)

Figure 5-8 Received power at the USRP b210 using SDRAngel software when both transmitter and the receiver are tuned at 2.4GHz frequency; (a) spectrum of the DVB-S transmitting channel

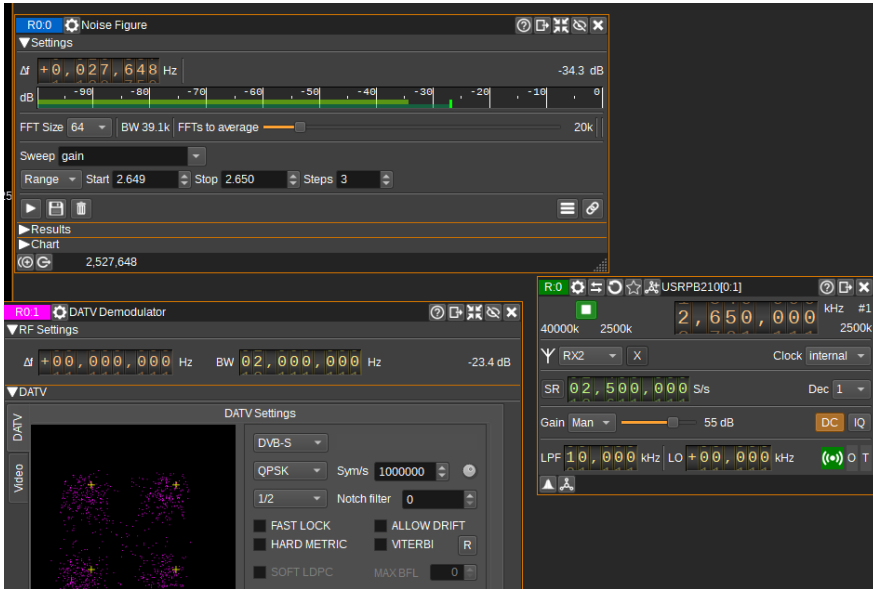
at 2.4GHz when omni antenna is transmitting (b) received power and the constellation when an omni antenna is transmitting (c) spectrum of the DVB-S transmitting channel at 2.4GHz when MAMP antenna is transmitting (d) received power and constellation is shown when MAMP antenna is transmitting

According to the setup, at first an omni antenna was integrated with the transmitting USRP unit. It is configured to transmit a DVB-S type signal using SDRangel software at both frequencies i.e., 2.4GHz and 2.6GHz. The receiver USRP unit is integrated with an omni antenna and is configured at the same frequency. Both the transmitter and receiver units are placed at a distance of 3m from each other inside the lab. Received power is measured across this distance and a comparison is shown. -29.7dB power is received when an Omni antenna is transmitting to an Omni receiver, whereas, when the MAMP is integrated, the received power increases to -25.9dB, which is due to the enhanced additive gain of the array.

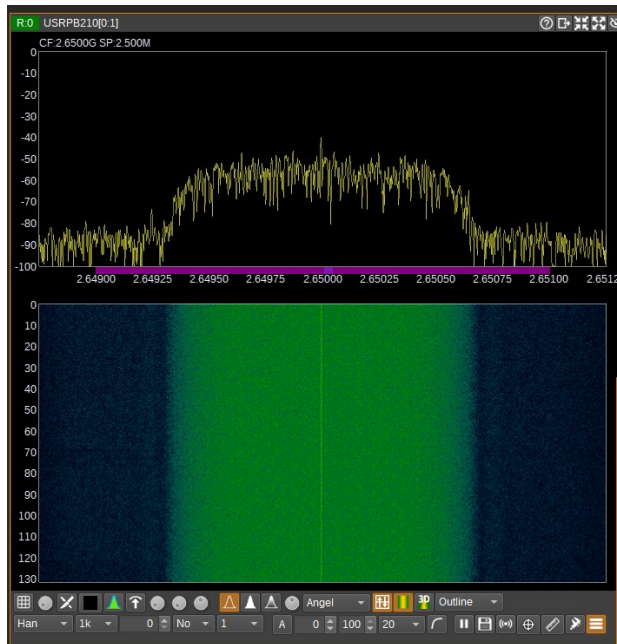


(a)

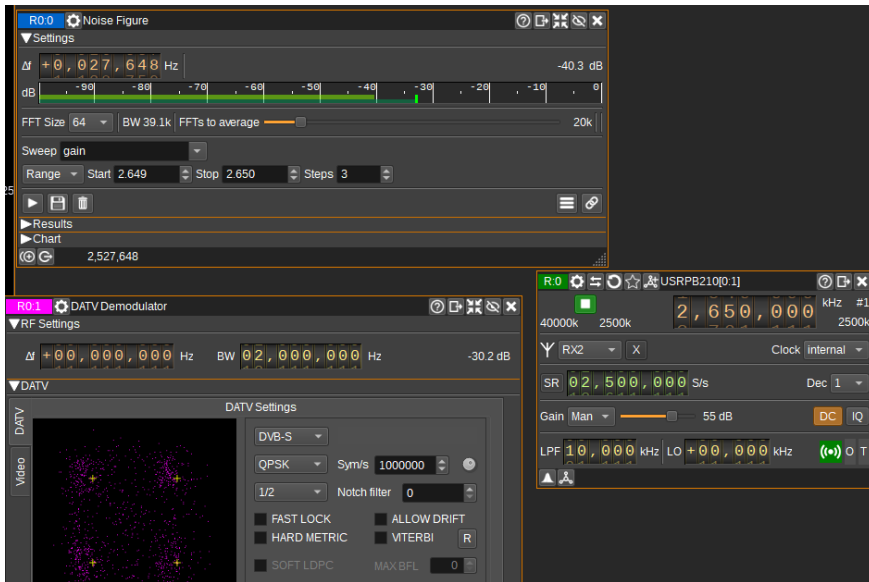
PROPAGATION MEASUREMENTS AND CHANNEL MODELING



(b)



(c)



(d)

Figure 5-9 Received power at the USRP b210 using SDRAngel software when both transmitter and the receiver are tuned at 2.4GHz frequency; (a) spectrum of the DVB-S transmitting channel at 2.4GHz when omni antenna is transmitting (b) received power and the constellation when an omni antenna is transmitting (c) spectrum of the DVB-S transmitting channel at 2.4GHz when MAMP antenna is transmitting (d) received power and constellation is shown when MAMP antenna is transmitting

Later, the setup is configured to transmit a DVB-S type signal using SDRangel software at both frequencies i.e., 2.4GHz and 2.6GHz. The above experiment is performed again with both omni and MAMP at the transmitting unit. -34.3dB power is received when the MAMP antenna is transmitting to an Omni receiver, whereas when the Omni is integrated, the received power decreases to -40dB.

The difference between the received powers of an Omni and the MAMP is around 5dB, which clearly shows that the MAMP antenna array is radiating well at the operating frequency of 2.4GHz and from the constellation it can be seen that it performs very well at this channel. The received power is lower when a signal is transmitted at 2.6GHz because the efficiency of the MAMP at 2.6GHz is lower (around 90%) and also the peak gain is around 7dB, which is lower compared to the gain and efficiency at 2.4GHz which is 8dB and 98% respectively. Another reason is the mismatch at 2.6GHz which causes loss of radiated power at the given frequency.

## CHAPTER 6. CONCLUSIONS AND FUTURE WORK

The overall MAMP performance is good, and it is well matched and performing well at the designed frequency. So, it is a good candidate for the future mMIMO communications for 5G and beyond, where small cells or self-backhauled wireless communications will be deployed. The size, weight, and cost of the wireless communications can be reduced by reducing the number of RF chains. Narrow beams can be achieved by introducing more numbers of active elements and thus the parasitic elements.

Design Guidelines are developed for Multi-Active/Multi-Passive Parasitic Antenna Arrays which introduce radiation conditions (chapter-2) to ensure that the MAMP array radiates. As per these developed guidelines, all the elements of the MAMP arrays will either radiate as whole or some of the elements will radiate. The radiation conditions are integrated in an algorithm (AOSBA) to compute the loads which are used in a CST simulation software to showcase with examples. Examples show that even if an array has a comparable desired array beam to an ideal beam, there might be a possibility that the array as a whole will not radiate, due to the negative input impedance at any feeding port of the array. The input impedance can be negative due to the mutual coupling among the elements and the distance among the elements. A mutual coupling model for the multi-active multi-passive antenna array is required to accurately model the design and important parameters for a desired output beam.

The newly developed radiation conditions are integrated with SBA to compute the load values for the parasitic elements. To ensure the MAMP array performance, a new cost function is introduced into the existing SBA algorithm. Radiation efficiency is calculated using the newly developed equations in chapter-3, by incorporating the mutual coupling among the elements. A new cost function is developed incorporating the radiation efficiency and the difference of radiation patterns between an ideal ULA and proposed MAMP. Hybrid beamforming is achieved using multi-active multi-passive parasitic antenna arrays. Some examples are shown for different steering angles, for example, the beam is directed towards 600, 900 and 1200. The algorithm computes the reactive load values only, which are easy to implement and also in a range that is available in the market. Mismatch for different angles can be eliminated using different combination of load values. Better performance can be achieved using MAMP array than conventional ULA by reducing the number of RF chains thus with reduced hardware complexity and cost of the system. SBA computes the load values for the same weights at the active ports. 2 active 12 passive MAMP is designed and developed to show the proof of concept. It is measured using a network analyzer and in anechoic chamber. Simulated and measured results are in good match.

A MAMP with higher number of active and parasitic elements can provide even better performance which is targeted for future work. A MAMP will be designed for MIMO communications with at least 4 active elements. To get the realistic weights and load values that can satisfy the MIMO system requirements will be a challenge. Since the parasitic elements need to be placed in the close vicinity of active elements to get increased coupling, the distance among the elements plays a crucial role here. For a narrower beam, a greater number of elements are needed and thus the size increases. Considering the future wireless technologies, designing MAMP array for mmWaves will be a challenge. At such higher frequencies, the size of the elements is small but the distance among the elements becomes a limitation due to the shorter wavelengths. Design and development of MAMP for mmWave communication and the analysis of near field can be considered as a key focus in the future. Another future aspect of this project is to design MAMPs using machine learning techniques for the computation of tunable loads instead of using constraint-based optimization. That would require mutual coupling models for MAMPs to directly solve the load values and get the currents at each element.

To see the practical limitations and real time performance of the envisioned self-backhaul base stations, mmWave measurements were performed. Three successful measurement campaigns were carried out in Athens for high frequency channel i.e., 60GHz. The measurements are based on outdoor-outdoor, outdoor-indoor and indoor scenarios. The locations are inside and outside ACG campus and in a commercial plaza located in Athens, Greece. An omni transmitter was mounted on a lamp post at a certain height and the receiver unit was placed inside the building or office. Channels were measured across the glass window and vegetation. The channel measurements were performed using channel sounding equipment which was provided by Facebook (now Meta) under the TIP project and another pair of equipment by Nokia Bell Labs US. Measurement data was analyzed and presented with the linear data fits, and a comparison was given between Frii's free space and Chizik's Bell Labs channel models. Based on these channel measurements, a channel model is developed for future fixed wireless communications using "street furniture."

The developed MAMP antenna array is used to show the proof of concept by using it for different applications. The prototype is used in the applications available in the Smart Wireless Future Technologies (SWiFT) lab at the American College of Greece.

- FIREMAN demo for IoT setup

It is a project funded by the EU for the development of IoT systems for manufacturing environments. The MAMP prototype is integrated with the system for the IoT network, which showed improved performance for the multiple sensor nodes in the lab. The MAMP is installed at the access point which connects to the network of sensor nodes. A narrow and pointed beam can connect to the transmitter node with an increased gain, which can reduce the battery life at the transmitter node. An access point is chosen with

2 RF ports so that the proposed MAMP can be integrated with the device, and it can measure RSSI at each user equipment. The RSSI at sensor nodes is shown using a GUI which is clearly reduced when MAMP is directed towards a certain transmitting node.

- SDR demonstration

The prototype is integrated with the existing 4G/5G setup in the lab. The setup consists of USRPs and server machine to configure the 4G over the air. Comparable performances are shown by integrating the MAMP with the USRPs to enable the 5G and 4G cellular services. The received powers are obtained and displayed for the proof of concept and to analyze the performance of the MAMP antenna array. A comparison between an Omni antenna and a MAMP is shown, where the MAMP array is clearly performing better than an Omni antenna. Data rates from 5Mbps to 25Mbps are achieved at 2.6GHz using the MAMP array with no packet loss or very low loss. The data rates for 5G setup using MIMO would be of great interest in the future.

Ideally, a MAMP would be considered in the future with a greater number of active elements, and it should perform at mmWave bands with considered scenarios for the self-backhaul and fixed wireless communications. The MAMP should be implemented with varactors to steer the beam in all the possible achievable angles while it maintains the radiation efficiency and the peak gain above the desired threshold



